

Towards Translation of Portable, Non-invasive, Near-infrared Imaging Systems

A Dissertation Presented
by

Morris D. Vanegas

to

The Department of Bioengineering

in partial fulfillment of the requirements
for the degree of

Doctor of Philosophy

in

Bioengineering

**Northeastern University
Boston, Massachusetts**

May 2023

NORTHEASTERN UNIVERSITY
Graduate School of Engineering

Dissertation Title: Towards Translation of Portable, Non-invasive, Near-infrared Imaging Systems.

Author: Morris D. Vanegas.

Department: Bioengineering.

Approved for Dissertation Requirements of the Doctor of Philosophy Degree

Dissertation Advisor: Dr. Qianqian Fang

Date

Dissertation Reader: Dr. Mark Niedre

Date

Dissertation Reader: Dr. Meryem Yücel

Date

Department Chair: Dr. Lee Makowski

Date

Director of the Graduate School:

Dean: Dr. Gregory D. Abowd

Date

ABSTRACT

Towards Translation of Portable, Non-invasive, Near-infrared Imaging Systems

by

Morris D. Vanegas

Doctor of Philosophy in Bioengineering

Northeastern University, May 2023

Dr. Qianqian Fang, Adviser

Medical imaging has become a fundamental research tool that continues to grow at a rapid pace. It has made enormous contributions to accelerating our ability to diagnose malignant breast lesions, measure brain functions, and capture oxygenation vital signs. Unfortunately, contemporary imaging modalities rely heavily on radiation- and nuclear-based methods, require coupling gels or contrast agents, or are simply too massive requiring patients to be immobile during use. These disadvantages not only limit our research to basic functions in highly-controlled environments, but their cost has become a barrier-to-entry for use by many populations that can benefit from their frequent use.

In order to translate our diagnostic capabilities from the laboratory to clinical and natural settings, we need a non-invasive, non-ionizing, gel-free, portable, and low-cost imaging approach. In this thesis, we focus on optical imaging in the visible and near-infrared (NIR) range. Optical imaging uses multiple wavelengths of light to probe the molecular function of tissues. Its varied implementation methods allow for singular measurements, 2-D functional images, and 3-D tomographic reconstructions.

Our overarching goal is to demonstrate how NIR imaging is a conduit for medical imaging innovations for the rest of the twenty-first century. We demonstrate this through the design and

development of three NIR systems with varying system lifecycle properties to address three national and global grand challenges. From fingertip-based imaging in rural areas, to breast imaging in low-light mammography environments, and even brain imaging in unconstrained locations, these challenges intentionally demonstrate the potential broad application of NIR imaging across populations and settings. Additionally, we facilitate the adoption of NIR imaging through the creation of a software platform for semi-automating the design of new systems based on a modular architecture as well as a systematic method for the creation of optical phantoms using off-the-shelf 3-D printing filaments.

Overall, this thesis leverages innovations in computational methods, advanced electronic sensors, and ubiquitous devices to elevate existing NIR-based methods into state-of-the-art imaging systems. This work positions NIR-based imaging as a functional medical imaging contender worthy of attention, exploration, and adoption due to its capability to image basic and complex dynamics in a range of environments.

To the...

ACKNOWLEDGEMENTS

Here I wish to thank those who have supported me during the process of the thesis work...

PREFACE

Here I'll write a dope section. More personal. Something that states why I started this research.

TABLE OF CONTENTS

LIST OF ACRONYMS	xvii
1 INTRODUCTION	1
2 BACKGROUND	5
2.1 Basics of Optical Imaging	5
2.1.1 Light-Tissue Interactions	5
2.1.2 Components of Optical Measurement Systems	7
2.1.3 Optical Phantom Fabrication	7
2.2 Imaging Techniques	8
2.2.1 Pulse Oximetry	8
2.2.2 Functional Near-Infrared Spectroscopy	9
2.2.3 Diffuse Optical Tomography	9
2.2.4 Structured-Light Imaging	10
2.3 “-ilities” of Near-infrared Imaging Systems	10
3 MOBILE-PHONE-BASED OXIMETER (MOXI)	12
3.1 Introduction	12
3.2 D1: Bluetooth Reflectance Pulse Oximeter	14
3.2.1 D1: Reflectance Board Hardware	14
3.2.2 D1: Reflectance Board Software	16
3.2.3 D1 Results	17
3.3 D2: Single Slit Oximeter	18
3.3.1 D2: Single Slit Hardware	18
3.3.2 D2: Single Slit Software	19
3.3.3 D2 Results	19

3.4	D3: Paper Filter Pulse Oximeter (MOXI)	22
3.4.1	Photon Propagation Simulations	22
3.4.2	Simulation Validation Results	25
3.4.3	Pilot clinical testing	26
4	MODULAR OPTODE CONFIGURATION ANALYZER (MOCA)	30
4.1	Introduction	30
4.2	Modular Probe Parameters and Performance Metrics	33
4.2.1	Essential module-level design parameters of fNIRS modular probes	33
4.2.2	Probe-level assembly process parameters	36
4.2.3	Performance metrics to characterize probes	38
4.3	Additional Functionalities	41
4.3.1	Parameter sweeping	41
4.3.2	Exporting probe for use in AtlasViewer	42
4.4	Results and Practical Examples	43
4.4.1	Slab-based brain sensitivity corresponds with atlas-based sensitivity	43
4.4.2	Comparison between sample modules of various shapes.	43
4.4.3	Improving existing probes through probe-level parameter alterations	50
4.5	Discussion	56
5	MODULAR OPTICAL BRAIN IMAGER (MOBI)	61
5.1	Introduction	61
5.2	Methods	63
5.2.1	Module design	63
5.2.2	System architecture	66
5.2.3	Automatic features	68
5.2.4	In-vivo protocols	69
5.3	Results	69
5.3.1	System characterization	69
5.3.2	Spatial multiplexing improvement	70
5.3.3	Optode-scalp coupling	71
5.3.4	Automatic optode positioning	73
5.3.5	Cuff occlusion results	74

5.3.6	Finger-tapping results	74
5.4	Discussion	76
6	OPTICAL MAMMOGRAPHY CO-IMAGER (OMCI)	79
6.1	Introduction	79
6.2	Methods	82
6.2.1	OMCI Instrument	82
6.2.2	Dual-camera SLI breast surface scanning system	84
6.2.3	Alternative breast surface reconstruction methods for assessing SLI surface accuracy	87
6.2.4	Evaluation of the impact of surface errors on DOT image reconstructions .	92
6.3	Results	93
6.3.1	Camera-projector calibration and surface acquisition	93
6.3.2	Surface estimation errors	94
6.3.3	Mean square error of optical property reconstruction	94
6.3.4	Full system <i>in-vivo</i> patient results	96
6.4	Discussion	96
7	3-D PRINTED PHANTOMS	99
7.1	Introduction	99
7.2	3-D Printing Hardware	100
7.3	New Filament Characterization	101
7.4	Multi-filament slicing	103
7.4.1	Artifacts for purging during transition	103
7.4.2	MOXI, MOBI, and OMCI system slicing	104
7.5	Lessons learned for use of PETG in filament mixing	104
8	CONCLUSION	106
8.1	Summary	106
8.2	Comparing system lifecycle properties	108
8.3	Future Outlook	111
REFERENCES		112

LIST OF FIGURES

2.1	Possible interactions when light interfaces with tissue. The pink rectangle represents tissue. White circles are scatterers. Black dots are absorbers. (1) Light reflects without entering the tissue. (2) Light immediately gets absorbed. (3) Light scatters multiple times before being absorbed. (4) Light scatters multiple times before exiting the tissue on the opposite side it entered. (5) Light scatters multiple times but exits on the side it entered.	6
3.1	(a) Screenshot of Moximeter mobile application simultaneously capturing D1 and D3 data. (b) D1 (green, dashed) and D3 (yellow, solid) mounted on a smartphone phone. (c) D2 board with cover.	14
3.2	(a) D1 phone mount. (b) Simultaneous capture of D1 and D3.	15
3.3	(a) Photoplethysmogram signals from evaluation module board and D1 design. (b) Ratio-of-ratios in blue (evaluation module) and green (D1 Device).	17
3.4	(a) Top side of D2 circuit showing USB connector and microcontroller. (B) Bottom side of the D2 circuit showing deep red (top) and red (bottom LEDs). (C) D2 board powered by a smartphone and an on-the-go USB cable.	18
3.5	(a) Nexus and Andor camera experimental setup. (b) Example cropped slit image for analysis.	20
3.6	Intensity attenuation slopes for the Andor (a) and Nexus (b) camera data. Top (640 nm) and bottom (730 nm) rows show the averaged attenuation slope of the log-scaled light intensity over time within a selected window. The vertical green lines mark the point at which pressure from the cuff was released.	21
3.7	(a) D3 design in use with a finger placed over the camera after a paper filter is taped over the bottom half of the mobile phone camera. (b) Broadband spectra (black) and resulting spectra after manipulation using colored paper filters. The color line refers to the color of the paper filter. (c) Simulation setup showing finger model with six tissue types.	23
3.8	Process of creating the ratio-of-ratio to arterial blood oxygen saturation mapping in simulation. Monte Carlo simulations result in fluence measurements at various arterial blood oxygen saturation values for both wavelengths at 0 and 20% artery volume increase. An example 1 second photoplethysmogram pulse is scaled by the fluence measurements and repeated to create a time trace. Each repetition is low-pass filtered with a randomized cutoff frequency between 60 and 100 hz. The ratio-of-ratio value is then calculated from the simulated photoplethysmogram signals.	25

3.9	Results of ratio-of-ratio mapping to arterial blood oxygen saturation based on Monte Carlo simulations. The curves are shown for two-wavelength simulations in transmission, two-wavelength simulations in reflection, and broadband simulations in reflection.	26
3.10	Results from comparison of our broadband reflectance-based oximeter with a clinical grade pulse oximeter. Green lines indicate clinical pulse oximeter readings sampled at 1 Hz. Red lines indicate calculated arterial blood oxygen saturation measurements using our broadband oximeter.	28
4.1	Workflow of module-level design parameters (left column; blue) used in probe-level processes (center column; red) to produce performance metrics to characterize a probe (right column; green). Performance metrics are organized top to bottom from least complex (two parameters needed) to most complex (four parameters needed). Arrows trace how parameters are used to derive specific performance metrics.	34
4.2	Example probe exported for use in AtlasViewer [1]. (a) A four-module probe with three sources (red circles) and two detectors (blue crosses) plotted using MOCA. Intra- (blue) and inter-module (orange) channels are shown in solid lines. (b) Imported probe in SDgui. Solid lines represent fixed springs. Dashed green lines represent flexible springs between sources and detectors. Three dummy optodes (numbered 21, 22, and 23) are shown in black. (c) The resulting probe in AtlasViewer registered to an atlas using the dummy optodes as anchors.	44
4.3	Results comparing brain sensitivity derived from finite slab models used by MOCA and atlas-based models. The blue line shows calculated brain sensitivity based on a five-layer slab model for SD separations from 0 to 60 mm in 1 mm increments. Overlaid in black are the brain sensitivity results calculated from an atlas by averaging brain sensitivity for fixed source-detector separations across nineteen locations in the international 10-20 system [2].	45
4.4	Elementary module designs used in a full-head comparison. (a), (b), and (c) show the perimeter of the square, hexagon, and triangle-based module designs, respectively. The optode layout of all three shapes is identical. Red circles represent sources while blue crosses represent detectors. (d) Tessellation of the hexagon module over an ROI. The dashed green line outlines the 200×200 mm ROI.	47
4.5	Channel distributions and total channel counts resulting from the tessellation of the three elementary module shapes over a 200×200 mm region of interest. (a-c) Resulting intra- and inter-module channel distributions for square, hexagon, and triangle module-based probes. (d) The total channel count of each probe grouped by intra- and inter-module channels.	48
4.6	Resulting average brain sensitivity organized by intra- and inter-module channels for square-, hexagon-, and triangle-based probes tessellated over a 200×200 mm region. Short-separation channels are excluded from all calculations.	49

4.7	Spatial multiplexing group results from the tessellation of the square-, hexagon-, and triangle-based probes. (a) Comparison of the total number of sources (orange) and the total number of spatial multiplexing groups (green). (b) The triangle-based module tessellation with sources (red circles) and detectors (blue crosses). The dashed red circles indicate the “effective” region (30 mm radius) of each of the nine sources in the first spatial multiplexing group. The nine sources turned on simultaneously in this group are indicated by filled-in red circles.	50
4.8	A 4-module probe simulated using MOCA. (a) All modules are oriented in the same direction. Red circles represent sources and blue crosses represent detectors. An exhaustive search of all combinations of orientations for each of the four modules results in 256 possible layouts. The average brain sensitivity and number of spatial multiplexing groups for the first 128 layouts are shown in (b). The original layout (layout number 1) is highlighted in the red square. An example layout with the maximum possible brain sensitivity (layout number 66) is highlighted in the green square. (c) A visual representation of layout 66 with the bottom-left and top-right modules rotated 90 degrees clockwise with respect to orientation in (a). Intra- and inter-module channel distribution resulting from the original layout is shown in (d). Channel counts resulting from the probe configuration in (c) are shown in (e). In both channel distribution histograms (d, e), intra- and inter-module channels are shown in blue and orange, respectively. Dark orange indicates overlapping histogram counts.	52
4.9	An analysis of hexagonal modules in a twelve-module probe. (a) Green arrows indicate the distances between modules as probe spacing varies. (b) The total channel count, average brain sensitivity, and the spatial multiplexing ratio at probe spacing values between 1 and 30 mm. Module orientations are held constant.	54
4.10	An analysis of square modules in a three-module probe. (a) A traditional three-module tessellation. Red circles represent sources and blue crosses represent detectors. (b) The resulting intra- and inter-module channel distribution from the probe layout in (a). (c) The average brain sensitivity for each layout resulting from module staggering separated by intra- and inter-module channel contributions. (d) The center module staggered by 26 mm, resulting in increased channel separation for inter-module channels, as shown in (e). (f) The total channel count and the number of spatial multiplexing groups of the probe layout as the center module is staggered between 0 and 42 mm.	55
5.1	(a) Top side of a Modular Optical Brain Imager (MOBI) module without a silicone cover showing the four flexible printed circuit connectors and 5 hair removal holes. (b) Bottom side of a MOBI module with light guides on optodes and black silicone cover of board. (c) Unpopulated flexible-circuit-board for a MOBI module.	64
5.2	Schematic diagram of a single Modular Optical Brain Imager module. The microcontroller uses an internal Inter-Integrated Circuit protocol to communicate with components on a single board. A peer-to-peer network allows communication between neighboring modules.	65
5.3	(a) Schematic diagram of a Modular Optical Brain Imager system. An external power source and trigger board are optional. (b) The master module without its cover.	66

5.4	(a) Five modules in a single chain configuration connected to a master module. (b) Modular Optical Brain Imager (MOBI) Graphical User Interface (GUI) displays 5 modules connected. (c) MOBI GUI displays the relative position of each module based on differences in neighboring orientation measurements.	67
5.5	Signal-to-noise (SNR) of Modular Optical Brain Imager modules as source-detector separation increases. Red asterisks indicate SNR for the 735 nm while black diamonds are for the 850 nm wavelength. Orange numbers signify the channel number. Channels 1, 2, and 3 are from the same module. Channels 4, 5, and 6 are from sources and detectors on different modules.	70
5.6	Three example probe layouts all composed from five identical Modular Optical Brain Imager modules. Optodes are represented by small red circles (sources) and blue crosses (detectors). Each layout has multiple spatial multiplexing groups determined based on the global proximity of sources to each other. Red dashed circles show which sources are simultaneously on for the first spatial multiplexing group of each layout.	71
5.7	(a) A rigid-based board showing three sources and two detectors. (b) Boxplot showing the distance from optode locations to the center of the sphere using rigid modules. The red line denotes the average distance of all 25 optodes. The dashed green line represents the expected distance to the center given the 5 mm thickness of the modules. (c) A histogram of the distances reveals that the rigid-based probe does not conform to the sphere, leading to optodes being farther away from the surface, especially those optodes closer to the edge of the module. (d) A flexible-circuit-based board showing three sources and two detectors with light guides. (e) Boxplot showing the distance from the optodes to the center of the sphere of the flexible-circuit-based probe. (f) The histogram of the flexible-circuit-based probe optode distances.	72
5.8	(a) Flexible-circuit-based Modular Optical Brain Imager (MOBI) modules arranged in probe layout 2 (from Figure 5.6) on top of a 100 mm radius sphere. (b) Spline model between 5 MOBI modules (green line) from which source (red crosses) and detector (blue crosses) positions are derived. Automatic optode digitization overlaid on manual digitization results (cyan circles). (c) Digitization error distribution averaged over all five modules in the probe. A green asterisk indicates the average digitization error. (d) Digitization errors are grouped by module.	73
5.9	Results from a dual-pressure blood occlusion experiment using (a) a single Modular Optical Brain Imager module and (b) a single Artinis channel placed on the forearm. Venous (100 mmHg) and arterial (220 mmHg) occlusions lasted 75 seconds each prior to release. Oxygenated, deoxygenated, and total hemoglobin concentrations are shows in red, blue, and green lines, respectively.	74
5.10	Block average results from a finger-tapping experiment with a Modular Optical Brain Imager module placed over the left motor cortex centered on C3 in the standard 10-20 system. Solid lines are oxygenated and dashed lines are deoxygenated hemoglobin. Magenta, cyan, and orange lines represent different channels within the probe.	75
6.1	The patient side of our OMCI system in its fully compressed state.	83

6.2	(a) Top-view of the breast compression compartment – upper: structured-light imaging system; bottom: horizontal cross-section (orange line) of the compressed breast with blue circles indicating the placement of the checkerboard used for system calibration. Numbers 1-5 indicate the 5 board orientations repeated at each location for calibration. (b) Side-view of the breast compression plates, showing the linear translation stage (blue bar on the right) and a linear encoder (in yellow), and (c) 3-D rendering of the structured-light imaging system, an acrylic bottom plate, and an acrylic compression plate (top).	85
6.3	(a) Front-view photo of the structured-light imaging system. Cameras and projectors are embedded in an acrylic mount to prevent the need for re-calibration. (b) Horizontal bar patterns reflecting off the top compression plate and onto the breast show curved illumination bar artifacts when the scaling factor α is set to 1. In (c), we show the same illumination pattern with thickness-informed masking eliminating the curved bar artifacts by cropping the patterns exceeding the breast surface before projection. Additionally, the scaling factor is automatically calculated to prevent camera saturation.	86
6.4	Flow chart of image acquisition for both subject measurements and system calibration. Subject measurements calculate a saturation scaling factor and mask the illumination patterns prior to projecting patterns. System calibration measurements do not mask the illumination patterns and project at full intensity. The calibration loop (dashed lines) is repeated for each location and orientation of the calibration checkerboard.	88
6.5	Generation of breast surface meshes using multiple acquisition methods. The digital breast tomosynthesis (DBT) volumetric mesh is created from segmented scans. The extrusion surface mesh is created by extruding the top contour to the breast thickness. The top and side contours of the DBT mesh are swept to create top and side surface meshes. The structured-light imaging mesh is created by scanning a 3-D printed breast phantom and trimming the resulting point-cloud using the linear encoder measurements. The surface estimation error is calculated for each of the surface meshes by comparing the surface estimations to the DBT mesh. All surface meshes are converted to volumetric meshes for validating the effect of surface estimation methods on inclusion reconstruction.	89
6.6	(a) Surface mesh of a digital breast tomosynthesis (DBT) model obtained from The Cancer Imaging Archive [3]. Blue cyan lines show the x/y and y/z breast contours from the top and side views. (b) Estimate of the DBT surface using the extrusion method in which the contour (cyan) is extruded to the thickness of the breast along the z axis. (c) The top-sweep method uses the x/y contour as the profile (cyan) and the y/z contour as the path to sweep (red). (d) The side-sweep method uses the y/z contour as the profile (cyan) and the x/y contour as the path to sweep (red). (e) point-clouds from both camera-projector pairs were generated by scanning a 3-D printed model of the DBT breast using the structured-light imaging system. The green (Camera 1) and magenta (Camera 2) point-clouds are in the respective camera coordinates. (f) Merged and denoised point-cloud in the projector's coordinates. . .	91

6.7	A comparison between the mean squared error (MSE) of the reconstructed absorption map using 4 estimated surfaces (EXT - z -axis extrusion, TOP - sweeping x/y contour along y/z contour, SIDE – sweeping y/z contour along x/y contour, and SLI – surface acquired from our structured-light imaging system) as well as the ground truth digital breast tomosynthesis surface. A 1 cm diameter spherical inclusion is moved away from the breast surface at various depths between 5 and 45 mm in 1 mm increments. Image slices (in x/y plane) of the reconstructed absorption coefficient (μ_a in mm^{-1}) (top-row) and the ground truth μ_a (bottom-right) are shown as insets.	95
6.8	These images will be replaced with patient data showing structured-light imaging (SLI) in a healthy volunteer. I will also show reconstructed results and will cite Edward + Miguel. Edward to provide me with patient IDs that have good SLI acquisitions. (b) The generated 3D breast-shaped mesh from a SLI measurement on a healthy patient.	97
7.1	(a) Flowchart showing how to use measured path widths to adjust extrusion multiplier values when characterizing filaments. (b) Printed square wall using clear filament. (c) Caliper measurements show over-extrusion.	102
7.2	The “caging” purge method (a) An example penguin composed of three different tissue types. (b) The same penguin model with the cage shown. The colors of the cage indicate the colors on that segment of the print. (c) Resulting 3-D printed penguin.	103

LIST OF TABLES

2.1	Definition of ilities. Asterisks indicate the definition was replicated from de Weck et al., 2012 [4]	11
3.1	Barriers to adoption of new medical devices in low- and middle-income countries (LMIC)s	13
4.1	Optical properties used in the slab model for calculating brain sensitivity based on Fang <i>et al.</i> [5]. The thickness of each layer is derived by dividing the total tissue volume by the tissue's surface area from a tetrahedral five-tissue brain model [6]. The absorption coefficient, μ_a , is the average path a photon will travel in the medium before being absorbed. Similarly, the scattering coefficient, μ_s , defines the average path length of photons before a scattering event. Anisotropy, g, is a unit less measure of the amount of forward direction retained after a single scattering event.	40
4.2	Summary of quantitative performance metrics derived by MOCA when tessellating the three elementary module shapes over a 200×200 mm region of interest.	46
5.1	The full frame rate of a probe depends on the layout of the modules within a probe. The three layouts in Figure 5.6 result in the channels, groupings, and full frame rates below.	70
6.1	Mean and standard deviation of the residuals of each point in a surface estimation mesh compared to the original digital breast tomosynthesis breast mesh.	94
8.1	Pugh Chart ranking of NIR systems	108

LIST OF ACRONYMS

- AC** alternating current.
- ADC** analog-to-digital converter.
- AFE4490** analog front-end.
- BRAIN** Brain Research Through Advancing Innovative Neurotechnologies.
- CCD** charge-coupled device.
- CMOS** complementary metal-oxide semiconductor.
- CSF** cerebral spinal fluid.
- CW** continuous-wave.
- DAC** digital-to-analog converter.
- DBT** digital breast tomosynthesis.
- DC** direct current.
- DICOM** Digital Imaging and Communications in Medicine.
- DOT** diffuse optical tomography.
- EEG** electroencephalogram.
- EM** extrusion multiplier.
- EMCCD** electron-multiplying charge-coupled device.
- EVM** evaluation module.
- FD** frequency-domain.
- FDM** fused-deposition modeling.
- fMRI** functional magnetic resonance imaging.
- fnIRS** functional near-infrared spectroscopy.

- FPC** flexible printed circuit.
- GM** gray matter.
- GUI** graphical user interface.
- HbO** oxygenated hemoglobin.
- HbR** de-oxygenated hemoglobin.
- HbT** total hemoglobin.
- HR** heart rate.
- HRF** hemodynamic response function.
- IMU** inertial measurement unit.
- IR** infrared.
- ISP** in-service programmer.
- JST** Japan Solderless Terminal.
- LASER** Light Amplification by Stimulated Emission of Radiation.
- LED** light emitting diodes.
- LMIC** low- and middle-income countries.
- MCX** Monte Carlo eXtreme.
- MEG** magnetoencephalography.
- MOBI** Modular Optical Brain Imager.
- MOCA** Modular Optode Configuration Analyzer.
- MOXI** Mobile-phone-based Oximeter.
- MRI** magnetic resonance imaging.
- MSE** mean squared error.
- NCI** National Cancer Institute.
- NIBIB** National Institute of Biomedical Imaging and Bioengineering.
- NIH** National Institutes of Health.
- NIR** near-infrared.
- NIRS** near-infrared spectroscopy.

OMCI Optical Mammography Co-Imager.

P2P peer-to-peer.

PCB printed circuit board.

PET positron emission tomography.

PETG polyethylene terephthalate glycol.

PLA polylactic acid.

POC point-of-care.

PPG photoplethysmogram.

PTFE polytetrafluoroethylene.

PW path width.

PWM pulse-width modulation.

RF radio frequency.

ROI region-of-interest.

RR ratio-of-ratio.

SD source-detector.

SDS source-to-detector separations.

SLI structured-light illumination.

SMG spatial multiplexing group.

SMIR spatial multiplexing improvement ratio.

SMR spatial multiplexing ratio.

SNIRF Shared Near Infrared Spectroscopy Format.

SNR signal-to-noise ratio.

SPECT single-photon emission computerized tomography.

SPI serial-peripheral interface.

SpO₂ arterial blood oxygen saturation.

SS short-separation.

StO₂ tissue oxygen saturation.

TCGA The Cancer Genome Atlas.

TTL transistor-transistor logic.

USAID US Agency for International Development.

WF wide-field.

WM white matter.

CHAPTER 1

INTRODUCTION

Modern civilization has leveraged medical imaging as a fundamental clinical and research tool for years. Although x-rays dominated the field for 80 years after its invention [7], the field is growing at a rapid pace due in part to the increasing availability of relatively inexpensive computational resources [8]. In recent decades, we have seen an emergence of new imaging technologies that improve on traditional methods being developed and commercialized, including magnetic resonance imaging (**MRI**), nuclear imaging [such as positron emission tomography (**PET**) and single-photon emission computerized tomography (**SPECT**)], and ultrasound imaging [9]. These contemporary imaging modalities have improved on the ionizing approach of x-ray, and thus, more and more frequently have taken the center stage of routine clinical use.

Unfortunately, many of our modern-day diagnostic approaches rely heavily on radiation- and nuclear-based imaging tools—so much so that the largest man-made source of radiation exposure comes from radiation due to medical examinations [10]. Nuclear imaging relies on the detection of injected radioactive isotopes that attach to biochemically active substances in the body [11]. Improving on these methods, ultrasound imaging uses high-frequency sound waves that are reflected back due to different acoustic impedances of tissues and collected to form an image [12]. Although particularly useful for imaging structures in motion, ultrasound is not used for brain imaging because of the high attenuation of the sound waves by the skull. **MRI** is also non-ionizing, using high-energy magnets to obtain structural information from changing spin properties of subatomic particles[13]. It is one of the most exciting modalities since it can achieve high-resolution scans of the entire body. The drawback is that these **MRI** machines are immense, extremely expensive, and require the user to be immobile during use, which limits its impact to investigations of immobile functions and to populations with the economic resources to access them. We are in need of an

imaging technique that is non-invasive, non-ionizing, can be used to diagnose various areas of the body, and is portable and low-cost enough for use by the masses.

Optical imaging is a non-invasive and non-ionizing method that uses visible and near-infrared light to probe the molecular function of tissues [14]. Although some optical imaging methods use agents (such as fluorescence and phosphorescence imaging), in this dissertation we focus on non-invasive (no agent) methods of optical imaging. The near-infrared part of the electromagnetic spectrum is typically used because soft tissues show less scattering and absorption to these bands. The composition of the imaged tissue determines how the light is absorbed, reflected, or scattered. The complexity of the interaction between light and tissue was once incredibly difficult to model, but technological advances in computational methods and devices has positioned near-infrared (**NIR**) imaging as a contender for functional medical imaging.

Our overarching goal is to demonstrate how **NIR** imaging is a conduit for medical imaging innovations for the rest of the twenty-first century. To do that, we must be bold—we will address modern national and global grand challenges to show the potential breadth of application of **NIR** imaging. The first challenge is posed by the US Agency for International Development (**USAID**) through their Saving Lives at Birth Initiative. The goal is to address the heightened high-risk period for babies from the onset of labor through 48 hours after birth in **LMIC**. This period accounts for 48 percent of maternal deaths and 54 percent of neonatal deaths annually [15]. For the second challenge, we turn toward the brain. The Brain Research Through Advancing Innovative Neurotechnologies (**BRAIN**) Initiative is focused on the development and application of new technologies to image the brain for the treatment, cure, and prevention of brain disorders. Through funding from the National Institutes of Health (**NIH**) National Institute of Biomedical Imaging and Bioengineering (**NIBIB**), we will develop a portable neuroimaging system with features tailored towards use in natural environments. And finally, we will address the challenge of improving breast cancer diagnosis and prevention of unnecessary biopsies through a grant from the **NIH** National Cancer Institute (**NCI**) for the development of an optical mammography system that augments existing x-ray mammography systems and scans. Although the field of medical imaging is continually advancing, at the time of writing, no contemporary imaging technique is suited to address all three aforementioned challenges.

This dissertation will show the potential of **NIR** imaging to address a variety of current application-, user-, and setting-specific needs through the development of multiple **NIR** systems. Although each of the imaging systems described in this thesis will vary in attributes (such as complexity, cost, and scalability), as the title of this thesis suggests, we will focus on the following

requirements:

1. Each **NIR** system must address portability, either through a stand-alone system or through simple integration into an existing imaging modality system.
2. Each **NIR** system must be non-invasive (use no reactive agents) and non-ionizing.
3. Each **NIR** system must utilize the visible and/or near-infrared spectral window.

To address these grand challenges while meeting the requirements above, some system will leverage computational improvements of light propagation models while other systems will integrate technological advancements in sensors to improve existing techniques. In all we will take a product-focused lens to ensure what we are building is addressing the needs of users (and prevent us from falling into the academic pitfall of building for the sake of building). By demonstrating use cases and designs across a variety of medical imaging attributes, we hope to show the medical community at large the benefits of non-invasive **NIR** methodologies and ways to translate these technologies outside of the research setting.

This thesis is separated into five high-level aims. The first three aims refer to the development of three individual portable and/or wearable near-infrared imaging systems. We will present the design, fabrication, and characterization of these systems as well as measurements on human test subjects. The fourth aim refers to the progress made towards a phantom fabrication workflow to manufacture optical phantoms of known optical properties for the validation of new **NIR** systems. Finally, the fifth aim condenses the work into a Pugh chart [16] by comparing all three developed **NIR** systems to an elementary **NIR** imaging system, a finger-clip-based pulse oximeter.

While this introductory chapter sets the challenge and scope of the research for this dissertation, Chapter 2 gives necessary background into the basics of optical imaging, details the **NIR** imaging techniques used in this work, and defines the “ilities” [4] that will be compared between all three systems. Chapter 3 shows how we address the first challenge through the development of a mobile-phone-based pulse oximeter that leverages the sensors inside already ubiquitous mobile phones in **LMIC**. The second challenge of advancing neuroimaging is broken down into two chapters detailing software and hardware solutions. We first describe a software workflow that helps design new modular-architecture-based functional near-infrared spectroscopy (**fNIRS**) systems (Chapter 4) before describing the hardware development of a wearable functional brain imaging system with features tailored towards its use in natural, unrestricted environments (Chapter 5). The third challenge is addressed in Chapter 6. By combining the physiological measurements from optical

imaging with the structural imaging from x-ray, we not only improve stand-alone optical imaging reconstructions but also improve existing x-ray mammography, all without exposing a patient to more ionizing radiation. Chapter 7 discusses the use of additive manufacturing in the development of optical phantoms utilized by all three systems in the first three aims. Finally, in Chapter 8, we compare the three systems across their abilities and conclude the significance and impact of this work.

CHAPTER 2

BACKGROUND

2.1 Basics of Optical Imaging

2.1.1 Light-Tissue Interactions

Biological optical imaging has the capability to detect biological structure, function, and molecular characteristics based on photon interactions with tissue [17]. The interaction of light with tissue is governed primarily by three processes: reflection, scattering, and absorption [18].

The index of refraction, n , is a unitless number that describes how fast light travels through material [17]. It is used to determine how much the path of light is bent upon transitioning from one material to the next. This is governed by Snell's Law of Refraction [17], $n_1 \times \sin\theta_1 = n_2 \times \sin\theta_2$, which define the angle of incidence, θ_1 , and angle of refraction, θ_2 , based on two media with indices of refraction n_1 and n_2 . Thus, from Snell's Law, we can also determine the amount of light that is reflected when reaching an interface (Figure 2.1).

Once photons enter a turbid media, they move in all directions and may be scattered or absorbed (Figure 2.1). Absorption depends on the component concentrations of tissue [14]. In the visible to near-infrared wavelength range, the primary absorption components include water, hemoglobin, pigment, and lipid [19, 20]. The absorption coefficient, μ_a [cm^{-1}], is defined such that, when a photon propagates over an infinitesimal distance ds , the probability of absorption is $\mu_a \times ds$ [18]. The absorption coefficient depends on the molar extinction coefficient of a given chromophore ϵ [$cm^{-1} \times M^{-1}$], and its Molar concentration, c . Thus, the absorption coefficient per wavelength is

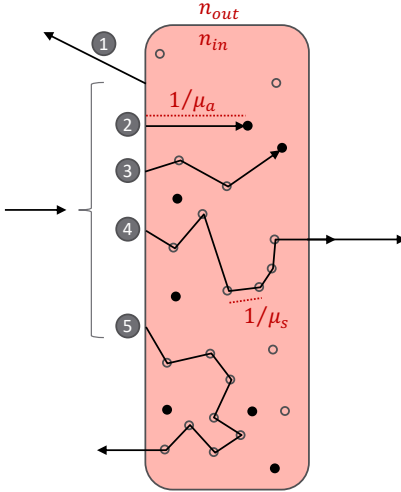


Figure 2.1: Possible interactions when light interfaces with tissue. The pink rectangle represents tissue. White circles are scatterers. Black dots are absorbers. (1) Light reflects without entering the tissue. (2) Light immediately gets absorbed. (3) Light scatters multiple times before being absorbed. (4) Light scatters multiple times before exiting the tissue on the opposite side it entered. (5) Light scatters multiple times but exits on the side it entered.

$$\mu_a(\lambda) = \log(10) \sum_{i=1}^t \epsilon_i(\lambda) \times c_i \quad [14]. \quad (2.1)$$

where t is the total number of absorbing components in the tissue. From this, we deduce that $1/\mu_a$ is the average path length traveled by a photon before being absorbed.

Light entering a tissue can also undergo scattering events, events during which directionality changes occur due to biological structures within the media (Figure 2.1). In the visible to infrared wavelength range, the primary scattering components in biological tissue are protein, fat, and mitochondria [19, 20]. Analogously, the scattering coefficient, μ_s , is defined such that, when a photon propagates over an infinitesimal distance ds , the probability of scattering is $\mu_s \times ds$ [18]. Additionally, we model the probability distribution of scattered photons by an angular function known as the anisotropy factor, g [17]. Since g is based on the scattering angle, the closer to 1.0 g is, the more likely the photon is to be scattered in the forward direction. To account for this anisotropy factor, we define the reduced scattering coefficient, μ'_s , as $\mu'_s = \mu_s(1 - g)$ [17]. The average distance traveled by a photon between scattering events is $1/\mu_s$.

2.1.2 Components of Optical Measurement Systems

Optical systems are composed of three elementary blocks: a source that radiates light, a sample through which light propagates, and a detector that measures the light intensity after photons have traveled through the sample [21]. Although there are numerous types of sources and detectors, here, we highlight only the types used in the optical systems developed for this thesis.

light emitting diodes (**LED**) are devices that radiate light when a current passes through them [21]. They are ubiquitous in modern electronics due to being inexpensive and requiring minimal power to operate. In our Mobile-phone-based Oximeter (**MOXI**) system, we leverage the white LEDs used for flash photography common in most smartphones. Our Modular Optical Brain Imager (**MOBI**) system uses dual-wavelength **LEDs** chosen to optimize propagation within the brain layers. Arrays of **LEDs** are used in conjunction with digital micromirrors to project color images from projectors. Our Optical Mammography Co-Imager (**OMCI**) system uses an **LED** projector to shine patterns to scan the surface of the breast. For certain applications, it is better to have a light source that does not spread out much, such as Light Amplification by Stimulated Emission of Radiation (**LASER**). Laser light sources produce very narrow beams of light. In **OMCI**, we use a laser to input light into a projector to project patterns onto the breast.

Detectors are devices used to measure light. Photodiodes are the reverse of **LEDs**—they convert light into electrical current [21]. Their cost tends to be relative to their sensitivity. **MOXI** and **MOBI** use inexpensive photodiodes chosen to be sensitive to the wavelengths of their associated **LEDs**. **OMCI** uses cameras to detect the reflection and transmission of projected patterns. These cameras capture light through a small lens using a tiny array of microscopic detectors.

The measured light, in combination with the known type of source, allows for the determination of biological structure, function, and molecular characteristics of the tissue through which the light propagated. For example, the detection of photons from particular wavelengths allows us to compute concentrations of oxygenated (HbO_2) and de-oxygenated (HbR) hemoglobin in tissue. From this, we can infer parameters such as total hemoglobin concentration and tissue oxygen saturation [14].

2.1.3 Optical Phantom Fabrication

Phantoms are objects with optical properties that mimic human tissues [20]. They are common for evaluating the performance of **NIR** imaging systems [20]. To mimic **NIR** light propagation due to components within biological tissue, phantoms typically attempt to mimic the reduced

scattering coefficient (μ'_s) and the wavelength-dependent absorption coefficient (μ_a) in biological tissue [22]. Traditionally, these phantoms are created using recipes that involve a mix of scattering agents and absorbing pigments with a base [23, 24]. The geometry of the phantom is typically created using either mold casting [25, 26] or spin coating [27]. While useful for simple phantoms, these methods fall short in supporting complex geometries needed for phantoms requiring structural and physiological properties, such as when diffuse optical tomography (DOT) is used to image the brain [28, 29]. Thus, a new method to manufacture phantoms with spatially varying optical properties and anatomically accurate geometries is needed to support the system development, calibration, and testing of new imaging protocols [30, 31].

2.2 Imaging Techniques

2.2.1 Pulse Oximetry

Pulse oximetry is used to measure oxygen saturation of hemoglobin in arterial blood and is so widely prevalent it is regarded as the fifth vital sign in medical care [32]. It is based on two principles. The first is that HbO_2 and HbR absorb red and infrared (IR) light differently [33]. Because of this, pulse oximeters tend to emit two wavelengths of light. Traditional (finger-clip) pulse oximeters place light sources and detectors on opposite sides of the finger. The second principle is that arterial blood volume fluctuates with the cardiac cycle while blood volume in veins, capillaries, skin, fat, and bone remains relatively constant [34]. Thus, light that propagates through the finger and is detected by the detector has two components during temporal measurements of the cardiac cycle—a relatively stable and non-pulsatile direct current (DC) component from the constant volume in veins and capillaries, and a pulsatile alternating current (AC) component from the volume fluctuation of the arteries [35]. This detected time trace is called a photoplethysmogram (PPG) [34].

Pulse oximeters use the amplitudes of PPG signals from red and IR light to calculate oxygen saturation (SpO_2) at the finger. SpO_2 is calculated from the ratio of the AC to DC components of the red and IR light. The ratio-of-ratio (RR) is defined as

$$RR = \frac{A_{red,AC}/A_{red,DC}}{A_{IR,AC}/A_{IR,DC}} \quad (2.2)$$

where A is absorbance. At low oxygen saturation, the increased HbR presence leads to a larger relative change in amplitude of red light due to the pulse compared to IR absorbance ($A_{red,AC} > A_{IR,AC}$), resulting in a higher RR value. SpO_2 is calculated from a calibration curve mapping

RR to SpO_2 generated from empirical measurements of RR in healthy volunteers with altered saturations [36].

2.2.2 Functional Near-Infrared Spectroscopy

fNIRS is an emerging neuroimaging technique that uses low-power near-infrared light to measure hemodynamic changes due to brain activities [37]. It is based on three fundamental principles. The first is that human tissue is relatively transparent to light in the near-infrared range allowing photons to propagate [38]. Secondly, hemoglobin has unique absorbing characteristics that allow for oxygenation-dependent quantification of **NIR** light absorption [38]. The third is the theory of neurovascular coupling, which states that the brain's demand for oxygen is altered by neuronal activation. fNIRS assumes that changes in hemoglobin concentrations are indicators of brain activity [37].

In **fNIRS**, multiple sources and detectors are placed on the scalp over a region-of-interest (**ROI**) [39]. The photons travel through the head being scattered and absorbed by the different tissue types [40] (scalp, skull, cerebrospinal fluid, and neuronal tissue) until the non-absorbed components of the scattered light are detected by a detector [41, 42]. The activity-dependent local increase of HbO and decrease of HbR change the absorption rate of neuronal tissue and affect the intensity of light detected [42, 43]. This change in intensity, along with the absorption spectra of chromophores, allows for the calculation of HbO and HbR concentrations via the modified Beer-Lambert law [39].

2.2.3 Diffuse Optical Tomography

DOT is a non-invasive imaging technique for 3-D functional tissue characterization [44]. This is done through the illumination of tissue with an array of light sources and the measurement of the exiting light with an array of detectors [45]. Typically, a source in the array is turned on and the light is measured by all detectors for that source. This is repeated sequentially for each source. A model of light propagation from the source to detector locations is parameterized using unknown scattering and absorption coefficients of the illuminated tissue [46]. The propagation model is then “inverted” to determine the scattering and absorption parameters of the tissue [46]. The inversion of the model is the solution to the question “given my array of sources, what optical parameters must my tissue possess in order to produce the results I measured with my array of detectors?”

Although conceptually simple, in practice, **DOT** is plagued with difficulties. The use of diffusive light along with the inherent ill-posedness of the inverse reconstruction leads to low spatial

resolution results [47, 48]. Additionally, the sensitivity to tissue-optode coupling coefficients of the coarse spatial sampling leads to an inaccurate representation of tissue properties [49]. To address low spatial resolution, the use of tissue structural priors (structural data obtained from MRI [50], ultrasounds [51], or x-ray [52, 53]) have been recently used to better constrain the inverse problem and produced higher resolution images [50]. Wide-field illumination (the projection of a pattern image rather than a few spare source points) and camera-based detection (where a pixel in a camera acts as a detector in an array) has allowed for high-density sampling and acceleration of data acquisition [54].

2.2.4 Structured-Light Imaging

One method of improving DOT reconstructions is to further constrain the inverse problem through highly accurate breast surface estimations. However, the two most prominent techniques for 3-D breast surface imaging (stereophotogrammetry and laser scanning [55]), require a large number of cameras and precise installation, making them infeasible in the confined, low-light mammography setting. An emerging, non-invasive 3-D surface imaging technique is structured-light illumination (SLI). SLI works by illuminating an object with 2-D spatially varying patterns and using an imaging sensor (e.g. a camera) to capture the illuminated object [56]. The distortion of the specially designed patterns inform of the geometric properties of the object. Calibration of the projector-camera system is easily done by capturing images of a known planar pattern [57]. With the ability to use off-the-shelf components, its use with a single projector and camera, and a robust and simple calibration method, SLI is positioned to be an accurate, fast, and cost-effective breast surface imaging system.

2.3 “-ilities” of Near-infrared Imaging Systems

In general, medical instruments can be approached from multiple viewpoints [21]. They can be classified according to clinical medicine specialties (pediatrics, cardiology, radiology, etc.), the principle of transduction (ultrasonic, electrochemical, capacitive, etc.), or they can be studied separately for each organ system (pulmonary, nervous, endocrine, etc.) [58]. In this thesis, we focus on optical imaging in the near-infrared range. These systems can be classified as a radiology specialty with the principle of transduction being optical measurements perturbed by hemodynamics.

Table 2.1: Definition of ilities. Asterisks indicate the definition was replicated from de Weck et al., 2012 [4]

Ility Name	Definition (“ability of a system...”)
Adaptability*	to be used for other applications besides what it was designed for with an acceptable level or resource
Affordability	to be purchased with minimal investment
Comfortability	to be used extensively while actively measuring
Conformability	to physically match the surface it is trying to measure
Extensibility*	to accommodate new features after design
Interoperability*	to effectively interact with other systems
Maintainability	to remain in working condition with minimal or no component replacement
Manufacturability	to be built using minimal components and fabrication methods
Modifiability*	to change the current set of specified system parameters
Operability	to be operated by a non-technical user
Portability	to be transported to another location with minimal resources
Reconfigurability*	to change its component arrangement and links reversibly

We intentionally have not chosen a particular organ system to focus on so as not to limit the potential application of optical imaging.

We will compare the three **NIR** imaging systems in terms of their system lifecycle properties, or ilities [4]. While it is true that any system has a set of design criteria based on signal, environmental, medical, and economic factors that impose constraints based on their specific use, ilities are typically not primary functional requirements of a system. Rather, ilities often manifest themselves after a system has been put to initial use. Unlike other engineering properties that are more easily tested in a laboratory, ilities tend to not receive as much focus [4]. However, when discussing the potential translation of a medical technology to outside the laboratory setting, ilities better inform of wider system impact with respect to stakeholders and are better indicators of user needs [59]. The ilities we will use in this thesis to compare across the three **NIR** systems are defined in Table 2.1.

CHAPTER 3

MOBILE-PHONE-BASED OXIMETER (MOXI)

3.1 Introduction

Every year, nearly 3 million newborns die within the first 4 weeks of life in LMICs [60]. Respiratory complications, such as birth asphyxia, and congenital heart defects, such as Tetralogy of Fallot (which results in Blue Baby Syndrome – a condition caused by low tissue oxygenation), are among the major causes of death at birth for neonates. In addition, over 17% of the post-neonatal child deaths are caused by childhood pneumonia and other acute respiratory infections, accounting for 4 million deaths per year for children under age 5 [61]. These conditions often lead to low arterial and tissue oxygenation [62]. Many of these complications are easily screened, diagnosed, and continuously monitored in most facilities in developed countries using a pulse oximeter, a device to measure arterial blood oxygen saturation (SpO_2) levels using low-power light based on near-infrared spectroscopy (NIRS).

Finger-clip-based pulse oximeters, however, are difficult to use on small fingers. Newborn-specific pulse oximeter probes, often sold as disposable parts, can cost up to \$100 USD, and require a more expensive oximeter system to read and display results [63, 64]. These designs thus have an extremely limited presence in first-level clinics in LMICs. In recent years, portable NIR devices have been reported, but they generally have high costs due to sensitive charge-coupled device (CCD) cameras and stand-alone image acquisition software [65], or still require the use of a finger-clip [66, 67]. Many factors, primarily high acquisition and maintenance costs (Table 3.1),

Table 3.1: Barriers to adoption of new medical devices in LMICs

Rank	Barrier to Adoption
1	Acquisition Costs
2	Spare Parts
3	Consumables
4	Reliable Power
5	Infrastructure
6	Training

have hindered the adoption of portable diagnostics tools [68].

A silver lining comes from the Pew Global Research Center, which reported that smartphone ownership in LMICs rose from 21% to 45% between 2013 and 2018, making smartphone networks the fastest growing infrastructure in LMICs [69]. By capitalizing on the ubiquitous presence of smartphones worldwide, we aim to develop phone-camera-based and phone-communication facilitated NIRS devices to measure tissue oxygenation, directly addressing the barriers to adoption in Table 3.1. These smartphone-based devices can address the current limitations of conventional pulse oximeters, including newborn-unfriendly clip designs, acquisition and maintenance costs of disposable probes, and the need for frequent disinfection due to direct skin contact. Leveraging smartphone features such as cameras, LEDs, and wireless communication along with their power and computation will pave the way for point-of-care (POC) smartphone-based diagnostic tools.

In this chapter, we establish the feasibility and accuracy of three smartphone-based approaches to monitoring oxygenation. In order of decreasing the complexity of hardware, the first design (D1) is a Bluetooth wireless oximeter board with a dedicated pulse oximetry chip [Figure 3.1(b)]. The second design (D2) measures tissue oxygen saturation (StO_2). It functions by imaging light attenuation in tissue through a slit on a circuit board carrying LEDs [Figure 3.1(c)]. The third design (D3) is a paper filter covering half of the field of view of a smartphone camera [Figure 3.1(b)]. Both D1 and D3 designs utilize our in-house developed mobile phone application [Figure 3.1(a)] to monitor heart rate (HR) and SpO_2 . The three devices, along with a screenshot of the mobile phone application, are seen in the figure below. Although we include details on D1 and D2 for completeness, when we refer to the MOXI system, we are referring to the D3 design.

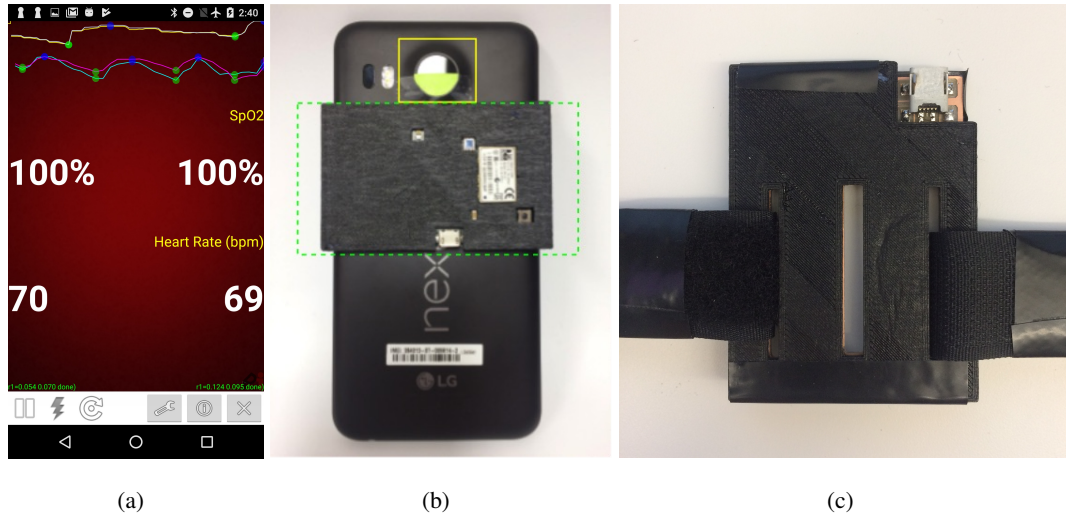


Figure 3.1: (a) Screenshot of Moximeter mobile application simultaneously capturing D1 and D3 data. (b) D1 (green, dashed) and D3 (yellow, solid) mounted on a smartphone phone. (c) D2 board with cover.

3.2 D1: Bluetooth Reflectance Pulse Oximeter

3.2.1 D1: Reflectance Board Hardware

The D1 design works similarly to a clinical-quality pulse oximeter, except the optodes are placed on the same side of the finger. A photodiode captures the diffuse reflection of the light emitted from two onboard LEDs (640 and 940 nm) in order to estimate SpO_2 . This reduced form factor, non-finger-clip design makes pulse oximetry measurements more newborn-friendly. The D1 board makes use of a low-cost (\$3.5 USD) dedicated analog front-end ([AFE4490](#)) pulse oximeter signal-processing chip (AFE4490 Integrated Analog Front-End, Texas Instruments, USA) and a microcontroller (ATMega32u4, Atmel, USA) communicating via the serial-peripheral interface ([SPI](#)) communication protocol. The $40 \times 40 \text{ mm}^2$ rigid printed circuit board ([PCB](#)) can be battery-powered or powered by a mobile phone using a male-to-male USB cable.

3.2.1.1 Optode settings for Neonates

In reflectance measurements, the distance between the sources and detector determines the depth of photon propagation. Given the larger fingers of adults compared to neonates in our initial studies (Massachusetts General Hospital approval is for use on adults with subsequent tests on

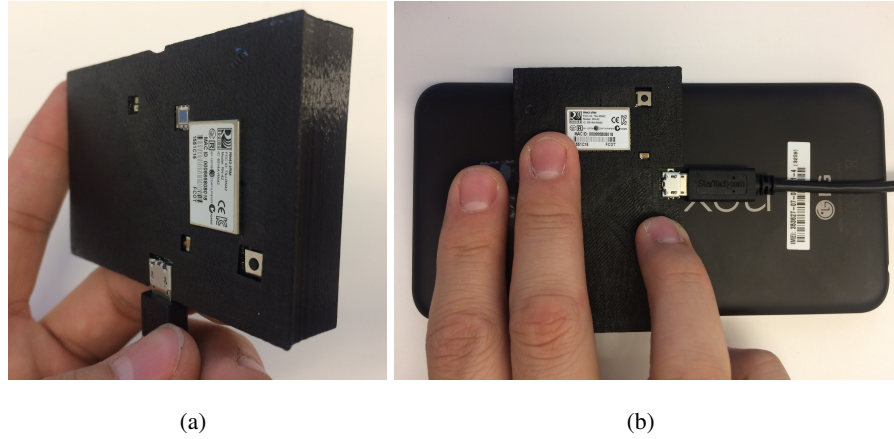


Figure 3.2: (a) D1 phone mount. (b) Simultaneous capture of D1 and D3.

neonates), the current reflectance board has optodes optimized for an adult finger by using a large source-detector distance of 17 mm. This was empirically chosen based on sweeping the source-detector (**SD**) distance from 2.54 to 15.24 mm in 2.54 mm increments (0.1 inches to 0.6 inches in 0.1-inch increments based on the breakout board). The highest signal-to-noise ratio (**SNR**) at this distance was obtained when driving the **LEDs** at 25 mA. Both 10 and 50 mA resulted in smaller amplitudes of the **AC** component of the signals due to low photon detection and photodiode saturation, respectively. The same trend is seen with the **SD** distance where being too close or too far leads to weak signals or photodiode saturation. Although set to 17 mm for the pilot tests with adults, when used on neonates, the **SD** distance should be decreased to account for their smaller finger sizes.

3.2.1.2 Phone Mount

The D1 board is placed over a Nexus 5X smartphone using a custom mount [Figure 3.2(a)]. The mount not only holds the D1 board onto the phone but also prevents users from touching the active electronics of the **PCB**. The mount is 3-D printed out of polylactic acid (**PLA**). The side panels that grip onto the phone have gaps designed to avoid accidentally pressing the volume and power buttons on the sides of the smartphone. The D1 board is press fit onto two small round tabs on the inside, eliminating the need for extra tools. The flat side of the mount is 0.2 mm thick to allow maximum surface contact of the optodes onto the finger. Holes on the mount allow access to the reset button of the board, as well as allow the Bluetooth chip to protrude outside for better signal quality. The D1 board is mounted off-center to the smartphone to accommodate the longer length

of the middle finger compared to the index finger. This allows both fingers to lay comfortably flat during simultaneous capture of D1 and D3 signals [Figure 3.2(b)]. The D1 board is powered by a USB male-to-male cable connecting the board to the smartphone’s battery.

3.2.2 D1: Reflectance Board Software

An Android phone application called Moximeter, written in Java, was developed to process the received signals from the D1 and display the results on the phone. Register values of the **AFE4490** were set to 25 mA for each optode and a 500 Hz corner filter was applied post-amplification. A long pulse repetition frequency of 250 Hz allows for dynamic averaging of 16 samples per data point by the analog-to-digital converter (**ADC**) to increase **SNR**. Bluetooth communication transmits data between the D1 board and the phone. The phone application displays the signals for the red and **IR** channels at the top of the screen. The signal sample-per-second (in Hz) is dynamically estimated and the **PPG** waveforms are processed in real-time using embedded C-code for maximum efficiency to obtain the oxygen saturation values. The real-time signal processing includes a built-in signal filtering algorithm, a peak detection algorithm, an algorithm to estimate **HR**, and an algorithm to compute **SpO₂** using a transmission pulse oximeter calibration model [70]. The real-time **HR** and **SpO₂** values are displayed in the Moximeter graphical user interface (**GUI**) [Figure 3.1(a)].

3.2.2.1 Noise Removal

Unlike a transmission finger clip where the optodes and finger are coupled, a reflectance-based measurement is more prone to noise and artifacts since the finger being sampled can move independently of the optodes. To reduce this noise, 16 readings of red and **IR** readings are sampled by the **AFE4490** prior to sending an average value to Moximeter. The sampling is done onboard to maintain our 60 Hz sampling rate. Additionally, a 5 ms delay has been added between the **SPI** transfer calls by the microcontroller to allow the **AFE4490** to stabilize. This stabilization prevents the loss of data and decreases the likelihood of garbled measurements. As an added precaution, our processing of data workflow now incorporates a mean filter in addition to our bandpass filter to remove any unwanted “chirps” or spikes in data.

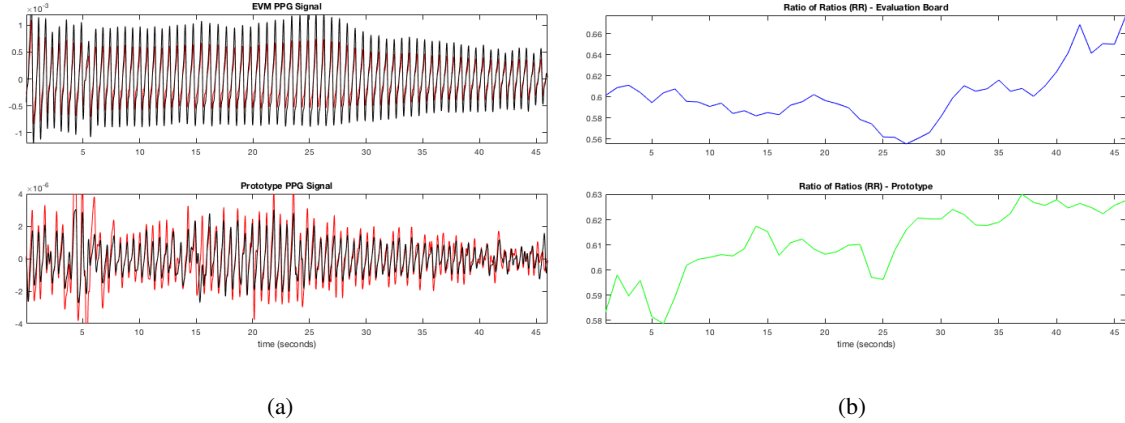


Figure 3.3: (a) Photoplethysmogram signals from evaluation module board and D1 design. (b) Ratio-of-ratios in blue (evaluation module) and green (D1 Device).

3.2.2.2 Independent Source Control

The receiver channel of the board is made up of a differential current-to-voltage trans-impedance amplifier followed by a current digital-to-analog converter (**DAC**). The amplifier has programmable a feedback resistor (R_F) and a capacitor (C_F) to form a low-pass filter for the input signal current. The output voltage of the amplifier includes the **AC** component and a component resulting from ambient light leakage. The **DAC** attempts to amplify only the **AC** component of the **PPG** signal. By systematically varying R_F , C_F , and the transmitter reference voltage for each optode, we are able to determine the **AFE4490** configuration that maximizes the **AC** components of both red and **IR PPG** signals, independently. Since the **RR** is based on the amplitude of the **AC** component of the **PPG** signals, increasing the **AC** range with optimized **AFE4490** configurations allows for more sensitivity in **RR** calculations and thus more accuracy in **SpO₂** readings.

3.2.3 D1 Results

To evaluate the D1 prototype, we compared the obtained signals from our device against simultaneously acquired signals from an evaluation module (**EVM**). The **EVM** captures **PPG** signals through transmission via a finger flip on the middle finger. The index finger of the same hand was placed over the optodes on the D1 device. The **PPG** signals in Figure 3.3(a) were simultaneously captured from the D1 device and from the **AFE4490 EVM** during a 46-second breath-holding procedure. Signals were band-pass filtered using a sixth-order zero-phase Butterworth filter

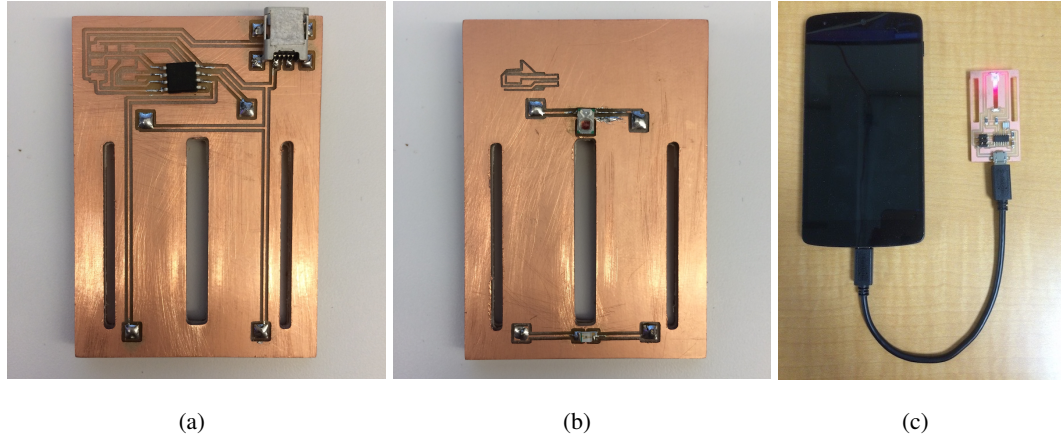


Figure 3.4: (a) Top side of D2 circuit showing USB connector and microcontroller. (B) Bottom side of the D2 circuit showing deep red (top) and red (bottom) LEDs. (C) D2 board powered by a smartphone and an on-the-go USB cable.

to remove out-of-bound noise (0.2 to 5 Hz). As shown in Figure 3.3(b), RR (Equation 2.2) increases as SpO_2 decreases due to the larger difference between extinction coefficients of oxygenated hemoglobin (HbO) and de-oxygenated hemoglobin (HbR) at red versus IR light. The pairwise linear correlation coefficient, R , between the two ratio-of-ratio signals in Figure 3.3 is 0.4856.

3.3 D2: Single Slit Oximeter

3.3.1 D2: Single Slit Hardware

The D2 design is a compact, low-cost, non-contact, and wearable LED-based illumination module to quantitatively measure StO_2 . The D2 design is made from a $53 \times 28 \text{ mm}^2$ circuit board with a $2 \times 20 \text{ mm}^2$ imaging window (the “slit”) [Figure 3.4(a)]. Two LEDs (640 and 730 nm) are mounted facing the skin at opposite sides of the long dimension of the slit [Figure 3.4(b)]. A 730 nm wavelength was chosen because IR light is not visible in the smartphone complementary metal-oxide semiconductor (CMOS) sensor. Moreover, HbO shows a similar absorption at the two wavelengths and HbR has a higher absorption at 640 nm than at 730 nm.

A micro-USB connector is added to provide power while a microcontroller (ATtiny85, Atmel, USA) controls the LED timing [Figure 3.4(c)]. Four of the eight pins on the microcontroller are used by the in-service programmer (ISP) to program the board using the Master-In-Slave-Out (MISO), Master-Out-Slave-In (MOSI), Serial Clock (SCK), and reset (RST) pins. Power

and ground each have a dedicated pin, leaving two analog pins available for the red and deep red LEDs. The use of analog pins allows us to use pulse-width modulation (PWM) to drive the LEDs. By varying the pulse width, we can control the time an LED is on and control its intensity. The microcontroller has a max output of 40 mA per pin, allowing the LEDs to be connected without the need for resistors. The board is programmed by holding the ISP pins onto the pads without soldering, allowing us to remove the programming pins after programming and reducing the board thickness. In total, the only four components on the D2 milled circuit board are the two LEDs, the microcontroller, and a USB female header for power.

The D2 design is made of two milled copper boards placed back-to-back. This has two main advantages. First, it allows the ability to easily swap out any broken LEDs if they break during use without having to mill out all the traces. Secondly, the LEDs are soldered directly to the underside of the board, allowing them to be in direct contact with the skin to minimize specular reflection. The entire board is encased inside a 3-D printed PLA cover. Velcro straps on the edges of the milled board allow the D2 design to be comfortably worn [Figure 3.1(c)].

3.3.2 D2: Single Slit Software

The microcontroller is programmed to cycle between three stages at one-second intervals. After securing the module with an elastic Velcro strap and powering the board with a USB cable, the microcontroller automatically begins cycling between the red LED on, deep red LED on, and no LEDs on, each for one second, indefinitely. The one-second interval with no LEDs on is used to capture background data. The diffuse-reflection profile across the slit of both wavelengths can be measured directly by taking a video of the slit opening using the smartphone camera controlled by our Moximeter application. The three intervals from the video stream are automatically detected by comparing intensity values at the ends of the slit. A moving bin average is used to estimate StO_2 changes.

3.3.3 D2 Results

Here, we propose to use the linear slope of the log-scaled image intensity along the slit as a surrogate marker to correlate with tissue oxygenation changes. This slope can be easily computed in real-time on low-power devices such as mobile phones.

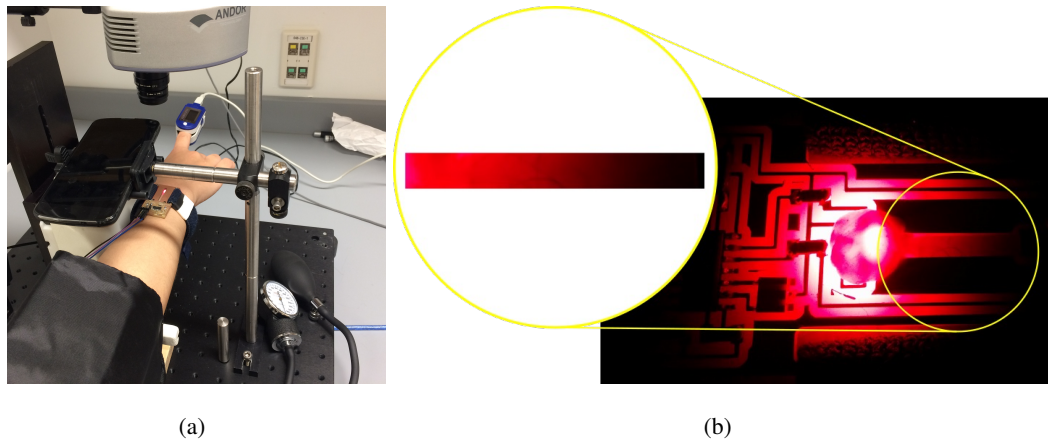


Figure 3.5: (a) Nexus and Andor camera experimental setup. (b) Example cropped slit image for analysis.

3.3.3.1 Protocol and Setup

A Nexus 5 Android phone and an Andor electron-multiplying charge-coupled device (**EMCCD**) camera (Luca-R, Andor, UK) were both mounted above the slit region and used to acquire video recordings simultaneously [Figure 3.5(a)]. The cameras recorded at 10.8 (Andor) and 30 (Nexus) frames per second while the red and deep red **LEDs** alternated every second. Data were captured in a dark room with the phone screen brightness set to the lowest setting. The subject held onto a handle during data gathering to minimize motion artifacts. An example of the acquired image (cropped using MATLAB) can be seen in Figure 3.5(b). Slit images were analyzed frame by frame for each camera. A blood occlusion experiment was performed using a standard pressure cuff. Prior to data capture, the pressure was increased to 200 mmHg and held for 20 seconds. After 20 seconds of data capture, the pressure was released.

3.3.3.2 Benchtop Results

The linear slope time courses obtained from the Andor and Nexus cameras for 640 and 730 nm are shown in Figure 3.6. Each marker in the plot is obtained by averaging the frames during the 1 second a particular **LED** is on. The vertical green line indicates the point of pressure release. The overall shape of the slope profile from the Nexus camera is similar to the Andor camera in both 640 and 730 nm. The pairwise linear correlation coefficients, R , between the two cameras are 0.8627 (640 nm) and 0.7986 (730 nm). The increase in slope immediately following the pressure

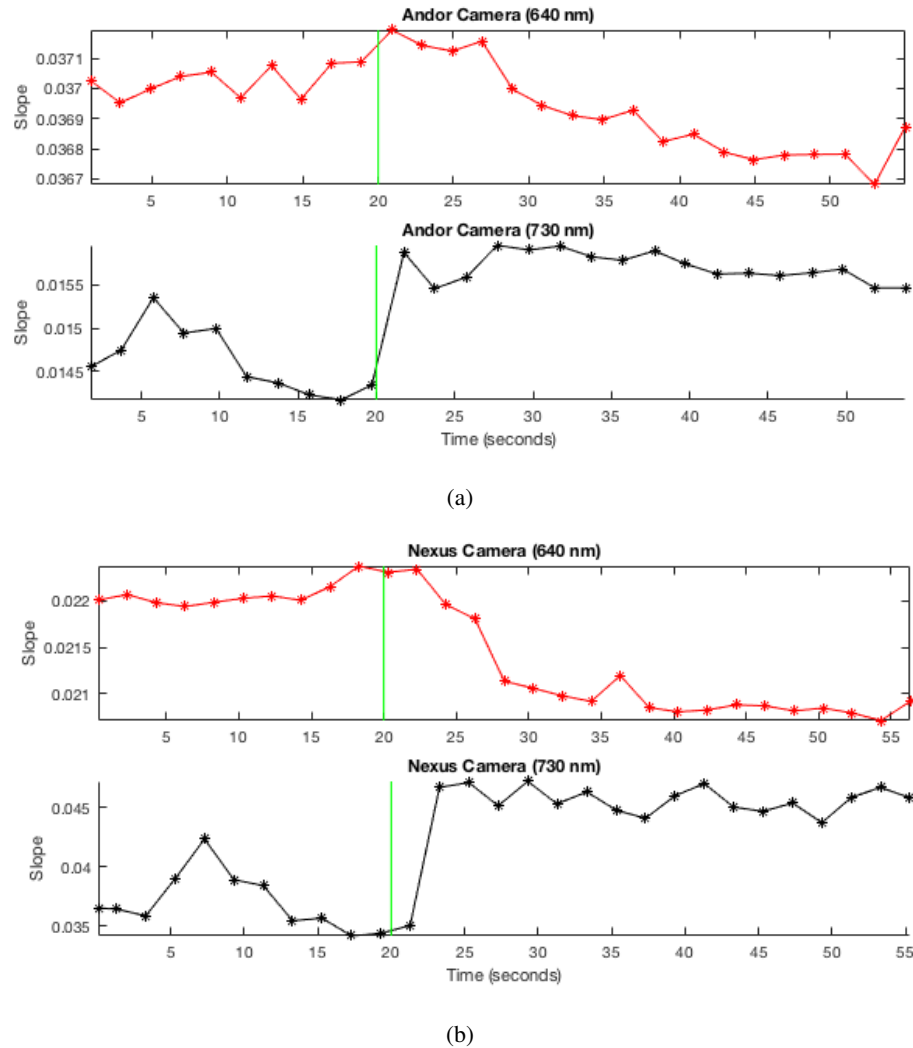


Figure 3.6: Intensity attenuation slopes for the Andor (a) and Nexus (b) camera data. Top (640 nm) and bottom (730 nm) rows show the averaged attenuation slope of the log-scaled light intensity over time within a selected window. The vertical green lines mark the point at which pressure from the cuff was released.

release is expected due to the higher absorption coefficient of the total hemoglobin that rushes in. These results suggest that a low-cost phone camera is capable of capturing blood volume and oxygenation changes in tissue.

3.4 D3: Paper Filter Pulse Oximeter (MOXI)

The D3 design is a broadband reflection pulse oximeter that utilizes a smartphone's embedded flash **LED** as the source and the smartphone's camera as a detector. An ultra-low-cost paper filter covering half of the camera's field of view manipulates the original spectra by attenuating certain wavelengths (Figure 3.7(a)). The hypothesis is that when a finger is placed over the phone's camera and **LED**, the observed spectra differences combined with the tissue absorption spectra will make it possible to make spectroscopic measurements. Point-of-care devices like these that require no or minimal attachments provide a much greater impact on the accessibility of such devices in resource-poor regions by directly addressing the acquisition and maintenance costs that hinder technological adoption (Table 3.1).

3.4.1 Photon Propagation Simulations

3.4.1.1 MCXlab simulations

A previously segmented, high-resolution, 7 Telsa realistic 3-D finger model was used for the photon propagation simulations [71] [Figure 3.7(c)]. The original 15 components were combined to represent six tissue types: dermis, epidermis, arteries, veins, fatty tissue, and bone. We ran a series of GPU-based Monte Carlo simulations using Monte Carlo eXtreme (**MCX**) [72] using 5×10^9 photons in both transmission and reflectance mode. The detector diameter was set to 3 mm, and the source-detector distance in reflectance mode was set to 10 mm, as measured from the mobile phone's dimensions. To simulate broadband light, the optical properties of the finger tissues were swept between the wavelength band of 350 to 1000 nm in 1 nm increments, with intensity based on the measured spectrum of an Android Pixel 2's **LED**. The filtered broadband light was then further attenuated by the ratio between unfiltered and filtered spectra. The intensity was estimated by fluence.

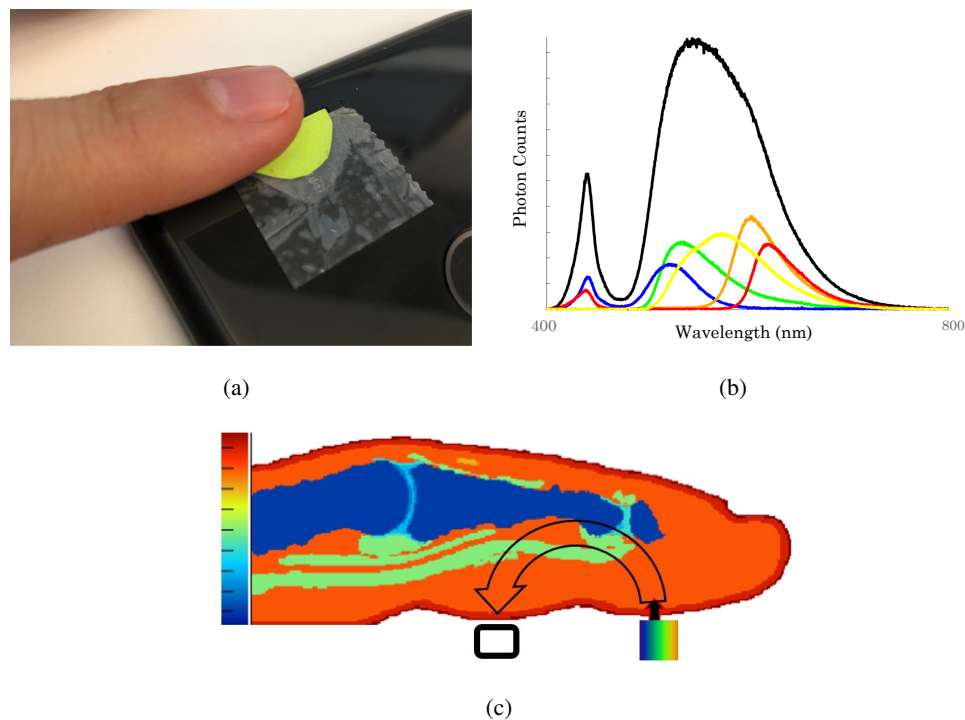


Figure 3.7: (a) D3 design in use with a finger placed over the camera after a paper filter is taped over the bottom half of the mobile phone camera. (b) Broadband spectra (black) and resulting spectra after manipulation using colored paper filters. The color line refers to the color of the paper filter. (c) Simulation setup showing finger model with six tissue types.

3.4.1.2 Optical Properties

The optical properties of the six tissue types were compiled from literature. The absorption and scattering coefficients of oxygenated whole blood, de-oxygenated whole blood, water, and melanosome were obtained from the MCXYZ.c light transport program [73]. Bone optical properties were digitized from published results [74]. Dermis and epidermis tissue optical properties were created from blood [75], oxygen [76], water [77], fat [78], and melanosome [79] volume fractions from literature [76]. Blood was assumed to have a hematocrit value of 45%. The remaining 55% is plasma, which is typically composed of 92% water and 8% food, protein, and other solids [76], but was simplified to 100% water for these simulations. Venous blood was assumed to have 70% SpO_2 . SpO_2 levels ranging from 85% to 100% are simulated by adjusting the corresponding optical properties of blood resulting from the volume fractions changes of the arteries.

3.4.1.3 Attenuation Spectra of Paper Filters

A spectrometer (Flame VIS-NIR, Ocean Insight, USA) was used to measure the spectrum of an Android Pixel 2 flash LED. Transmission spectra from paper filters of various colors, which further alter the light source spectrum, were also measured [Figure 3.7(b)]. Broadband spectra were scaled to a max arbitrary unit of 1. The green paper filter was chosen due to its capability of blocking near-infrared light while still not attenuating the original broadband light significantly. This provides a means to differentiate between the broadband light source and a filtered broadband source, which, when combined with the tissue absorption spectra, makes spectroscopic measurements using two broadband sources possible.

3.4.1.4 PPG Signal

The PPG signal, the measured intensity by the detector, was simulated by increasing the volume of the arteries in the model using a gaussian filter until a 20% change in the detected fluence was obtained at 690 nm in transmission [80]. This artery volume increase was used for both transmission and reflection modes as well as for both traditional (two-wavelength) and broadband simulations. All other tissue volumes remained constant. The resulting fluence values for both finger artery volume changes were then used to scale a discretized PPG signal [81] to create a 60 bpm oscillation optical measurement. A PPG signal was created for each SpO_2 value for each pulse oximeter mode (transmission and reflection), as well as for traditional (two-wavelength) and broadband simulations (Figure 3.8).

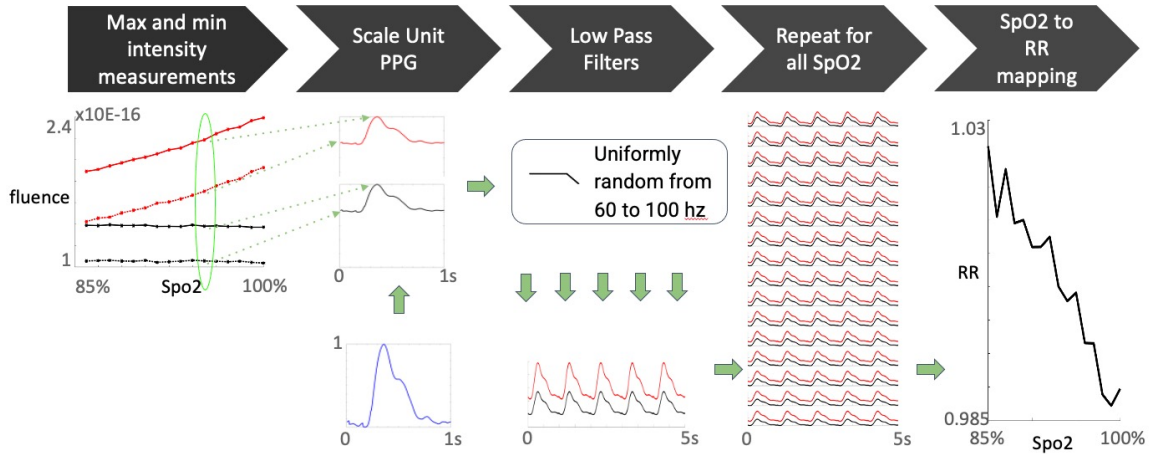


Figure 3.8: Process of creating the ratio-of-ratio to arterial blood oxygen saturation mapping in simulation. Monte Carlo simulations result in fluence measurements at various arterial blood oxygen saturation values for both wavelengths at 0 and 20% artery volume increase. An example 1 second photoplethysmogram pulse is scaled by the fluence measurements and repeated to create a time trace. Each repetition is low-pass filtered with a randomized cutoff frequency between 60 and 100 hz. The ratio-of-ratio value is then calculated from the simulated photoplethysmogram signals.

3.4.1.5 Ratio-of-ratio for broadband spectroscopy

The traditional calculation of **RR** was altered slightly to account for broadband light. For this device, **RR** is defined as

$$RR = \frac{A_{BB,AC}/A_{BB,DC}}{A_{FB,AC}/A_{FB,DC}} \quad (3.1)$$

where A is the amplitude, BB refers to the broadband **PPG** signal, and FB refers to the filtered broadband **PPG** signal of our simulations.

3.4.2 Simulation Validation Results

The **RR** values calculated from the fluence values at the detector locations from the **MCX** simulations are shown in Figure 3.9. Traditional two-wavelength transmission simulations showed a typical linearly decreasing relationship between **RR** and **SpO₂** as expected. The difference between the maximum and minimum **RR** is 0.0795. In traditional two-wavelength reflection mode, the range of **RR** dropped to 0.0519. This indicates that transmission mode is more sensitive to changes in **RR**, and thus to changes in **SpO₂**, than reflection mode.

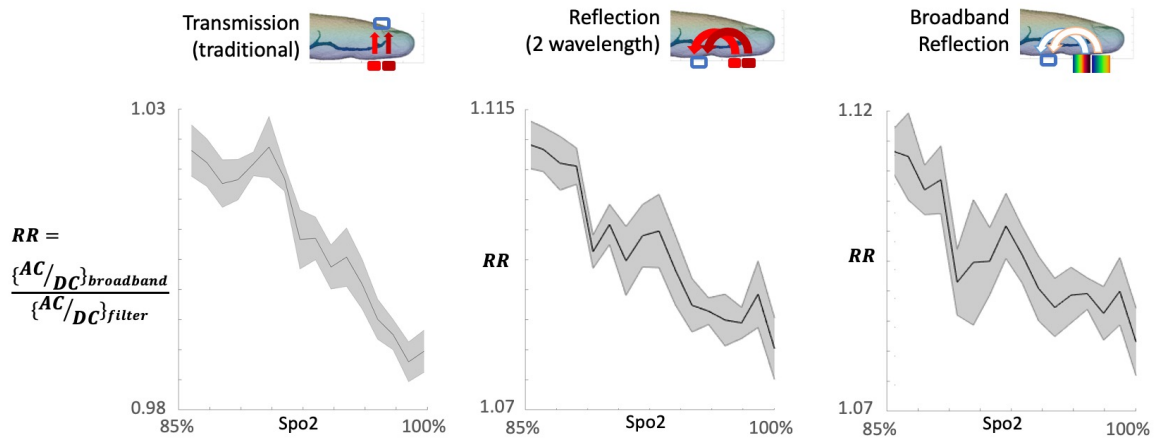


Figure 3.9: Results of ratio-of-ratio mapping to arterial blood oxygen saturation based on Monte Carlo simulations. The curves are shown for two-wavelength simulations in transmission, two-wavelength simulations in reflection, and broadband simulations in reflection.

For broadband simulations, the range of **RR** was 0.013 for transmission mode, dropping by nearly six times as compared to traditional transmission simulations. The difference between **RR** ranges in traditional and broadband simulations in reflectance mode was about an order of magnitude, with a maximum **RR** range of 0.005 for broadband reflectance simulations.

Despite the sensitivity of a traditional two-wavelength transmission pulse oximeter simulation being fifteen times higher than the broadband reflectance simulation, the broadband reflectance simulation relationship between **RR** and **SpO₂** is still linear. These results validate our hypothesis that our smartphone-based pulse oximeter can differentiate between **SpO₂** values using the embedded broadband light from the smartphone's **LED**, as long as the sensitivity of the smartphone camera is large enough. Additionally, extra care must be taken to block ambient light and reduce motion artifacts to be able to decouple physiological changes from environmental ones.

3.4.3 Pilot clinical testing

A clinical study was designed to simultaneously capture measurements from a mobile phone low-cost paper filter broadband pulse oximeter and a reference device (Rad87, Masimo, USA). The study was conducted on twenty-nine healthy volunteers at the Massachusetts General Hospital Translational Clinical Research Center.

3.4.3.1 Breath-holding procedures

The clinical pulse oximeter finger clip was attached to the middle finger of the right arm while the index finger rested on the lens of the Pixel 2 smartphone modified to carry a paper filter that partially covers the lens. Measurements were collected simultaneously using our in-house developed mobile application, Moximeter. Subjects were asked to exhale and hold their breath for as long as they comfortably could. This was repeated three times, with two minutes to recover in between. Subjects were told to begin breathing immediately if their oxygen saturation according to the clinical pulse oximeter device dropped below 90%.

3.4.3.2 Data Processing

The Moximeter application controlled the smartphone's **LED** flash and sampled the camera view at 15 Hz. The average pixel intensities of the top and bottom quarter of the camera's image were used to generate the broadband and filtered broadband **PPG** signals. Moximeter then applies a Chebyshev Type II filter to remove the systemic heart rate signal. The **PPG** signals are then band-pass filtered using a sixth-order zero-phase Butterworth filter to remove out-of-bound noise (0.2 to 5 Hz). **RR** is calculated over a 1-second sliding window along the entire time trace. In order to directly compare with the Masimo pulse oximeter, which only outputs **SpO₂** readings every second, data from the mobile application needed to be converted to **SpO₂** values. This was done using Dr. Hossein Hakim's conversion [70]: $SpO_2 = 110 - 25 \times RR$. This conversion assumes a transmission pulse oximeter. Our clinical dataset was fit to the Masimo pulse oximeter to generate a new **SpO₂** calibration curve of $SpO_2 = 109.59 - 54.69 \times RR$. Readings were averaged within 1-second bins to directly compare the 1 Hz Masimo **SpO₂** values.

3.4.3.3 Pilot Test Results

Selected results from this pilot study are shown in Figure 3.10. In many cases [Figures 3.10(a), (b), and (c)], we observe a strong overall correlation between **SpO₂** readings from our paper filter (red lines) and the finger-clip style Masimo clinical grad pulse oximeter readings (green lines). Figure 3.10 shows that our D3 design captures the expected delay in **SpO₂** drop after initial breath holding. Additionally, the D3 readings correlate well with the minimum **SpO₂** values determined by the Masimo baseline.

In other cases, while the overall trends seem to agree, the range of the **SpO₂** values differ between the D3 design and the finger-clip oximeter [Figure 3.10(d)]. This seems to indicate that the

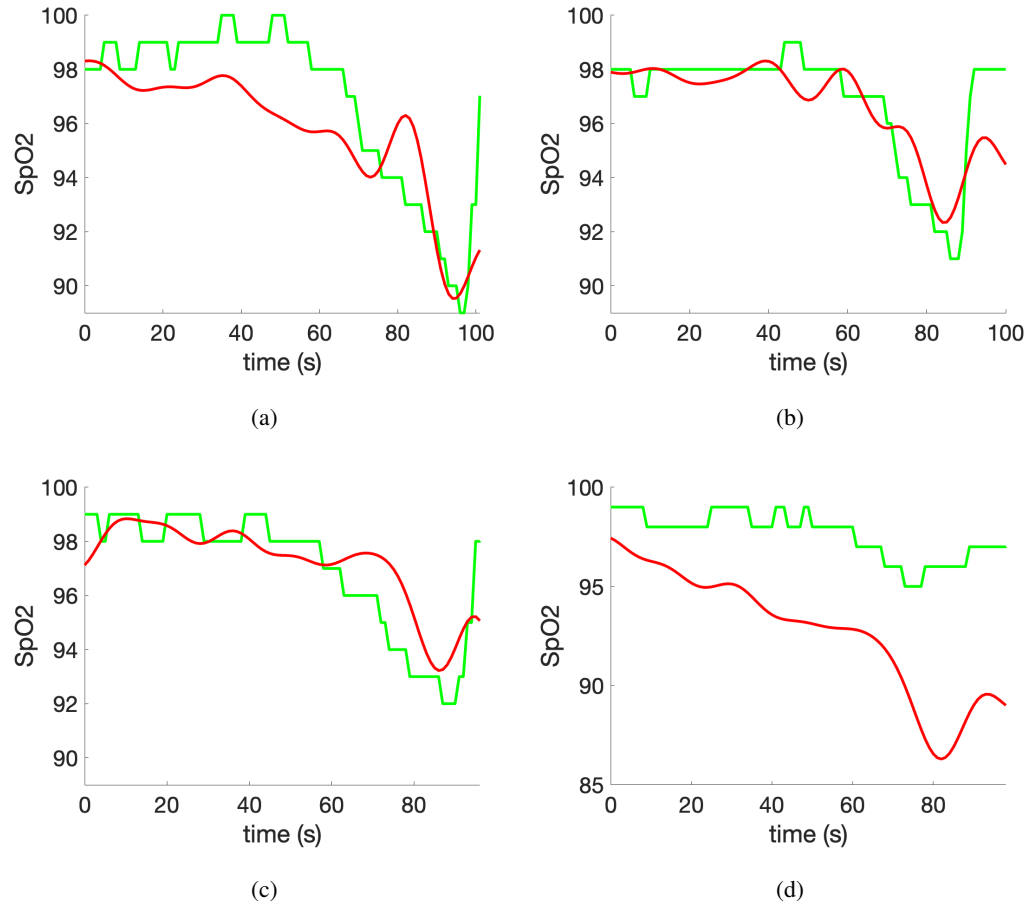


Figure 3.10: Results from comparison of our broadband reflectance-based oximeter with a clinical grade pulse oximeter. Green lines indicate clinical pulse oximeter readings sampled at 1 Hz. Red lines indicate calculated arterial blood oxygen saturation measurements using our broadband oximeter.

RR to SpO₂ conversion may need to be better calibrated. It also indicates that our pulse oximeter prototype may be more susceptible to motion artifacts and noise to alter our SpO₂ calculations.

Due to the low-cost nature of our pulse oximeter, and the inherent motion artifact in broadband-based oximeters, the signal variability is quite high. As a result, more advanced signal-processing techniques should be further explored and make these measurements practically useful. Nevertheless, the matching between our ultra-low-cost pulse oximeter readings to the Masimo device in some of the subjects is quite encouraging.

CHAPTER 4

MODULAR OPTODE CONFIGURATION ANALYZER (MOCA)

This is part 1 of 2 of the work addressing the second challenge described in Chapter 1. This chapter will focus on Modular Optode Configuration Analyzer (**MOCA**), a software workflow created with the intention of simplifying the design of new modular **fNIRS** systems. Chapter 5 will describe the **fNIRS** system built to translate neuroimaging into natural settings.

4.1 Introduction

fNIRS is an emerging neuroimaging technique to non-invasively measure brain activity using non-ionizing light [38]. Unlike functional magnetic resonance imaging (**fMRI**) [82] that requires high-strength magnetic fields and large scanners, **fNIRS** utilizes **NIR** light to detect brain activation by measuring the associated hemodynamics. The portability of **fNIRS** positions it as a competitive imaging modality to address some of the challenges of conventional neuroimaging techniques, such as **fMRI** and magnetoencephalography (**MEG**), including a lack of wearability for continuous monitoring, limited temporal resolution, and need for subject immobility during use [83]. It has shown great promise for safe and long-term monitoring of brain activity and is increasingly used in studies for behavioral [84] and cognitive neurodevelopment [85, 86, 87, 88], language [89, 90], psychiatric conditions [91, 92], stroke recovery [93], and brain-computer interfaces [94, 95, 96].

Despite exponential growth in the number of applications [37, 97] and publications [83] in recent years, many fNIRS systems still employ fiber-based, cart-sized instrumentation [39] that place limits on both channel density and the use of fNIRS in natural environments. Although fiber-based high-density [98] and portable [99] fNIRS systems have been demonstrated, the use of fragile fiber optics cables, stationary external source/detector units [100, 101], and the need for individual and specialized headgear for specific tasks have motivated the fNIRS community to investigate more flexible modular and fiber-less designs [102, 103].

The modular fNIRS architecture is based on utilizing elementary optical source and detector circuits (modules) as repeating building blocks to form a re-configurable probe [102]. This modular architecture offers significantly improved portability, scalability, flexibility in coverage, and fabrication cost [102]. By avoiding the use of fragile optical fibers, modular fNIRS systems permit the use of light guides to directly couple light sources and detectors to the scalp, significantly reducing signal loss due to fiber coupling. The lightweight and compact modules also make wearable fNIRS and continuous monitoring in mobile environments possible [83, 104]. In addition, the ability to use both intra-module (within a single module) and inter-module (source and detector on different modules) channels allows for high-density probes with varying source-to-detector separations (SDS)s that increase measurement density and tissue depth sampling, resulting in enhanced signal quality, and easy removal of physiological noise [105].

Despite these perceived benefits, the task of designing a modular fNIRS probe can quickly grow in complexity as the number of modules increases. While parameters can be empirically determined when designing a single module, understanding the trade-offs among a large array of parameters, including module shape, module size, optode quantities, and optode locations, and each parameter's effects on the final probe can become a daunting task. Not only do most published modular fNIRS studies largely focus on the design of a single module without addressing the effect of these module- and probe-level parameters on the final probe, but the current literature also does not provide a means to compare probes composed of different module designs.

Aside from the challenges of determining these modular probe core parameters, other factors such as mechanical, ergonomic, safety, usability, optoelectronic, and data communication considerations [102] also play important roles in achieving the desired performance. For example, mechanical features such as optical coupling and electronic circuitry encapsulation must be considered alongside ergonomic considerations such as comfort, weight, and robustness. Additionally, the use of high-density light sources in such modular probes brings about additional safety considerations, such as heat dissipation, driving voltage, and battery life. Moreover, optoelectronic con-

siderations arise from the use of specialized optodes with narrow emission bandwidths, high gains, low noise, and **fNIRS**-optimized wavelengths. Not only are these specialized optodes more expensive due to their niche applications and characteristics, but they also require more complex control electronics for driving optodes and acquiring data. With such dense coverage, complex encoding strategies such as frequency [106] multiplexing become a necessity for obtaining high-density data acquisition to achieve sufficient spatial and temporal resolution. Finally, while previously reported modular **fNIRS** systems often employ daisy-chain communication protocols to connect multiple modules on a single bus [107, 108, 109, 110, 111], the design of physical inter-module connections [112], the synchronization method between modules [102], and the transfer of acquired data become increasingly complex with high module counts and branching connections.

Along these lines, a number of **fNIRS** data analysis packages exists [113, 114, 115]. However, they focus on the statistical analysis of the data [115, 113, 114] to enhance its quality and provide guidance on post-processing steps such as motion artifact correction [113]. While some other tools exist to assist in the probe design [116, 117, 118, 1], most of these tools are designed to work in a highly constrained design space, where the probe parameters are mostly pre-determined by the user. As a result, the best practices and trade-offs in modular probe design such as tessellation, connection, or re-orientation are poorly explored and understood. Therefore, the community is in great need of an easy-to-use software tool to assist the exploration of and quantitative comparisons among countless parameter choices in a modular probe design and to perform a limited degree of optimization within a well-constrained configuration.

A fully-automated probe design and optimization pipeline is impractical without application-dependent design constraints. Instead, we report a simplified, easy-to-use software toolbox to help designers navigate the vast parameter space of a modular probe. We also share a number of fundamental modular probe design strategies, discovered through our explorations via this toolbox, that are not widely recognized or previously studied. The entire workflow has been implemented into an open-source, MATLAB-based toolbox called Modular Optode Configuration Analyzer (**MOCA** [119]). **MOCA** supports a list of commonly used module shapes, user-defined optode layouts, and **ROI** coverage, and can produce quantitative performance metrics such as distributions of **SD** separations, sensitivity maps, and spatial multiplexing groupings. These performance metrics also allow comparisons between different designs of modular probes. Although **MOCA** is not designed as a fully-automated software that produces “optimal” probes regardless of application, its unique capability to describe and sweep modular probe parameters in operator-guided interrogations offers valuable perspective to start approaching the complex modular hardware design problem and

make informed comparisons between well-constrained design choices.

The remainder of the paper is outlined below. In Section 4.2, we discuss the relevant design considerations when developing a modular probe using MOCA. We specifically focus on the parameterization of the modules, processes required to assemble modules into functional probes, and related performance metrics for system characterization and comparisons. In Section 4.4, we demonstrate MOCA’s capability in designing full-head probes using a variety of module shapes and compare their trade-offs regarding channel density, SD separations, and average brain sensitivities. Furthermore, we utilize MOCA to showcase potential improvements to published fNIRS probes by altering module orientations, spacing, and staggering layouts. In Section 4.5, we highlight a number of generalizable design strategies that were discovered via our experiments using MOCA, including the importance of considering module orientations, tiling strategies, and module spacing tuning, among others.

4.2 Modular Probe Parameters and Performance Metrics

A diagram showing the overall design process of a modular fNIRS system is shown in Figure 4.1. Specifically, the three parts describing MOCA’s workflow are 1) the design parameters describing a single module design, 2) the processes and parameters used to assemble the modules into a probe, and 3) the derived performance metrics used to characterize the resulting probe. MOCA starts with the definition of essential module parameters (shown in the left column in Figure 4.1), applies those parameters along with probe-level constraints to a probe-generation process (center column in Figure 4.1), and derives quantitative performance metrics of the resulting probe (shown in the right column in Figure 4.1). Arrows in Figure 4.1 define dependencies between the derived performance metrics and the input parameters. For example, in order to calculate the probe’s channel distribution, one must define the module geometry, ROI, and optode layout design parameters.

4.2.1 Essential module-level design parameters of fNIRS modular probes

The basic building block of a modular probe is an fNIRS module. It is typically in the form of an optoelectronic circuit made of a rigid [107, 108, 111, 120] or rigid-flex [121, 122] substrate with on-board light sources, optical sensors, auxiliary sensors, microcontrollers, and other communication electronics. A modular probe is subsequently constructed by replicating and inter-

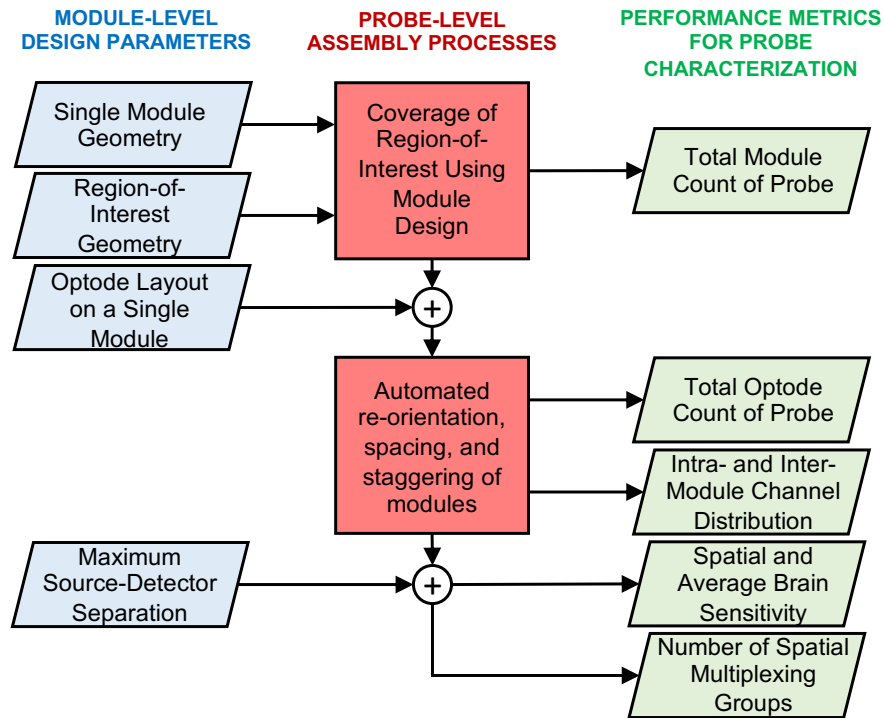


Figure 4.1: Workflow of module-level design parameters (left column; blue) used in probe-level processes (center column; red) to produce performance metrics to characterize a probe (right column; green). Performance metrics are organized top to bottom from least complex (two parameters needed) to most complex (four parameters needed). Arrows trace how parameters are used to derive specific performance metrics.

connecting multiple identical modules. Therefore, the design decisions regarding the module-level parameters are highly important and directly impact the functionalities and restrictions of the resulting probe.

4.2.1.1 Single module geometry

The shape of a module is one of the key parameters when designing a modular system. In the published literature, simple polyhedral shapes, especially equilateral polygons (square, hexagon, etc), are typically used due to their simplicity to fabricate, analyze, and tessellate over a target **ROI**. It is also possible to design probes that combine multiple polygonal shapes, such as a combination of hexagonal and pentagonal modules. Such hybrid-shape modular systems may bring advantages in tessellating curved surfaces, but they also require more complex analyses. **MOCA** supports a number of built-in module shapes including three equilateral polygons (triangle, square, hexagon). In such cases, the module edge length is the only shape parameter that needs to be defined. One should be aware that a small-sized module requires a large number of boards to cover a given area, thus resulting in higher fabrication costs and higher complexity in assembly and analysis. Moreover, a small module size also limits the maximum intra-module **SDS**. Shorter **SD** separations are known to be more sensitive to superficial tissues rather than brain activities. On the other hand, a small-module size provides better probe-to-scalp coupling when a rigid-board-based module is used. **MOCA** provides support for user-specified arbitrary polygonal modules, defined by a sequence of two-dimensional (2-D) coordinates. Subsequent analyses of these user-defined arbitrary module shapes only use the bounding box of these polygons when varying probe-level parameters.

4.2.1.2 Target regions-of-interest

An **ROI** refers to the area of the scalp directly above the cortex for which brain activities are expected to occur[123]. For simplicity, here we focus on designing probes based on the coverage of a 2-D **ROI**. For generality, **MOCA** specifies an **ROI** geometry as a closed polygon made of a sequence of 2-D coordinates. Users need to specify at least three Cartesian coordinates to define a closed **ROI**. In the future, **MOCA** can potentially be expanded to support three-dimensional (3-D) surfaces as **ROIs** through the use of 3-D surface tessellation tools, such as the Iso2Mesh [124] mesh generator and 3-D photon transport modeling tools such as NIRFAST [125] and MCX [126].

4.2.1.3 Optode layout within a single module

Optode layout refers to the spatial arrangement of optical sources and light sensors within the boundaries of a single polygonal module. In MOCA, each source and detector position is defined by a set of discrete 2-D coordinates relative to the module's center. The 2-D coordinates define the center of the active area of the light-emitting-diode (LED), laser, or photodetector. The physical dimensions of the optodes as well as the size and location of electronic components needed to drive each optode are not considered. The SD separations between all combinations of SD pairs are derived based on the optode positions.

4.2.1.4 Maximum source-detector separation and maximum short separation channel

MOCA also considers the maximum SD separation (SDS_{max}) as a key design parameter. Typically, SDS_{max} is determined by the SNR of the detected signal [127]. A large SDS has low detector sensitivity due to the exponential decay of light intensity as SDS increases. This maximum separation limits the number of inter-module channels that emerge from a particular tessellation of modules over an ROI. By default, MOCA considers any SDS below 10 mm to be a short-separation (SS) channel. This threshold can be manually changed to fit any specific optode performance or probe application. MOCA uses 30 mm as the default SDS_{max} [128, 129]. MOCA bounds the SD range by the SS channel threshold and the SDS_{max} .

4.2.2 Probe-level assembly process parameters

A modular probe is constructed when multiple modules are arranged to form a non-overlapping coverage of the ROI area. The final probe is dependent on the tessellation (the number of modules and the spacing between them) and the orientation of each individual module in the probe.

4.2.2.1 Exploring module tessellation and probe spacing

MOCA provides a process to tessellate modules over a user-defined 2-D polygonal ROI, which is generally known as the “tiling” problem in computational geometry [130]. Here, a “complete tessellation” refers to the tiling of an ROI using a single module shape without overlapping or leaving a gap in coverage. Each of the three built-in polygons (triangle, square, hexagon) have the ability to cover a 2-D area [131]. MOCA performs the tessellation by first tiling the module

shape along a horizontal axis starting at the lowest vertical coordinate of the **ROI** until the width of the row composed of adjacent modules is wider than the width of the corresponding segment of **ROI** the row is tiled over. It then repeats this row-generation process until the height of all the rows combined is larger than the maximum height of the defined **ROI**. This dimension comparison in both axes accounts for module shapes with non-vertical and non-horizontal sides. For irregular module shapes, **MOCA** uses the maximum width and maximum height of the defined polygon as the bounding box to create a tiling grid of the module over the **ROI**. Using the maximum width and height of the **ROI** as a guide for tiling ensures the full **ROI** is covered. Although **MOCA** offsets and flips the three equilateral polygon shapes to prevent gaps, irregular module shapes have inherent gaps between modules when tessellated. Additionally, **MOCA** accepts manually defined tessellations by reading a sequence of coordinates defining the center of modules to specify each individual module’s location within the **ROI**. Following tessellation, each module is assigned a unique index and an adjacency matrix is constructed to represent which modules are next to one another.

To extend the flexibility of probe creation, users can change probe spacing, the minimum distance between adjacent modules in all directions. Additionally, a module can be manually deleted from the tessellation to allow the probe to more closely follow the boundaries of the **ROI** or better represent intentional empty spaces in the probe. When individual modules are removed from the probe, the adjacency matrix is re-calculated from the resulting probe.

4.2.2.2 Guiding module orientation and connection routing

Module orientation refers to the rotation of the module along the normal direction of the **ROI** plane. In a “complete tessellation” of the three equilateral polygon shapes, **MOCA** appropriately flips and translates modules to prevent gaps and overlaps. For tessellations of irregular shapes, each module is simply placed in the same orientation as it was originally defined. After probe generation, **MOCA** allows the user to manually change the orientation of individual modules based on their assigned indices. For asymmetric optode layouts, changing the module orientation alters the **SDS** of inter-module channels, resulting in different performance metrics.

Additionally, **MOCA** creates a single sequential path to connect all modules to form a linear data communication bus, referred to as the “routing” process. In such a path, all modules are connected and every module is visited exactly once—a classic problem known as the Hamilton path [132] in graph theory. In most configurations, a Hamilton path is not unique, and computing such a path is known to be an NP-hard problem, i.e. problems that do not have a polynomial com-

plexity when the node number grows. However, due to the limited module numbers commonly used in **fNIRS** probes, an exhaustive search of the adjacency matrix can typically identify all Hamilton paths in a given tessellation with no more than a few minutes of computation. For any computed path, **MOCA** then orients each module based on the angle of a vector defined by the center of the oriented module and the center of the following module in the path. The orientation angle is relative to the horizontal axis.

4.2.3 Performance metrics to characterize probes

Each metric described below changes as module- and probe-level parameters are altered either manually or through **MOCA**'s sweeping functions. **MOCA** not only helps unravel the complex interplay between choices of different parameters but also guides the probe designer in making trade-offs between conflicting design targets—improving one metric may come at the risk of worsening another. We have chosen the following set of essential performance metrics due to their ability to easily inform a breadth of end-user probe requirements such as cost, weight, depth sensitivity, and sampling rate estimates.

4.2.3.1 Total module and optode counts

Based on the module design and tessellation, **MOCA** computes the total number of modules, n_m , needed to cover the **ROI**. In addition, **MOCA** also outputs the total number of sources (n_s) and detectors (n_d) of the final probe. All modules, sources, and detectors of an assembled probe are given unique identifiable index numbers (m_i , s_i , and d_i , respectively). Module and optode counts are performance metrics outputted by **MOCA** from which cost, weight, and power estimates can be deduced.

4.2.3.2 Inter- and intra-module channel distribution

For any assembled probe, **MOCA** generates histograms of the **SD** separations for all combinations of **SD** pairs. Particularly, it outputs separately the distribution of inter- and intra-module channels that are below the SDS_{max} previously defined by the user. These channel distributions aid the user in designing the probe based on the targeted application and population. For example, shorter channels are more applicable to infant populations. Additionally, **MOCA** outputs channel density, a metric commonly used for **fNIRS** probe benchmarking. Channel density is defined as the number of channels, $n_{channels}$, divided by the area of the **ROI** [102]. Furthermore, **MOCA** can

provide a spatial plot overlaying channels on the assembled probe, allowing for visual inspection of low channel density areas within the probe.

4.2.3.3 Spatial brain sensitivity

Brain sensitivity (S_{brain}) refers to the magnitude of the measurement signal change at a detector given a localized perturbation of optical properties of brain tissue [2]. A higher S_{brain} value suggests the probe is more sensitive to the anticipated brain activation. It is calculated from the spatial probability distribution of photons scattering through complex tissue as they travel from the source to the detector [133]. Although modeling 3-D head/brain anatomies and 3-D based light simulations have been reported, including several related works from our group [126, 124, 5, 134], we deliberately chose a simplified layered-slab head model and 2-D based probe layout as default models to evaluate a modular probe in MOCA. Such a decision was largely motivated by 1) significantly faster computation and pre-/post-processing to accommodate fast sweeping of a large parameter space, and 2) avoiding another added layer of complexity when probe design is coupled with underlying brain anatomy in a 3-D head model. A comparison between S_{brain} computed by 2-D and atlas-based analyses is provided in the Results section. Nonetheless, MOCA can export 2-D probe data to established 3-D probe modeling toolkits, such as AtlasViewer [1] and MCX [126], to perform more advanced analyses when 3-D head models are necessary.

MOCA uses a five-layer slab model consisting of tissue imitating the scalp, skull, cerebral spinal fluid (CSF), white matter (WM), and gray matter (GM) to determine the spatial sensitivity profile for each SD pair in a probe [135]. The thickness of each tissue layer in the slab is set to the average thickness of that tissue type computed using the top half of a tetrahedral brain model [6]. We define the brain region as the combination of gray matter and white matter tissues. The optical properties and resulting thicknesses for each tissue type are summarized in Table 4.1.

For each SD pair in the assembled probe, 3×10^8 photons are simulated using our in-house 3-D Monte Carlo photon transport simulator, MCX [126], using a pencil beam source and a single 1.5 mm radius detector placed at the surface of the slab at its corresponding SDS. In a voxelated grid, S_{brain} is defined as a ratio dividing the region-wise summation of the sensitivity matrix in each brain tissue region by the summation of the entire sensitivity matrix for each source-detector separation [133], i.e.

$$S_{brain}(s, d) = \frac{\sum_{r \in \Omega_{GM}} J(r, s, d) + \sum_{r \in \Omega_{WM}} J(r, s, d)}{\sum_{r \in \Omega} J(r, s, d)}, \quad (4.1)$$

Table 4.1: Optical properties used in the slab model for calculating brain sensitivity based on Fang *et al.* [5]. The thickness of each layer is derived by dividing the total tissue volume by the tissue's surface area from a tetrahedral five-tissue brain model [6]. The absorption coefficient, μ_a , is the average path a photon will travel in the medium before being absorbed. Similarly, the scattering coefficient, μ_s , defines the average path length of photons before a scattering event. Anisotropy, g, is a unit less measure of the amount of forward direction retained after a single scattering event.

Tissue Type	μ_a [mm^{-1}]	μ_s [mm^{-1}]	g	Thickness [mm]
Gray Matter	0.020	9.000	0.89	7.25
White Matter	0.080	40.900	0.84	4.00
Cerebral Spinal Fluid	0.004	0.009	0.89	2.73
Skull	0.019	7.800	0.89	3.29
Scalp	0.019	7.800	0.89	4.23

where the sensitivity matrix, also known as the Jacobian (J), is computed using the adjoint Monte Carlo method [136]. In addition to S_{brain} , MOCA also calculates the average brain sensitivity for the entire probe, $\overline{S_{brain}}$, based on all the SD separations above the SS threshold. SS channels are excluded in the calculation of $\overline{S_{brain}}$ because, by definition, they are designed to only sample superficial layers [133].

4.2.3.4 Spatial multiplexing groups

The density of assembled modular probes may impact the probe's temporal sampling rate when illuminating each source sequentially. MOCA introduces spatial multiplexing, an encoding strategy that can potentially accelerate data acquisition by simultaneously turning on multiple light sources at the same time. Because of the high attenuation of light in the head and brain tissues at large separations, MOCA can ignore the cross-talk of light sources that are far away for a given detector and assign sources into a spatial multiplexing group (SMG) so that all sources within an SMG can be turned on simultaneously. By default, MOCA uses the SDS_{max} as the minimal distance between sources. This distance, however, can be defined by the user. Notably, unlike frequency multiplexing, spatial multiplexing does not require extra energy-intensive hardware or post-measurement separation of combined signals.

The search for the SMG starts by randomly specifying a source position as the seed; a circle of radius SDS_{max} centered at the seed position is drawn and a random source outside of this circle that is at least $2 \times SDS_{max}$ away is picked; the above process repeats until no additional source can be found. Once an SMG is identified, a new source that does not belong to any existing SMG is selected as the new seed for the next SMG, and the above process repeats until every source

is allocated. The total number of spatial multiplexing groups, n_{SMG} , depends on the tessellation of the module over the **ROI** as well as the choice of the seed position. As with channels, the n_{SMG} are for a single wavelength. Thus, when estimating the total sampling rate of the probe using dual-wavelength sources, the control unit must cycle through each group twice (once for each wavelength).

In addition to n_{SMG} , **MOCA** calculates the spatial multiplexing ratio (**SMR**), defined as $SMR = n_s/n_{SMG}$. This ratio is interpreted as the acceleration factor of the data acquisition speed when using spatial multiplexing. For example, for a 20-source probe, an n_{SMG} of 5 can accelerate the data acquisition by a factor of $SMR = 20/5 = 4$ fold.

4.3 Additional Functionalities

MOCA was created as an exploratory tool to interrogate specific design parameters and reveal the trade-offs, within a well-constrained search space, regarding specific design decisions. **MOCA** possesses functions to facilitate changing probe-level parameters and exporting the desired probe for use in existing probe design tools such as **AtlasViewer**.

4.3.1 Parameter sweeping

4.3.1.1 Altering spacing between modules

An optional parameter during module tessellation is probe spacing—a uniform distance assumed between adjacent modules. The spacing sweep function varies the probe spacing within a user-defined range in user-defined increments. For the three built-in polygons (triangle, square, hexagon), spacing is increased between all adjacent sides of the modules within the probe. For arbitrary shapes, spacing is added to the horizontal and vertical sides of the rectangular bounding box. The number of modules required to cover the **ROI** is continuously adjusted as probe spacing is varied. The performance metrics for each of the resulting probes are reported by **MOCA** as a function of probe spacing.

4.3.1.2 Exhaustive search of module orientations

MOCA provides a limited orientation enumeration function to re-orient modules through a predefined number of orientations. For the three built-in polygons, the default number of re-orientations per module is simply the number of sides of the polygon. For arbitrary shapes, the

default number of re-orientations is four based on the bounding box. Additionally, a user can describe the number of orientations for any shape. **MOCA** re-orient modules in evenly spaced angle increments. An exhaustive search is performed using the number of modules in the probe and the number of user-defined orientations. Each probe resulting from each permutation of module re-orientations is characterized by **MOCA** and reported as a function of various probe layouts.

4.3.1.3 Staggering rows of modules

Staggering modules refers to shifting a row (or column) of tessellated modules in the x (or y) axis. Staggering is performed on tiling grid probe layouts. Adjusting this probe-level parameter is particularly useful for improving probes composed of modules with symmetrical optode layouts, where re-orienting modules does not affect **SDS**, or when high-density probes are needed, where probe spacing cannot be increased. A user defines both the range and increment by which to offset a particular row. Each resulting probe is analyzed and the corresponding performance metrics are calculated. **MOCA** then reports a plot of the $\overline{S_{brain}}$, spatial multiplexing ratio, and the number of channels for each staggered probe.

4.3.2 Exporting probe for use in AtlasViewer

MOCA performs its analysis of module- and probe-level parameters on an infinite slab model derived from the Colin27 atlas. When 3-D analysis is desired, **MOCA** can export the probe layout to a “.sd” file for use in “SDgui” – a built-in tool of AtlasViewer [1] used for creating and editing “.sd” files. To properly represent a modular probe layout in AtlasViewer (which treats all optodes individually without a reference to a module), **MOCA** first translates the module-level parameters by creating fixed/rigid springs between all optode pairs (source-source, source-detector, and detector-detector) within each module. These fixed springs maintain the relative optode layout within each module while permitting bending at the junctions between springs. **MOCA** then adds fixed springs between each inter-module channel (**SD** pairs between modules with distances below the SDS_{max}) to translate the probe-level parameters (spacing, orientation, staggering). As an additional constraint, **MOCA** adds flexible springs (springs of length -1) for inter-module channels above the SDS_{max} . Finally, to register the probe to the surface of the selected atlas, **MOCA** adds three dummy optodes to the exported “.sd” file. All three optodes are placed at the midpoint between the minimum and maximum x coordinates of all optodes in the probe. The y coordinate of the first, second, and third dummy optodes are set to the minimum y coordinate, midpoint, and

maximum y coordinate of all optodes in the probe, respectively. The first, second, and third dummy optodes are assigned to the Fpz, Cz, and Oz positions, respectively, in the standard 10-10 system. This places any MOCA-designed probe at the top of an atlas by default. A user can change the dummy optode anchors to re-position the probe on an atlas. The exported “.sd” file can then be loaded into AtlasViewer for placement on a generic or subject-specific atlas (Figure 4.2).

4.4 Results and Practical Examples

In this section, we first validate the S_{brain} derived from a simplified five-layer slab model against previously published atlas-based S_{brain} results [2]. Then we demonstrate how the module-level parameters of MOCA can be used to characterize and compare full-head probes composed of different choices of elementary module designs. Lastly, we show examples using MOCA’s assembly processes as investigational tools to potentially improve existing designs by altering probe-level parameters such as probe spacing, module orientations, and the staggering of modules within an assembled probe.

4.4.1 Slab-based brain sensitivity corresponds with atlas-based sensitivity

Figure 4.3 shows S_{brain} calculated using our five-layer slab model at SD separations ranging from 1 to 60 mm in 1 mm increments (blue line). We also overlay full-head averages of S_{brain} and standard deviations at 20, 25, 30, 35, and 40 mm separations from a previously published study [2] using the Colin27 atlas.

Simulations on a five-layer slab model show an increase in S_{brain} as SDS increases. Additionally, S_{brain} for SD separations below 10 mm is less than 1.17%. At 20, 25, 30, 35, and 40 mm separations, the maximum difference between the atlas-based and slab-based S_{brain} values is less than 0.6%. Figure 4.3 demonstrates that using a 2-D approximation of the ROI and a layered brain structure provides a reasonable trade-off between accuracy and computational efficiency, especially for high-density probe characterization.

4.4.2 Comparison between sample modules of various shapes.

MOCA allows the comparison of a wide range of fNIRS module designs by quantifying the effects of probe-level design parameters on a probe’s performance. As a showcase, here we report the results from a comparison of three equilateral module shapes (square, hexagon, and tri-

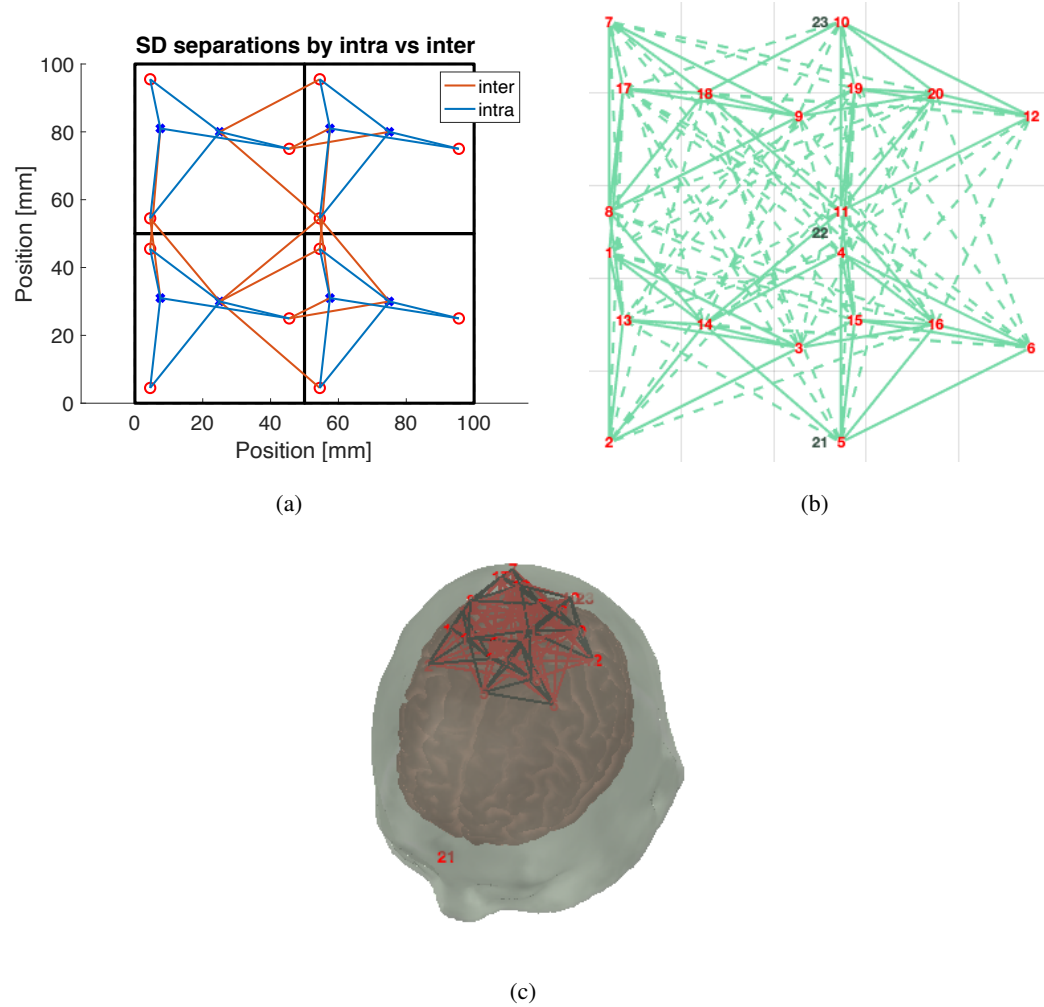


Figure 4.2: Example probe exported for use in AtlasViewer [1]. (a) A four-module probe with three sources (red circles) and two detectors (blue crosses) plotted using MOCA. Intra- (blue) and inter-module (orange) channels are shown in solid lines. (b) Imported probe in SDgui. Solid lines represent fixed springs. Dashed green lines represent flexible springs between sources and detectors. Three dummy optodes (numbered 21, 22, and 23) are shown in black. (c) The resulting probe in AtlasViewer registered to an atlas using the dummy optodes as anchors.

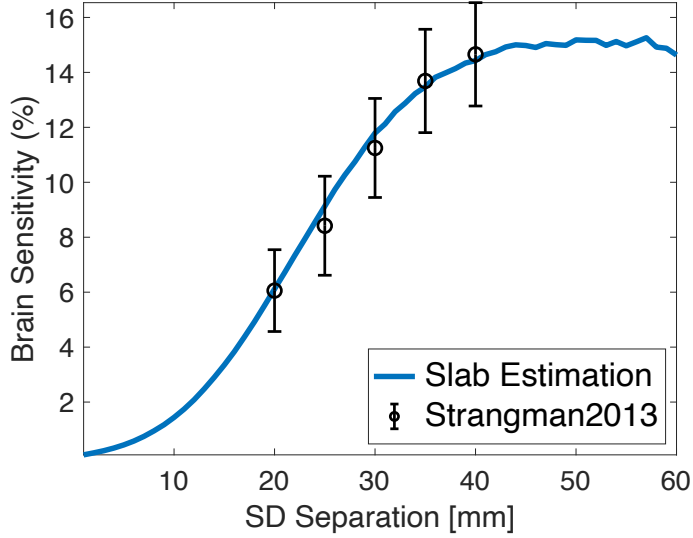


Figure 4.3: Results comparing brain sensitivity derived from finite slab models used by MOCA and atlas-based models. The blue line shows calculated brain sensitivity based on a five-layer slab model for SD separations from 0 to 60 mm in 1 mm increments. Overlaid in black are the brain sensitivity results calculated from an atlas by averaging brain sensitivity for fixed source-detector separations across nineteen locations in the international 10-20 system [2].

angle) with the same optode layout tessellated over a 200×200 mm ROI, derived from the average surface area of the top half of an adult male head [137]. Square [107, 108, 109] and hexagonal [110, 120, 111] fNIRS modules have been extensively studied in literature and are chosen here for a quantitative comparison. While an equilateral triangle has not been reported in published module designs, we include it here because of the potential suitability for better tessellation of a 3-D surface in future extensions. With this comparison, we want to demonstrate both the scalability of MOCA in analyzing full-head probes and how performance metrics change across module-level design decisions.

As mentioned above, MOCA systematically tessellates the target ROI using the module geometry and assigns each module an index number. If not considering within-module optode locations, only translation is needed for both square and hexagon modules to completely cover a region. For the triangle shape, MOCA rotates every other triangle and its optodes 180 degrees to fill the ROI without leaving any gaps. No other probe-level parameter changes are made for this comparison. Probe spacing is set to zero. The default SS threshold is set to 10 mm and the SDS_{max} is set to 30 mm. The minimum distance between sources used in calculating SMGs is set to $2 \times SDS_{max}$. To avoid simultaneously changing multiple parameters and only focusing on

Table 4.2: Summary of quantitative performance metrics derived by MOCA when tessellating the three elementary module shapes over a 200×200 mm region of interest.

Row	Performance Metric	Square-based probe	Hexagon-based probe	Triangle-based probe
1	Total modules [N]	36	42	40
2	Total optodes [N]	144	168	160
3	Total channels [N]	324	405	496
4	Intra-module channels [N]	180	237	336
5	Inter-module channels [N]	144	168	160
6	% of channels that are inter-module [%]	55.56	58.52	67.74
7	Average brain sensitivity [%]	7.52 ± 1.95	6.50 ± 2.44	8.83 ± 3.10
8	Average intra-module brain sensitivity [%]	6.44 ± 2.10	6.44 ± 2.10	6.44 ± 2.10
9	Average inter-module brain sensitivity [%]	8.82 ± 0.00	6.54 ± 2.66	9.94 ± 2.86
10	Spatial multiplexing groups [N]	9	8	13
11	Spatial Multiplexing Ratio	8	10.5	6.15

module shape, an identical optode layout made of two sources and two detectors is used in all three module designs in this example. The edge length of the square is set to 33.33 mm, determined by the average length of three previously reported square-shaped module designs [107, 108, 109]. The edge length of the hexagon and triangle is set to 20.68 and 50.65 mm, respectively, calculated to achieve the same area as the square module. The three-module designs as well as the tessellation of the hexagon-based probe over the ROI are shown in Figure 4.4. The derived performance metrics for each of the three sample probes are summarized in Table 4.2. The results that follow are only applicable to the specific module- and probe-level parameters chosen for this showcase.

4.4.2.1 Effect of module shape on channel separation distributions

Figure 4.5 shows a histogram of the SD separations of the full-head (200×200 mm area) probe composed from the three selected module shapes. Table 4.2 shows that the number of modules needed to cover the ROI varies for each shape due to the complete coverage constraint enforced by MOCA for this showcase (Figure 4.4d). Since each module utilizes the same optode layout, the intra-module channel distributions (blue bars in Figures 4.5a, b, and c) are simply scaled by the total numbers of modules needed to completely cover the ROI. The SDS of inter-module channels are dependent on the module shape, resulting in varying inter-module channel distributions between all three probes (orange bars in Figures 4.5a, b, and c).

For this particular example, the triangle-based probe reports both the highest number of total channels (Figure 4.5d) and the largest SD separations of all three tessellated probes (Figure 4.5c).

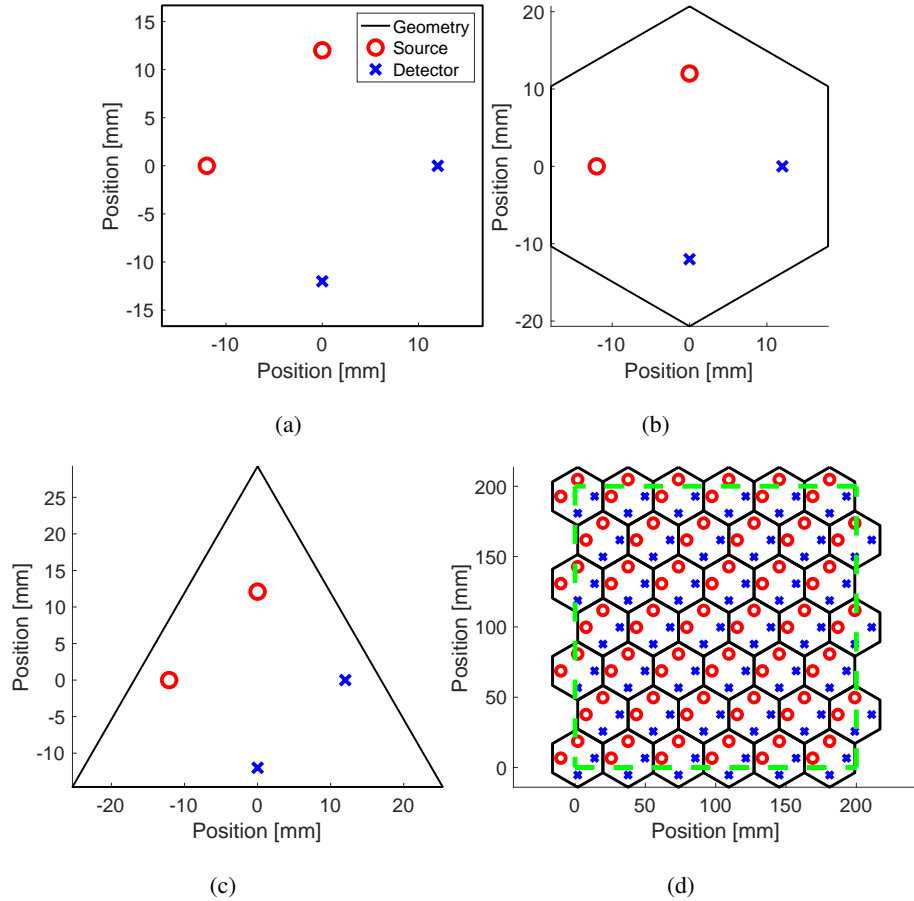


Figure 4.4: Elementary module designs used in a full-head comparison. (a), (b), and (c) show the perimeter of the square, hexagon, and triangle-based module designs, respectively. The optode layout of all three shapes is identical. Red circles represent sources while blue crosses represent detectors. (d) Tessellation of the hexagon module over an ROI. The dashed green line outlines the 200×200 mm ROI.

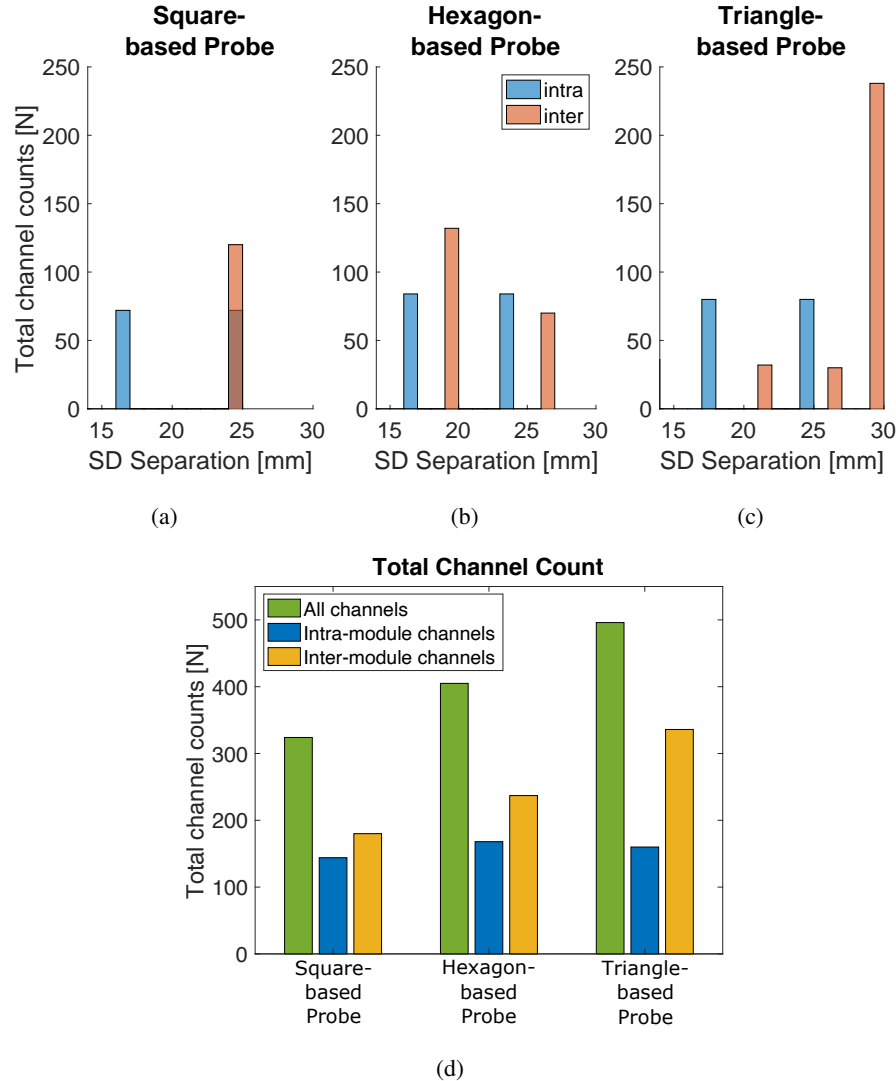


Figure 4.5: Channel distributions and total channel counts resulting from the tessellation of the three elementary module shapes over a 200×200 mm region of interest. (a-c) Resulting intra- and inter-module channel distributions for square, hexagon, and triangle module-based probes. (d) The total channel count of each probe grouped by intra- and inter-module channels.

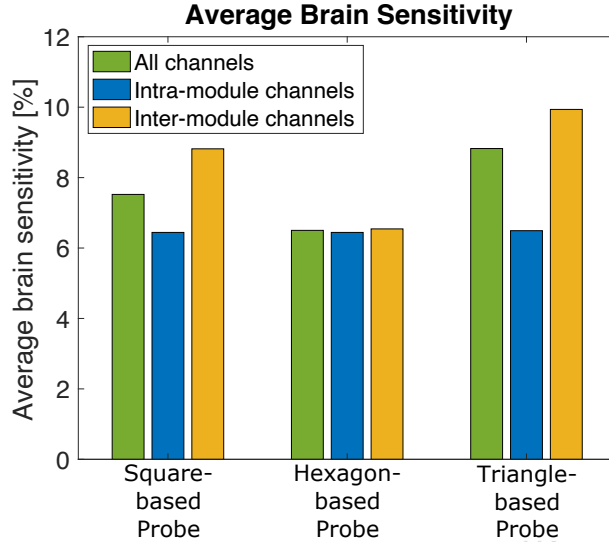


Figure 4.6: Resulting average brain sensitivity organized by intra- and inter-module channels for square-, hexagon-, and triangle-based probes tessellated over a 200×200 mm region. Short-separation channels are excluded from all calculations.

The hexagon-based probe appears to have the shortest inter-module channels (Figure 4.5b). Due to its symmetry and given the SDS_{max} setting, the square-based probe happens to have all **SD** separations at 24 mm. Notably, the triangle-based probe adds the most inter-module channels, almost twice the number of intra-module channels (Figure 4.5d), while also requiring two fewer modules than the hexagon-based probe (Table 4.2, Rows 1-5). Figure 4.5d also shows that the number of inter-module channels is greater than the number of intra-module channels for all three probes.

4.4.2.2 Combining intra- and inter-module channels for brain sensitivity

The $\overline{S_{brain}}$ values derived from the three probe designs, grouped by intra-module channels, inter-module channels, and all channels, are summarized in Figure 4.6. Only channels above the **SS** threshold and below the SDS_{max} are used. Despite having the fewest total channels (Table 4.2, Row 3), the square-based probe results in a higher $\overline{S_{brain}}$ than the hexagon-based probe. For the square- and triangle-based probes, the use of inter-module channels increases the probe's $\overline{S_{brain}}$ as compared to simply using intra-module channels alone. For the hexagon-based probe, $\overline{S_{brain}}$ computed using only intra-module channels is similar to that when using only inter-module channels (6.44% vs 6.54%). Due to having the same optode layout, the intra-module $\overline{S_{brain}}$ is the same for all three probes.

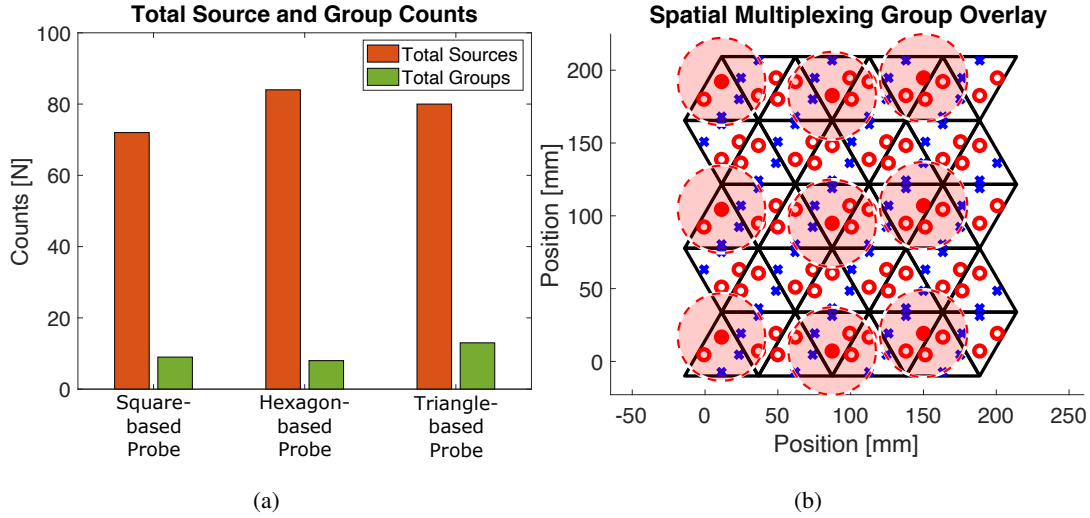


Figure 4.7: Spatial multiplexing group results from the tessellation of the square-, hexagon-, and triangle-based probes. (a) Comparison of the total number of sources (orange) and the total number of spatial multiplexing groups (green). (b) The triangle-based module tessellation with sources (red circles) and detectors (blue crosses). The dashed red circles indicate the “effective” region (30 mm radius) of each of the nine sources in the first spatial multiplexing group. The nine sources turned on simultaneously in this group are indicated by filled-in red circles.

4.4.2.3 Effect of module shapes on improving sampling rate

The total n_s compared to the n_{SMG} arising from the tessellation of each module over the ROI are compared in Figure 4.7a. The total number of sources for the square-, hexagon- and triangle-based probes are 72, 84, and 80, respectively. Figure 4.7b overlays the first SMG over the triangle-based full-head probe. Using the n_{SMG} for each probe (Table 4.2, Row 10), the SMR (the ratio between n_s and n_{SMG}) is 8, 10.5, and 6.15 for the square-, hexagon-, and triangle-based probe, respectively. This result indicates that the hexagon-based probe’s sampling rate can benefit the most when using group-based spatial multiplexing.

4.4.3 Improving existing probes through probe-level parameter alterations

The ability to compute performance metrics from basic design parameters allows users to explore probe-level alterations and potentially improve existing probes using MOCA. Here, we simulate and alter published examples to demonstrate how even simple module layout changes such as rotating selected modules, altering probe spacing, and staggering modules can potentially improve published probe designs.

4.4.3.1 Effect of optode orientation on probe characteristics

Re-orienting modules within existing probes alters the **SDS** distribution and, consequently, the probe's S_{brain} and **SMR**. In Figure 4.8, we simulate a 36 mm² square module in a probe configuration inspired by the μ NTS **fNIRS** module described in Chitnis *et al.* [107]. The modules in the initial tessellation are oriented in the same direction as in the original paper (Figure 4.8a). In our investigation, the spacing between each module is set to 5 mm and the SDS_{max} is set to 30 mm. Each module has 2 sources and 4 detectors, resulting in 8 intra-module channels per module ranging from 8 to 29 mm. A total of 256 different probe configurations result from exhaustively re-orienting each module individually by 90 degrees. Without losing generality, a subset of 128 layouts are shown in Figure 4.8b to show the range of the variations.

Of the 256 possible layout configurations, 8 of those layouts result in a maximum average brain sensitivity of 9.87%. These 8 layouts also achieve the minimum number ($n_{SMG} = 4$) of spatial multiplexing groups. The intra- and inter-module channel distribution and channel count resulting from the **MOCA** analysis of the original probe layout are shown in Figure 4.8d. Figure 4.8c shows the same 4-module probe but constructed with the bottom-left and top-right modules rotated 90 degrees clockwise, corresponding to layout number 66 in Figure 4.8b. Using **MOCA**, the spatial channel plot overlaid onto this re-oriented probe shows a denser coverage of the center of the **ROI** compared to the original probe layout. The channel count distribution of this re-oriented probe is shown in Figure 4.8e. As expected, the intra-module channels in Figure 4.8a and Figure 4.8c are identical. However, re-orienting the two modules produces a shift towards longer separation inter-module channels that are known to be more sensitive to brain tissues. The number of inter-module channels within the 10 to 20 mm range decreases from 8 to 4 and the number of 29 mm separation inter-module channels increases from 2 to 12 upon re-orienting the 2 modules. The re-orientation of modules not only allows the probe to have more long-separation channels, it also increases the total number of inter-module channels from 14 to 20 (Figures 4.8d and e). Additionally, $\overline{S_{brain}}$ of the probe increases from 8.56% to 9.87% (Figure 4.8f) while the number of spatial multiplexing groups, and subsequently the probe's sampling rate, remains the same.

4.4.3.2 Effect of probe spacing on probe performance

Probe spacing—the distance between edges of adjacent modules in a probe—is a parameter that can vary the resulting channel distribution and channel density of a probe by altering the relative distances between optodes on neighboring modules. To investigate the effect of this pa-

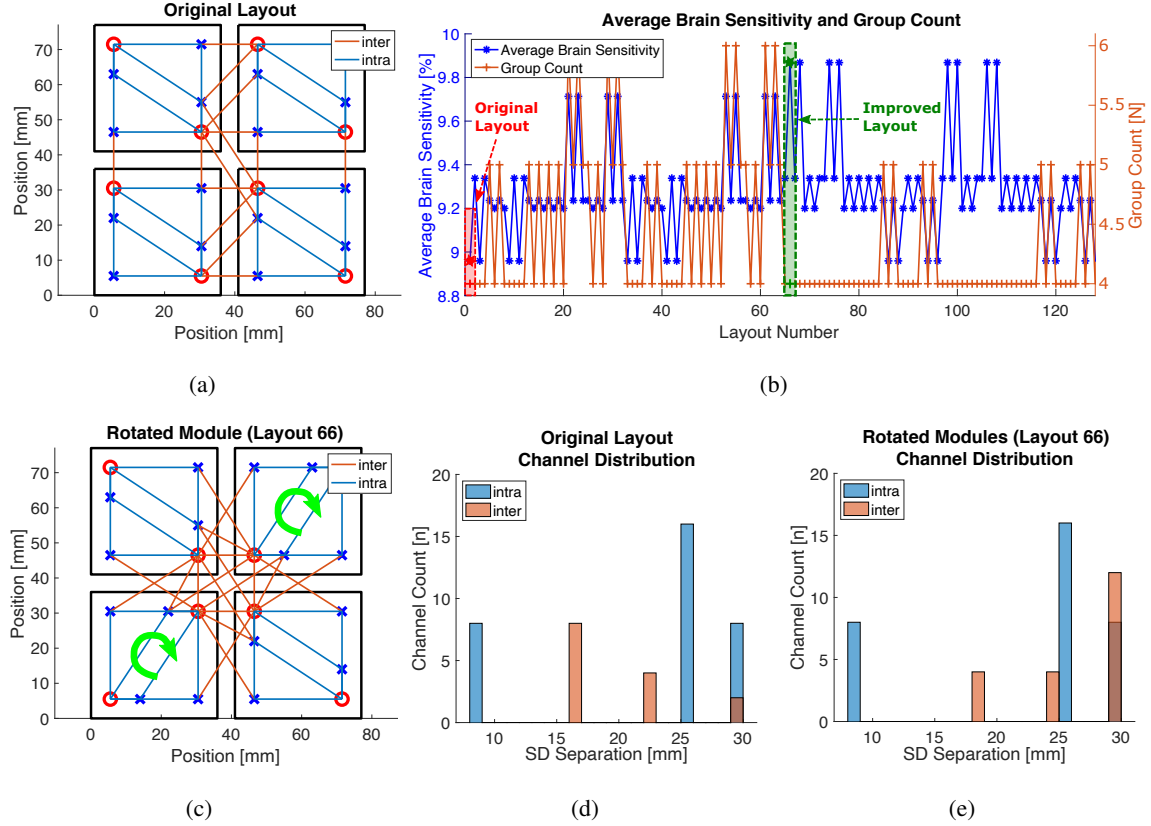


Figure 4.8: A 4-module probe simulated using MOCA. (a) All modules are oriented in the same direction. Red circles represent sources and blue crosses represent detectors. An exhaustive search of all combinations of orientations for each of the four modules results in 256 possible layouts. The average brain sensitivity and number of spatial multiplexing groups for the first 128 layouts are shown in (b). The original layout (layout number 1) is highlighted in the red square. An example layout with the maximum possible brain sensitivity (layout number 66) is highlighted in the green square. (c) A visual representation of layout 66 with the bottom-left and top-right modules rotated 90 degrees clockwise with respect to orientation in (a). Intra- and inter-module channel distribution resulting from the original layout is shown in (d). Channel counts resulting from the probe configuration in (c) are shown in (e). In both channel distribution histograms (d, e), intra- and inter-module channels are shown in blue and orange, respectively. Dark orange indicates overlapping histogram counts.

parameter, in Figure 4.9, we simulate the probe layout described by Zhao *et al.* [111], which utilizes hexagonal-shaped LUMO **fNIRS** modules developed by Gowerlabs [138]. The length of each side of the hexagonal-shaped module used in our investigation is set to 18 mm and each module contains three sources and four detectors. The SDS_{max} is set to 30 mm. A uniform spacing is set between all adjacent modules. Probe spacing is varied from 0 to 30 mm in 1 mm increments.

When all modules are densely packed with a spacing of 1 mm, the probe results in 328 total channels (184 of which are inter-module channels), an $\overline{S_{brain}}$ of 5.95%, and 12 **SMGs**. When the probe spacing is increased to 6 mm, the number of channels and spatial multiplexing groups remain the same while the $\overline{S_{brain}}$ increases (Figure 4.9b). The increase in $\overline{S_{brain}}$ arises due to the overall increased distances between sources and detectors of inter-module channels which sample deeper into the brain tissue. This results in a local maximum $\overline{S_{brain}}$ of 7.87%.

When we increase probe spacing to 8 mm, the inter-module channel separations increase to above the SDS_{max} . This decreases the number of “usable” inter-module channels and the probe’s $\overline{S_{brain}}$. The **SMR** remains unchanged between 6 and 8 mm probe spacing. Above 11 mm, the increase in probe spacing increases the relative distance between adjacent sources, allowing more sources to be turned on at the same time and decreasing the n_{SMG} needed. This trend continues as we increase probe spacing. Consequently, the probe’s $\overline{S_{brain}}$ reaches a minimal plateau of 3% at 15 mm spacing and beyond because only intra-module channels above the **SS** threshold remain within the **SD** range (Figure 4.9b). Similarly, since modules are further apart, the n_{SMG} continues to drop which increases the **SMR** (and the sampling rate of the probe when spatial multiplexing encoding is utilized). At 29mm spacing, the **SMR** value is 12 due to only 3 spatial multiplexing groups needed (one for each of the 3 sources on each module).

4.4.3.3 Effect of staggering modules on probe characteristics

Staggering adjacent modules within a high-density probe can increase inter-module **SD** separations to improve performance. To demonstrate the effect of staggering on the resulting probe, in Figure 4.10 we simulate a 42 mm^2 square module in a 3×1 layout configuration inspired by M3BA modules [108]. Each of our simulated modules contains two sources and two detectors. The probe was staggered by translating the center module between 0 mm and 42 mm along the horizontal axis.

In Figure 4.10a, we overlaid the intra- (blue) and inter-module (orange) channels over the three-module probe. The resulting channel distribution shows 12 intra-module channels at 28 mm

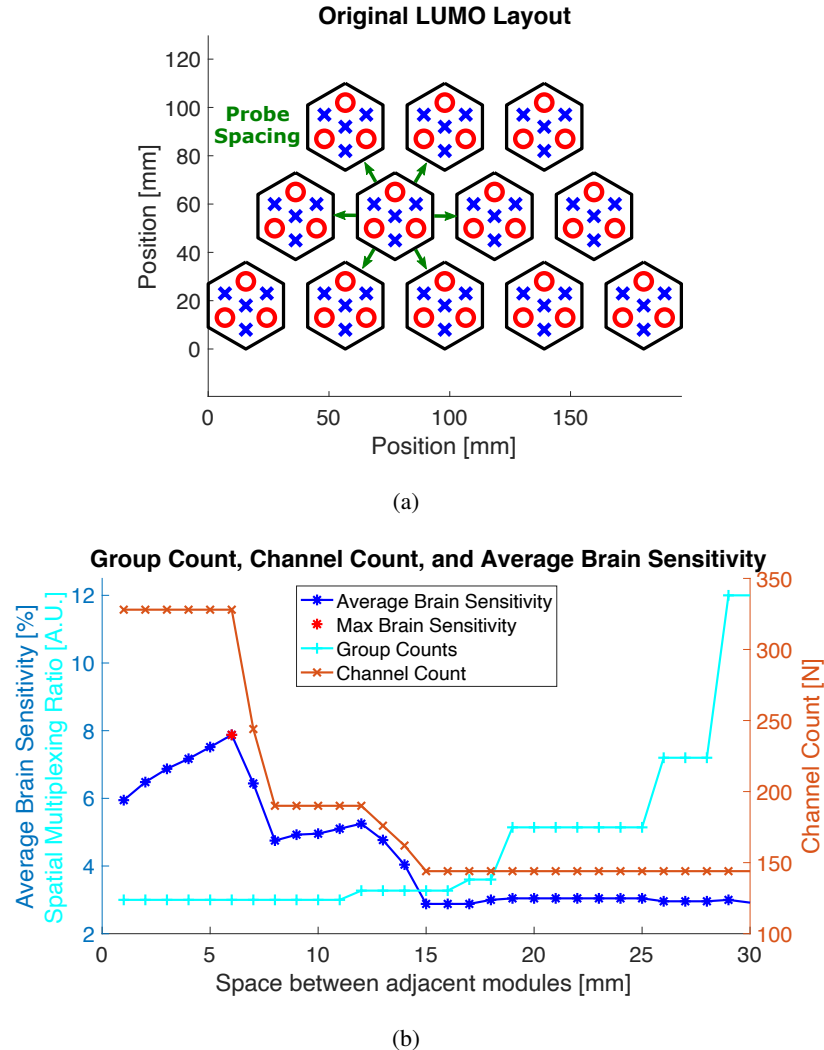


Figure 4.9: An analysis of hexagonal modules in a twelve-module probe. (a) Green arrows indicate the distances between modules as probe spacing varies. (b) The total channel count, average brain sensitivity, and the spatial multiplexing ratio at probe spacing values between 1 and 30 mm. Module orientations are held constant.

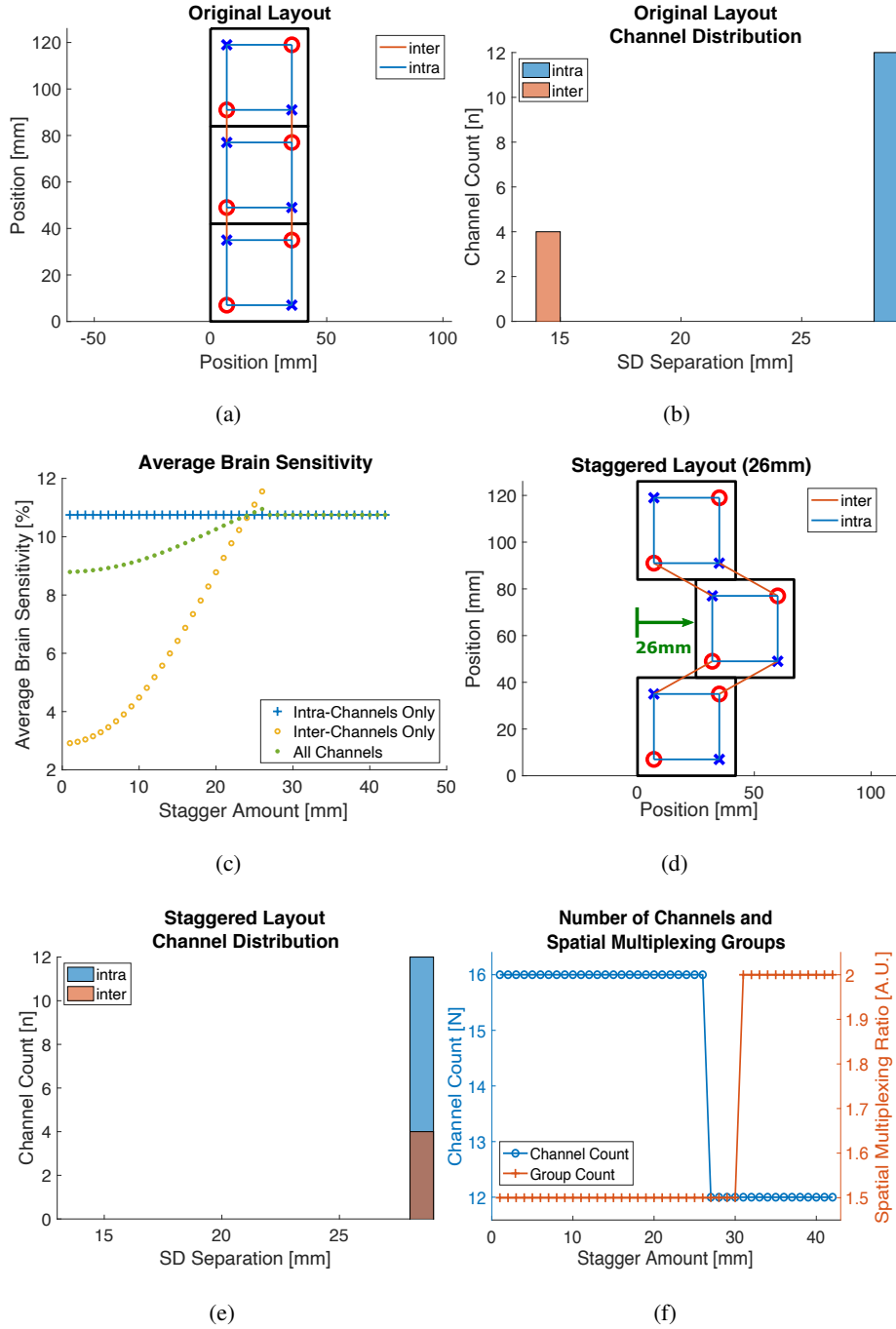


Figure 4.10: An analysis of square modules in a three-module probe. (a) A traditional three-module tessellation. Red circles represent sources and blue crosses represent detectors. (b) The resulting intra- and inter-module channel distribution from the probe layout in (a). (c) The average brain sensitivity for each layout resulting from module staggering separated by intra- and inter-module channel contributions. (d) The center module staggered by 26 mm, resulting in increased channel separation for inter-module channels, as shown in (e). (f) The total channel count and the number of spatial multiplexing groups of the probe layout as the center module is staggered between 0 and 42 mm.

and 4 inter-module channels at 14 mm SD separations (Figure 4.10b). The $\overline{S_{brain}}$ of this probe using all channels is 8.79% (Figure 4.10c). When analyzed separately by intra- and inter-module channels, the $\overline{S_{brain}}$ using only intra-module channels (10.75%) is larger than the $\overline{S_{brain}}$ when using only inter-module channels (2.9%) since in this tessellation intra-module channels are larger and probe deeper into the tissue.

In Figure 4.10c, we show the effect of staggering the tessellated module layout by translating the center module along the horizontal axis. This alteration increases the inter-module channel separations. Consequently, the $\overline{S_{brain}}$ due to only inter-module channels increases until the inter-module channel separations are larger than the SDS_{max} . The $\overline{S_{brain}}$ using all channels increases from 8.79% in the original tessellation to a maximum of 10.95% in the staggered tessellation at 26 mm. The n_{SMG} between the two layouts remained the same until a staggering amount of 31 mm at which point the sources are far away enough to group them together (Figure 4.10f).

4.5 Discussion

Through the case studies shown in the above section, we demonstrate the high complexity in designing a modular probe, where even adjusting a single parameter may have a profound impact to other parameters as well as the overall performance. Despite the fact that MOCA only permits operator-guided parameter interrogation in a well-constrained problem, the results from the above experiments did reveal a number of important design strategies that were not previously discussed in literature, including the effect of module re-orientation, fine-tuning the space between modules, and module staggering to potentially improve existing fNIRS probes.

Figure 4.5 reveals that, despite having the same optode layout, probes composed of different module shapes covering the same ROI result in different channel distributions. Although the inter-module channels are identical between modules, the resulting total number of channels is related to the number of modules needed to cover the ROI. The effect of module shape on channel distribution is complex and requires a tool like MOCA to thoroughly investigate. Certain module geometries result in optodes closer to the module's edges, effectively shortening inter-module channels in completely tessellated probes. Because the optode layout in Figure 4.4 is not completely symmetric and each module shape is an equilateral polygon, each individual module can be re-oriented without overlapping while maintaining the complete tessellation of the probe. While not altering intra-module channel distributions, these orientation configurations spatially alter channel locations and alter inter-module channel separations. The results from Figure 4.5 also show how

some individual module shapes may be more appropriate for certain subject populations. For example, the high count of 19 mm inter-module channel separations in the hexagon-based probe makes it better suited for infant populations. An important takeaway is that the number of inter-module channels of an assembled probe is not a simple multiplicative factor of the number of intra-module channels. These results demonstrate the dependency a probe's derived characteristics have on module shape even when different modules have the exact same optode layout.

The results in Figure 4.6 provide a counter-example where higher channel density due to increased inter-module channels may not necessarily improve all performance metrics of a probe. Despite having fewer total channels than the hexagon-based probe, the square-based probe results in a higher average brain sensitivity ($\overline{S_{brain}}$) due to larger inter-module channel separations. This reveals the trade-offs in performance metric improvement, emphasizing the need for S_{brain} to be considered in conjunction with channel distribution when comparing probes. Additionally, this analysis reveals that the use of inter-module channels in addition to intra-module channels does not always lead to increased S_{brain} for probes based on different module shapes. In fact, the use of only inter-module channels increases the average penetration depth for the square- and triangle-based probes due to the larger channel separations. However, for the hexagon-based probe design in this example, Figure 4.6 demonstrates that the contribution to $\overline{S_{brain}}$ from using only intra- or only inter-module channels differed by merely 0.1%. These results show that adding inter-module channels to intra-module probes will not always result in improved $\overline{S_{brain}}$. Thus, users of this particular hexagon-based probe may benefit from the simplicity and faster sampling rate of using only intra-module channels rather than implementing a potentially complex data acquisition method to capture inter-module channels. Although ignoring inter-module channels can increase the sampling rate without affecting S_{brain} for this particular probe, it does result in fewer channels and lowers the channel density of the probe. Through this complex example, we show that it is non-trivial to consider all constraints in a modular probe. MOCA is positioned as a tool to help designers challenge hypotheses, explore alternative designs, and quantify various trade-offs.

Figure 4.7 indicates that the hexagon-based probe can achieve the highest sampling rate among the three configurations if a spatial multiplexing encoding strategy is implemented. The frame rate of a sequential encoding strategy is dependent on the total number of sources (n_s) because each source needs to be turned on and sampled once. Spatial multiplexing allows multiple sources within a group to be turned on simultaneously, allowing the sampling rate to increase by a factor of n_s/n_{SMG} , defined as the **SMR**. Therefore, despite having the lowest sampling rate when sampled sequentially due to the highest n_s (Table 4.2, Row 1), the hexagon-based probe has the

fastest sampling rate of the three probes when spatial multiplexing is used due to the low n_{SMG} (Figure 4.7a). These results demonstrate that a probe’s sampling rate can be increased not only through firmware changes or advanced electronics but also by using different module shapes with the same optode layout.

While MOCA’s ability to change module-level parameters helps design new fNIRS modules, its ability to sweep through probe-level parameters helps potentially improve existing ones. Figure 4.8 shows how probes based on published modules can potentially improve $\overline{S_{brain}}$ at no increased cost and without re-designing modules by altering the orientations of modules that make up the probe. The orientation changes in layout 66 (Figure 4.8c) increase the channel density at the center of the ROI, but also increase the number of inter-module channels by 43%. The emerging inter-module channels also have larger SDS and contribute to an increase in $\overline{S_{brain}}$ without changing the SMR. The re-oriented probe in Figure 4.8c is only a representative case of how a 2×2 probe composed of square modules can be potentially improved and is exhaustive only because the number of possible orientations of each of the 4 modules was limited to 4, resulting in $4^4 = 256$ probe layouts to analyze. Additionally, the re-orientation of modules causes changes to performance metrics due to the asymmetry of the optode layout within each module. If the optode layout was symmetric, re-orienting modules would have no effect on either inter- or intra-module channels.

In Figure 4.9, we investigated the effect of spacing between modules on the derived performance metrics of a probe composed of hexagonal-shaped modules. The results suggest that varying module spacing does have an impact on $\overline{S_{brain}}$. Since optodes are generally placed near the edges of the modules to maximize intra-module channel separations, dense probes with modules near one another tend to have shorter inter-module channel separations. This trend becomes more apparent as the size of the module increases. Increasing the probe spacing increases the distance between optodes on neighboring modules, thus increasing the $\overline{S_{brain}}$ in the process. This increase in $\overline{S_{brain}}$, however, has a local maximum. As shown in Figure 4.9, further increasing probe spacing leads to a drop in the number of inter-module channels as their SD separations become greater than the separation limit (SDS_{max}). Additionally, increasing the distance between modules reduces the number of multiplexing groups (n_{SMG}) which increases the SMR and consequently the probe’s sampling rate. Once the probe spacing exceeds the user-specified SMG diameter, one source on each module can be turned on at the same time because each source would be outside the other’s “effective” region. Because the distance between sources on the same module does not change, a different SMG is required for each source within a module. Thus, the limit to the minimum n_{SMG} is equal to the number of sources on a single module, revealing a minimum improvement in sampling

rate due to spatial multiplexing encoding. Compared to a sequential sampling strategy, a spatial multiplexing encoding strategy will increase a probe's sampling rate by at least a factor equal to the number of sources on one module. Figure 4.9 shows that probe spacing can both alter n_{SMG} to help meet sampling rate requirements and alter inter-module channel separations to meet channel distribution needs.

Figure 4.10 shows that staggering a probe layout can increase $\overline{S_{brain}}$ in dense probes. Simulations using a published module shape [108] with zero probe spacing results in inter-module channels of 14 mm separations. These channels are too long to be SS channels and too short to be long-separation (LS) channels. Staggering spatially increases inter-module channel separations while maintaining the compactness of a probe (Figure 4.10c). This improvement works with square or rectangular modules since staggering is done by translating user-specified modules along a horizontal or vertical axis. For module designs with symmetrical optode layouts, we recommend staggering probe layouts by translating every other module row by half of the module's maximum width in one axis (Figure 4.10f). This ensures the optodes from the translated module are well separated from modules of the adjacent rows.

The results above are derived from investigating the module- and probe-level design parameters that MOCA currently supports. However, this only represents a small subset of the general parameters previously used in evaluating a modular probe [102]. For example, user feedback-based design parameters not yet accounted for in MOCA include conformability (a module's ability to conform to a curved surface), subject comfort, and safety limits such as operating voltage and heating effects. Source output power and module weight each require external instrumentation measurements while noise-equivalent power and dynamic range calculations require lab-specific phantoms. Power consumption depends on the type of optodes used as well as the control electronics of the individual module while a probe's battery life can be adjusted using existing off-the-shelf components. Each of these design parameters are based on specific electronic or material components chosen for a particular module design. MOCA was built to easily scale and incorporate more complex mechanical-, ergonomic-, safety- and experiment-specific considerations in the future as those design parameters are evaluated.

There are limitations to MOCA's current minimal subset of design parameters. First, the ability to re-orient, increase spacing, or stagger modules assumes that modules can be connected in any orientation. This is true for many published modular designs where cables of different lengths can be easily connected to the top of a module, but does not necessarily apply to more sophisticated designs that have embedded printed flex connectors or utilize headgears with pre-determined

mounting locations. Second, **MOCA** does not currently support multiple module shapes within the same probe or different optode layouts on different modules. Third, **MOCA**’s channel count output does not include wavelength count as a multiplier. This approach allows one to quickly scale the channel distribution and channel counts when dual-wavelength or triple-wavelength sources are utilized. Similarly, the n_{SMG} is also defined for a single wavelength. Thus, when estimating the total sampling rate of the probe using multi-wavelength sources, the control unit must cycle through each group multiple times (once for each wavelength). Fourth, **MOCA**’s analysis is based on the coordinates of the center of an optode’s active area and does not account for the actual size of the optode package, the shape of the optode’s active area, or any master control unit needed to control a series of modules. Despite being able to place optodes near the edge of modules in **MOCA**, designers may face constraints in practice imposed by the fabrication process due to board materials, sizes, and electrical routing needed to drive these optoelectronics. In general, module shapes with large interior angles allow optodes to be placed closer to the module’s perimeter. Fifth, **MOCA**’s probe-level functions are but one method of interrogating parameters in a systematic way. These functions vary parameters in discrete increments (fixed number of orientations, a set spacing range, and user-defined translation amounts) and therefore only explore a subset of all potential probe layouts. They do not determine an optimal probe configuration—they assist in improving existing probes by adding design constraints (holding module-level parameters constant) and allowing a user to identify design choices that improve performance for their particular application. Finally, **MOCA** can output 2-D optode layouts but relies on other existing software, such as *AtlasViewer* [1], to perform 3-D head contour registration. It does, however, automatically add spring relationships to embed modular aspects into an exported probe. For example, the distance between all optodes (both sources and detectors) within a module is fixed, while inter-module channels can vary slightly. This ensures that a physically rigid electronic module does not transform when registered to a surface. In addition, the performance metrics output by **MOCA** are currently based on a 2-D probe layout and do not account for changes in **SDS** if the probe is “wrapped” on the 3-D surface of a head [112]. Consequently, 2-D-derived metrics may underestimate the number of channels when a probe is made to conform to the scalp. This may result in an increase in the number of total inter-module channels for a probe. However, by working in 2-D, **MOCA** can both help unearth design and performance relationships, as well as drastically constrain the vast potential design space by helping researchers converge on the module- and probe-level parameters that most impact performance.

CHAPTER 5

MODULAR OPTICAL BRAIN IMAGER (MOBI)

5.1 Introduction

Neuroimaging techniques have advanced our fundamental understanding of human brain function [139]. However, brain activations often exhibit complex patterns and dynamics that are only apparent when measured in natural environments [104, 139]. Despite making tremendous progress, contemporary neuroimaging techniques such as fMRI [82] and MEG are hindered from studying these advanced dynamics due to their poor portability and immobility during use [140, 83]. electroencephalogram (EEG), although highly portable, suffers from low spatial resolution compared to fMRI [141, 140]. These inherent disadvantages of the gold standard techniques restrict our current understanding to limited types of stimuli and interactions within confined spaces [104]. In recent years, researchers have turned to fNIRS to address this technological gap [37]. FNIRS is based on the theory of neurovascular coupling [38]. It uses low-power light spectroscopy to measure brain activation and its associated hemodynamics [37]. With its non-invasive nature, the use of fNIRS has increased exponentially [97, 83] to include studies from psychiatric conditions [91, 92] and language [89, 90, 142] to cognitive neurodevelopment [85, 86, 87, 88] and stroke recovery [93], education [143], pain detection [144], and even brain-computer interfaces [94, 95, 96].

Many of these studies using fNIRS have utilized traditional, fiber-based, cart-sized instrumentation [39, 98, 99, 145]. Despite it being an improvement over conventional fMRI and MEG modalities, fiber-based fNIRS systems also quickly reached a limit on portability and chan-

nel density due to the use of fragile fiber optic cables [146, 111] and stationary source/detector units [100, 101]. The need to expand toward broader paradigms in unrestricted environments [139] requires the use of portable and wearable systems [103, 104], and the need for wearable systems has led to the increased use of modular architectures [108, 109, 110, 120, 147, 148, 149].

Modular fNIRS systems are probes composed of repeating source/detector circuits called modules [107]. Repeating modules not only facilitate and lower fabrication costs but also allow for reconfigurability to varying sizes of regions of interest [102]. By using only the minimal number of modules needed for a specific task, modular fNIRS systems drastically improve portability [83]. Additionally, the use of varying SD separations by utilizing both intra- and inter-module (sources and detectors on different modules) pairs provide overlapping channels, improving both spatial resolution and depth specificity (a key parameter in removing systemic physiological signals) [105, 148]. Modern fNIRS systems now leverage a plethora of state-of-the-art design and analysis tools that support the use of modular architecture in natural environments. Optode layout optimizers [117, 1, 118, 116] and modular probe designers [150] ensure application-specific arrangements, motion [113, 114] and coupling [115] artifact correction algorithms allow for improvements in data quality, and faster light-propagation simulation tools [125, 126] facilitate the use and analysis of high-density fNIRS probes.

Despite its increasing adoption, the modular high-density fNIRS architecture also possesses its own set of technical challenges [151, 140] and usability concerns [152, 153]. First, the use of fNIRS in natural settings means subjects will be more mobile, leading to headgear moving and shifting relative to the scalp during use [140, 154]. Current solutions to ensure proper coupling use mechanical components that are cumbersome, require replacements, and add head-borne weight [155, 108]. Second, the ever-increasing number of optodes in a probe requires very efficient encoding strategies to maintain sufficiently high frame rates to capture the hemodynamic response function [106, 145, 156]. Finally, in order to improve accuracy using high-density tomographic analysis, we must be able to know the location of all optodes in a probe prior to and during the use of a system [157]. The most traditional approach is to use expensive hand-held 3-D digitizing systems to record the coordinates of optodes prior to the start of an experiment [151, 147]. More recent solutions leveraging photogrammetry promise to be more portable, but still require a set of external cameras that restrict mobility to areas within the camera's field of view [148, 157].

To address these needs, we have designed a lightweight and re-configurable fNIRS Modular Optical Brain Imager (**MOBI**) system well-suited for full-head long-term brain monitoring or over a particular ROI. This ultra-compact and fiberless system addresses optode-to-scalp contact

coupling through its shape and board composition. A dual-triangle shape allows for better conforming to a surface, akin to how a triangular mesh accurately represents a 3-D shape, while its flexible-circuit-based board allows the entire module to bend over arbitrary shapes to ensure constant optode-to-scalp contact [155, 121]. Additionally, a dense peer-to-peer (P2P) network allows the system to automatically determine the connection topology between modules of a probe without user input. This facilitates the implementation of a spatial multiplexing encoding strategy to increase a probe’s full frame rate. Finally, the wearable MOBI modules each contain 3-D orientation sensors that leverage the connection topology and the module’s geometry to automatically determine the location of all sources and detectors without the use of an external hand-held or photogrammetry tracking system. This automatic, independent digitization method shortens setup times, ensures high data quality, and improves accuracy and contrast through tomographic reconstructions.

In this paper, we introduce our MOBI system. In Section 5.2, we describe our entire MOBI system design, including details of individual modules as well as supporting components such as the master and trigger boards. We also highlight novel features of our system, including connection topology recognition, inertial measurement unit (IMU)-based optode positioning, and frame rate improvement through spatial multiplexing. Section 5.3 focuses on the characterization of our MOBI module and the validation of its features. We quantify conformability through the use of flexible-circuit-based modules and detail the accuracy of our internal-based optode digitization method. Additionally, we show results from two *in-vivo* experiments and compare MOBI’s performance to that of a commercial fNIRS system. Finally, Section 5.4 describes the limitations and assumptions used in our investigation and proposes work to address them in the future.

5.2 Methods

5.2.1 Module design

Our MOBI system is based on double-sided modules manufactured on flexible-circuit-based boards, allowing the modules to bend and conform to the scalp [Fig. 5.1(c)]. Each module houses two detectors (OPT101, Texas Instruments, USA) with built-in trans-impedance amplifiers. The 3 dual-wavelength sources (SMT735D/850D, Marubeni, Japan) at 735 and 850 nm are driven from a digital multiplexer (NX3L4051, NXP Semiconductors, Netherlands) with a programmable constant current driver (LT3092, Analog Devices Inc., USA) using a spatial multiplexing encoding strategy (Fig. 5.2).

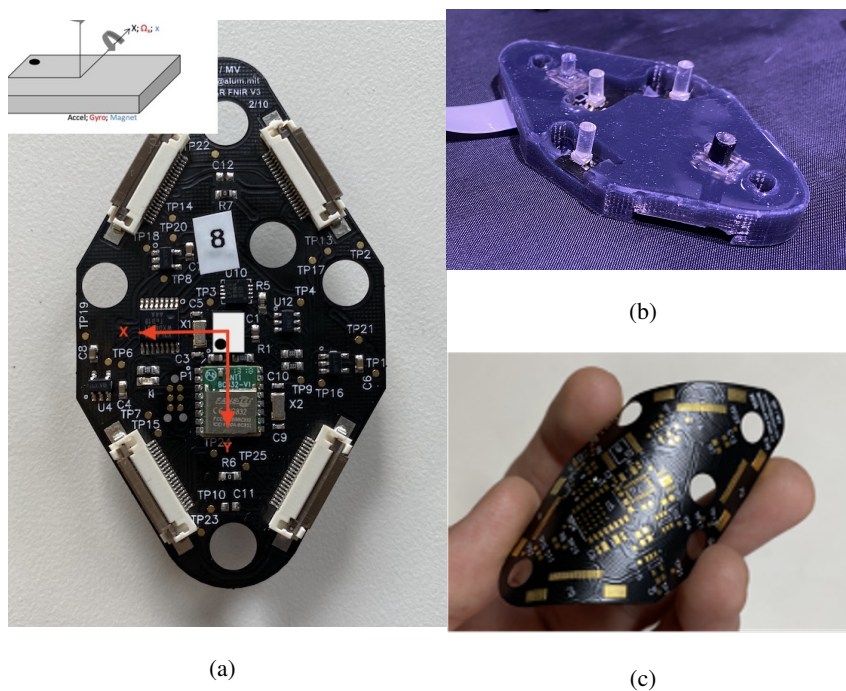


Figure 5.1: (a) Top side of a Modular Optical Brain Imager (MOBI) module without a silicone cover showing the four flexible printed circuit connectors and 5 hair removal holes. (b) Bottom side of a MOBI module with light guides on optodes and black silicone cover of board. (c) Unpopulated flexible-circuit-board for a MOBI module.

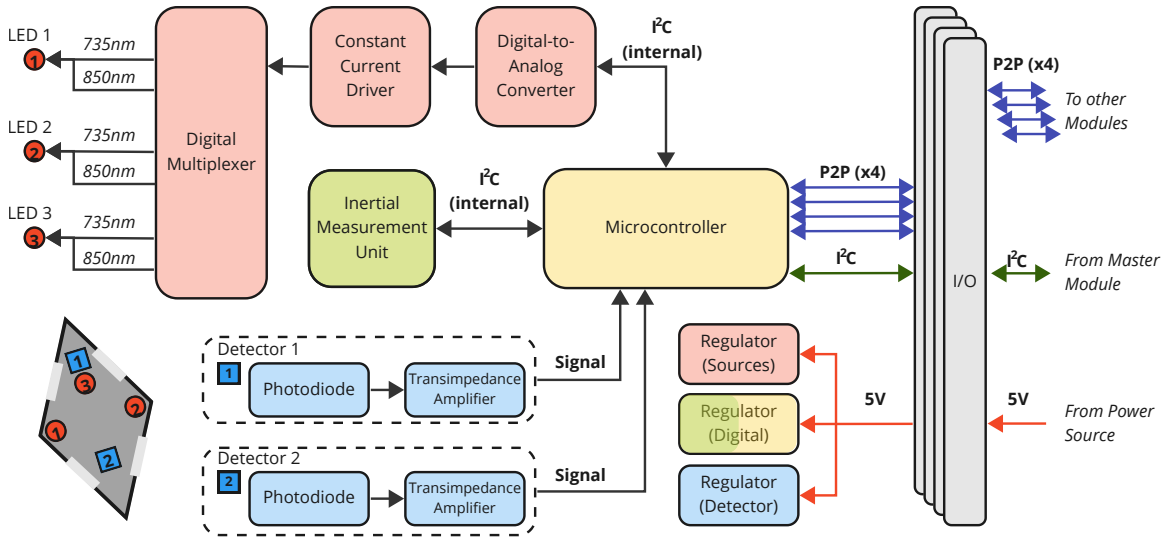


Figure 5.2: Schematic diagram of a single Modular Optical Brain Imager module. The microcontroller uses an internal Inter-Integrated Circuit protocol to communicate with components on a single board. A peer-to-peer network allows communication between neighboring modules.

The optode layout results in one 8 mm, one 30 mm, and four 24.5 mm dual-wavelength channels on a single module. A 3 mm diameter light guide (53-833, Edmund Optics, USA) is glued to each optode to focus the emitted and detected light [Fig. 5.1(b)]. A 9-axis IMU allows for absolute orientation measurements for each module (BNO055, Bosch Sensortec, Germany). All optodes and sensors on the MOBI module are controlled and read by an onboard system-on-a-chip (BC832, Fanstel Corp, USA) with an integrated microcontroller (nRF52832, Nordic Semiconductor, Norway). An internal Inter-Integrated Circuit (I²C) communication protocol is used to set the current driver and communicate with the onboard IMU (Fig. 5.2). Additionally, three low-dropout voltage regulators regulate the power source voltage for the source, detector, and auxiliary measurement components. The microcontroller samples all six dual-wavelength channels, dark measurements, and IMU measurements at a frame rate of 22 Hz.

The five optodes are located on one side of the module—the side that remains in contact with the scalp. All driving electronics are placed on the non-scalp side of the module to assist with heat dissipation and comfort. Triangles are the most efficient shape for tessellating a 3-D surface, thus, the use of a “dual-triangle” shape (two equilateral triangles with 50 mm sides) and a flexible-circuit-based board allows for increased conformity and optode-scalp coupling. MOBI modules have a channel density of 0.56 dual-wavelength channels per square centimeter. The modules are

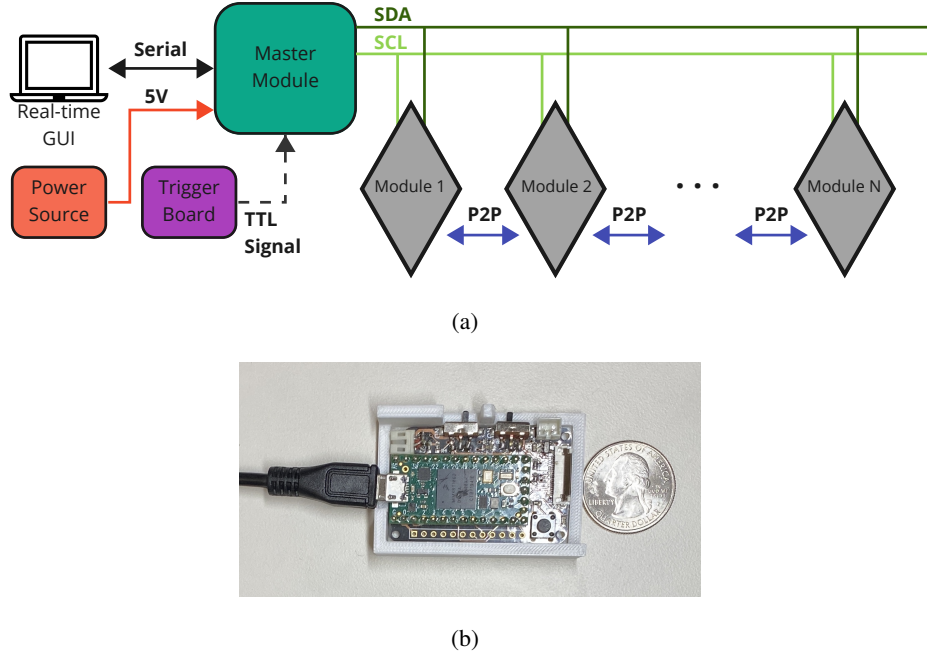


Figure 5.3: (a) Schematic diagram of a Modular Optical Brain Imager system. An external power source and trigger board are optional. (b) The master module without its cover.

completely encapsulated in flexible black silicone to provide comfort during long-term wear, block stray light, and protect the electronic components during use. Each module has four flexible printed circuit (**FPC**) connectors that allow multiple modules to be connected using **FPC** cables of fixed lengths [Fig. 5.1(a)]. A **P2P** serial network allows each module to communicate with up to four connected neighboring modules. Five 6 mm diameter holes next to each optode are used for hair removal after placement on the scalp. Each module, including the components, light guides, and silicone cover, weighs 14 grams.

5.2.2 System architecture

Our **MOBI** system consists of a computer, a single master module, and an arbitrary number of **MOBI** modules connected to each other using **FPC** cables (Fig. 5.3). Optionally, a separate power source and a trigger board can also be connected to the master module to allow synchronization of events during experiments. The master module uses an I²C communication protocol for power and data acquisition of each module (Fig. 5.3(a)). The master module incorporates a USB-based microcontroller development system (Teensy 4.0, PJRC, USA), a voltage regulator, an

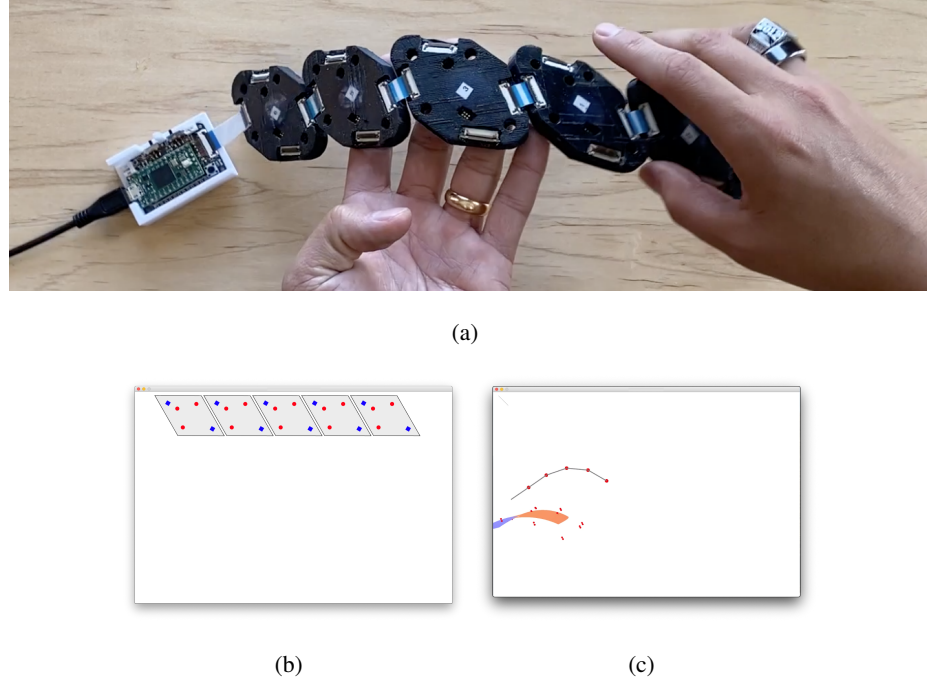


Figure 5.4: (a) Five modules in a single chain configuration connected to a master module. (b) Modular Optical Brain Imager (MOBI) Graphical User Interface (GUI) displays 5 modules connected. (c) MOBI GUI displays the relative position of each module based on differences in neighboring orientation measurements.

FPC connector, a Japan Solderless Terminal (JST) connector, and two switches. A micro-USB cable connects the master board to a computer for serial communication. The switches are used to manually select the power source (from micro-USB or an external battery). A 2-pin JST connector allows an external trigger board to be connected for synchronizing auxiliary signals such as experimental triggers. The trigger board is based on a simple microcontroller (Atmega328p, Microchip, USA) and interrupts fNIRS readings from inputted transistor-transistor logic (TTL) signals. The entire trigger board is encased inside a 3-D printer cover. A GUI provides real-time detector and IMU readings. The GUI also provides the ability to change the current source and detector gain of individual optodes. All acquired MOBI data is saved in Shared Near Infrared Spectroscopy Format (SNIRF) [158].

5.2.3 Automatic features

5.2.3.1 Connection topology recognition

Our MOBI system has the ability to recognize the connection topology between all modules to determine the number of modules and the orientation of each module in an arbitrary probe. Any two modules can be connected by simply bridging any FPC connections with an FPC cable [Fig. 5.4(a)]. Upon start-up, each module samples all four of its P2P communication channels to determine if another module is connected to one or more of its FPC connectors. This sampling of inputs/outputs allows the P2P serial network to automatically determine how each module is laid out relative to others. With the P2P connections identified, the master board can determine the orientation of each module in the probe by simply rotating and translating the module dimensions based on the connection topology [Fig. 5.4(b)].

5.2.3.2 IMU-based optode positioning

Additionally, our MOBI system can automatically determine the 3-D position of each source and detector in the probe without the use of an external digitizer. With the connection topology known, the master module can sample the orientation sensors between neighboring modules to create a 3-D spline estimating the shape onto which the probe is placed [Fig. 5.4(c)]. The master module then superimposes FPC cable lengths, module geometry, and optode layout within a module to derive the 3-D location of each optode, reducing the need for time-consuming 3-D position measurements. The IMU measurements also permit robust temporal signal rejection through real-time monitoring of optode movements during use.

5.2.3.3 Spatial multiplexing groupings

Finally, our MOBI modules utilize a spatial multiplexing encoding strategy in which sources are grouped into SMG and turned on at the same time [150]. Based on the layout of all the sources and detectors (automatically derived from the connection topology), the master module assigns sources into SMGs to be on simultaneously without cross-talk based on the SNR of the system. In this way, probe layouts that are more spread apart lead to a smaller number of SMGs because the sources are more dispersed. The spatial multiplexing improvement ratio (SMIR) is defined as the number of sources in a probe divided by the number of SMGs. In this way, spatial multiplexing improves a system's full frame rate by a factor of SMIR.

5.2.4 In-vivo protocols

The **MOBI** system was validated against a commercial fiber-based **fNIRS** system (Brite23, Artinis) through simultaneous measurements during a dual-pressure cuff occlusion experiment on the arm. A single **MOBI** module and an Artinis probe with a single channel were placed on the underside of the forearm for the cuff occlusion experiment. The upper arm rested at the same height as the heart. Data from the 30 mm channels were simultaneously captured at 10 Hz in a completely dark room. The 100 mmHg (venous) and 220 mmHg (arterial) occlusions lasted 75 seconds each.

Additionally, human brain activity was measured in an adult male in the left motor cortex area during a finger-tapping task. The finger-tapping task consisted of a 10-second task period followed by 20 seconds of rest, repeated 10 times with 60 seconds of baseline rest prior to and at the end of the repeated tasks. Subjects were instructed to sit still with their eyes closed during the entire experiment. During the task period, a verbal command instructed the subjects to tap their right thumb sequentially against their index, middle, ring, and pinky finger, followed by the same sequence mirrored, repeated as fast as possible until instructed to rest. During rest, subjects were instructed to place both hands on their laps. Signals were obtained through a single **MOBI** module placed over the left motor cortex.

Data from **MOBI** were converted to **SNIRF** format using MOCA. Data from Artinis was first converted to the **NIRS** format using the Artinis software, OxySoft, prior to converting to **SNIRF** format using Homer. Optical density was converted to hemoglobin concentrations using Homer after applying a 0.01 Hz high-pass and a 0.5 Hz low-pass filter to all channels.

5.3 Results

5.3.1 System characterization

A 20-module full-head **MOBI** probe results in 372 dual-wavelength channels due to the use of source and detector pairs in between adjacent modules. This increases the achievable channel density to 1.72 channels per square centimeter. Additionally, with **MOBI**'s spatial multiplexing encoding strategy and a **SD** separation cutoff of 52 mm (where **SNR** is > 40 dB), this full-head probe results in 14 spatial multiplexing groups and a full frame rate of 4.7 Hz. Each source is driven at 100 mA. The total power draw of the full-head probe is 2.31 W, resulting in a 2.85-hour battery life when a 3.7 V 2000 milliamp-hour (mAh) battery is used.

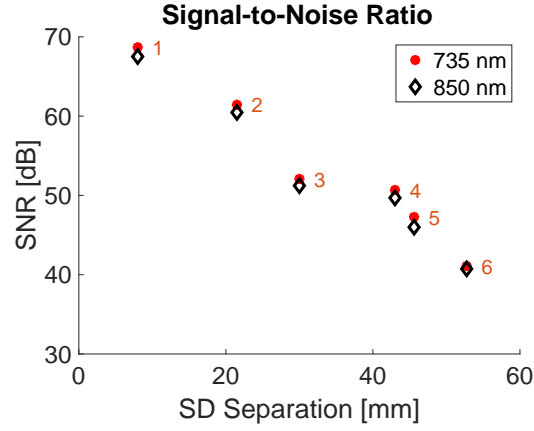


Figure 5.5: Signal-to-noise (SNR) of Modular Optical Brain Imager modules as source-detector separation increases. Red asterisks indicate SNR for the 735 nm while black diamonds are for the 850 nm wavelength. Orange numbers signify the channel number. Channels 1, 2, and 3 are from the same module. Channels 4, 5, and 6 are from sources and detectors on different modules.

Table 5.1: The full frame rate of a probe depends on the layout of the modules within a probe. The three layouts in Figure 5.6 result in the channels, groupings, and full frame rates below.

	Layout 1	Layout 2	Layout 3
Number of Modules	5	5	5
Temporal Encoding Full Frame Rate [Hz]	4.4	4.4	4.4
Number of Channels	38	53	55
Number of Spatial Multiplexing Groups	6	7	8
Improvement Ratio SMIR	2.5	2.14	1.875
Spatial Encoding Full Frame Rate [Hz]	11	9.4	8.25

Fig. 5.5 shows the SNR as a function of SD separations. The SD separations were calculated from intra- and inter-module channels using a 3-module probe placed on an optical phantom ($\mu'_s = 4.7 \text{ cm}^{-1}$ and $\mu_a = 0.063 \text{ cm}^{-1}$ at 830 nm). Each measurement is the average of 10 samples of that channel. Fig. 5.5 shows a linearly decreasing SNR as SD separation increases for both wavelengths. The correlation coefficient, R^2 , is 0.955 and 0.959 for the 735 and 850 nm wavelengths, respectively. SNR for MOBI modules is greater than 50 dB for SD separations of up to 43 mm.

5.3.2 Spatial multiplexing improvement

The performance results from three different 5-module probe layouts (Fig. 5.6) are shown in Table 5.1. When using a temporal encoding strategy, the full frame rate of the probe is determined by the number of sources in the probe since each source is sampled sequentially. Although the

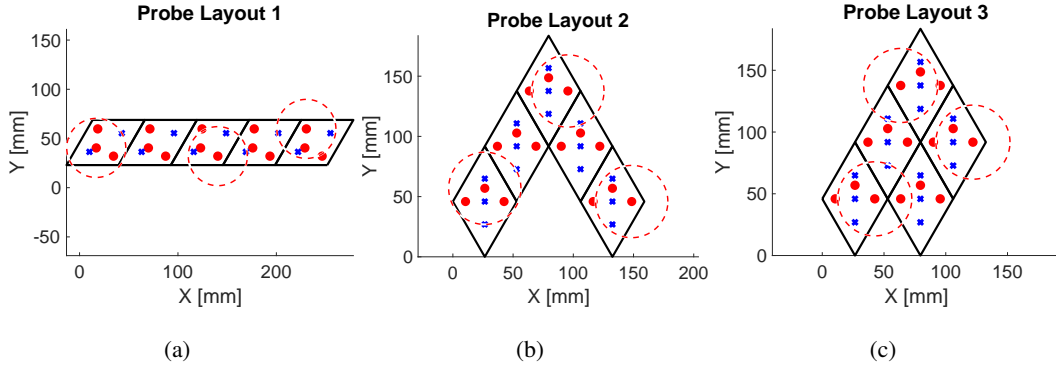


Figure 5.6: Three example probe layouts all composed from five identical Modular Optical Brain Imager modules. Optodes are represented by small red circles (sources) and blue crosses (detectors). Each layout has multiple spatial multiplexing groups determined based on the global proximity of sources to each other. Red dashed circles show which sources are simultaneously on for the first spatial multiplexing group of each layout.

temporal encoding full frame rate remains constant at 4.4 Hz, the channel density and the number of spatial multiplexing groups increase from layout 1 to 3 as the layout of the probe becomes denser (Row 3, Table 5.1). Consequently, SMIR decreases as the probe layout increases in density, limiting the potential full frame rate performance gain. Layout 1 saw the biggest improvements in full frame rate when converting from a temporal to a spatial encoding strategy. The spatial multiplexing full frame rate was always larger than the temporal encoding full frame rate for all three layouts.

5.3.3 Optode-scalp coupling

A 5-module probe, in a configuration identical to layout 2 in Fig. 5.6(b), was placed on a 100 mm radius sphere. The 25 optodes were digitized using a hand-held Polhemus digitizer and the distance to the center of the sphere was calculated for each optode in both probes (Figure 5.7). The digitization was conducted on both flexible-circuit-based and rigid-based modules [Figs. 5.7(a) and 5.7(d)].

Fig. 5.7(b) shows the average distance to the center of the sphere for all optodes of a rigid-board-based probe to be 107.5 mm with a range of 10.5 mm. In contrast, the average distance to the center decreases to 104.9 mm with flexible-circuit-based boards that allow the module to conform to the spherical surface [Fig. 5.7(e)]. Additionally, the range of distances decreases when using flexible-circuit-based modules. Fig. 5.7(c) reveals a skewed left histogram, indicating that optodes near the edges of rigid modules remain farther from the scalp. Fig. 5.7(f), however, shows that

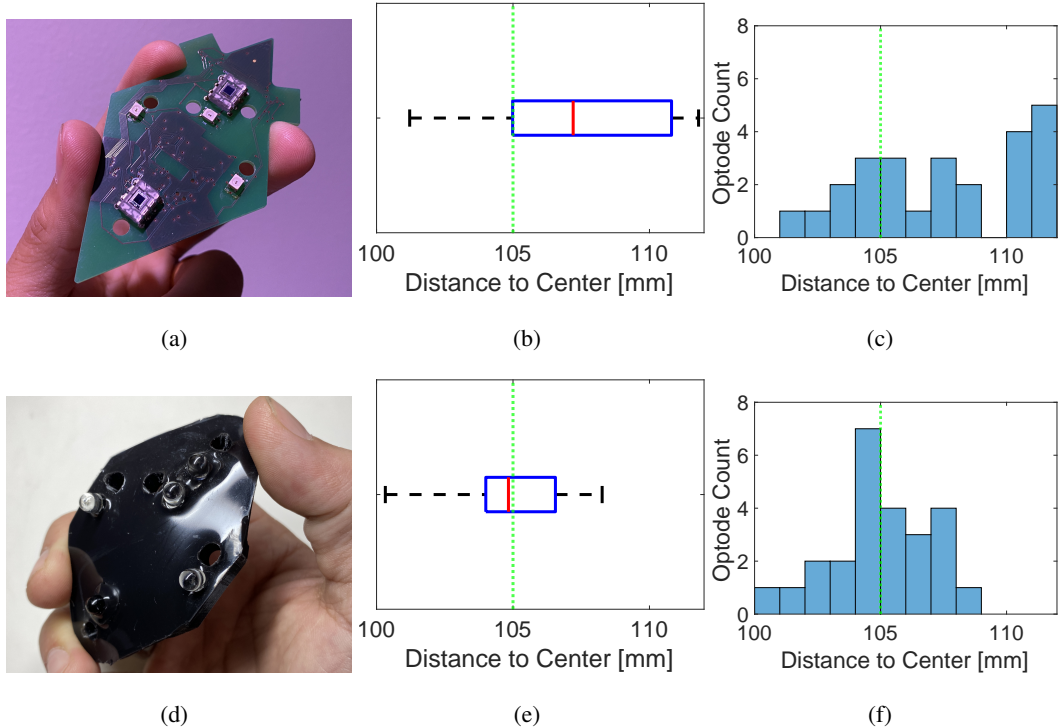


Figure 5.7: (a) A rigid-based board showing three sources and two detectors. (b) Boxplot showing the distance from optode locations to the center of the sphere using rigid modules. The red line denotes the average distance of all 25 optodes. The dashed green line represents the expected distance to the center given the 5 mm thickness of the modules. (c) A histogram of the distances reveals that the rigid-based probe does not conform to the sphere, leading to optodes being farther away from the surface, especially those optodes closer to the edge of the module. (d) A flexible-circuit-based board showing three sources and two detectors with light guides. (e) Boxplot showing the distance from the optodes to the center of the sphere of the flexible-circuit-based probe. (f) The histogram of the flexible-circuit-based probe optode distances.

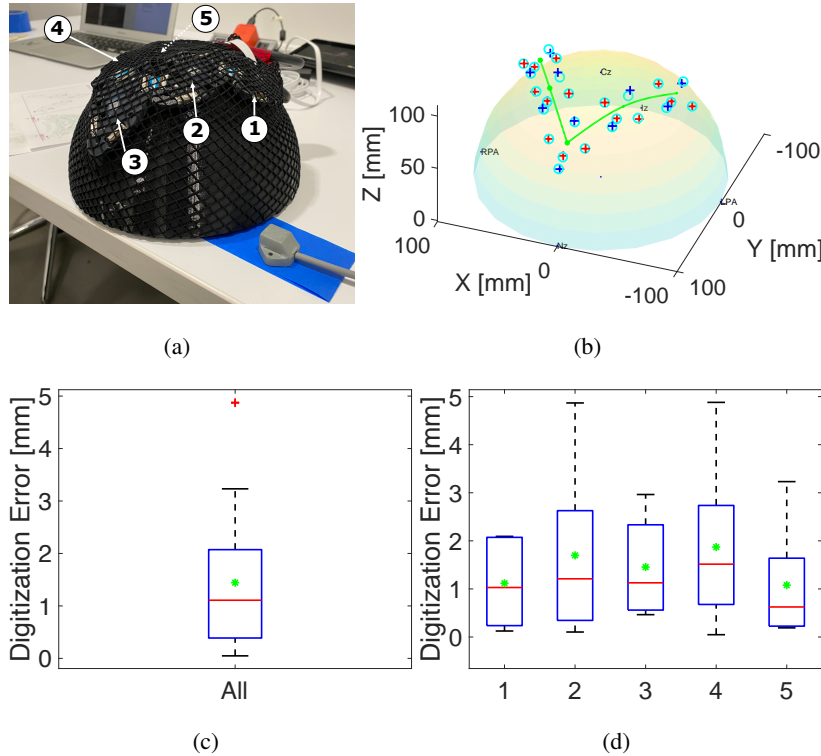


Figure 5.8: (a) Flexible-circuit-based Modular Optical Brain Imager (MOBI) modules arranged in probe layout 2 (from Figure 5.6) on top of a 100 mm radius sphere. (b) Spline model between 5 MOBI modules (green line) from which source (red crosses) and detector (blue crosses) positions are derived. Automatic optode digitization overlaid on manual digitization results (cyan circles). (c) Digitization error distribution averaged over all five modules in the probe. A green asterisk indicates the average digitization error. (d) Digitization errors are grouped by module.

by using flexible-circuit-based modules, the same optode layout within a module results in optode distance closer to the scalp, indicating the ability of flexible-circuit-based modules to conform to the surface.

5.3.4 Automatic optode positioning

Fig. 5.8(b) shows the traditional hand-held-based optode locations against the resulting optode locations using internal orientation sensors. For visibility, the optode locations are displayed over a 100 mm radius sphere. The cyan circles are optode locations averaged across five repetitions of hand-held digitizations. The standard deviation across those five hand-held digitizations was 1.78 mm. Fig. 5.8(c) shows the average digitization error over all optodes, defined as the Euclidian

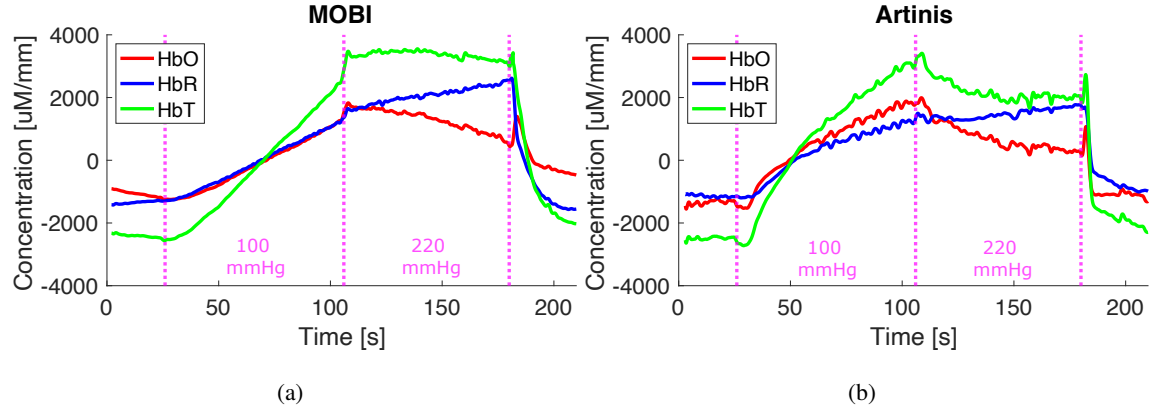


Figure 5.9: Results from a dual-pressure blood occlusion experiment using (a) a single Modular Optical Brain Imager module and (b) a single Artinis channel placed on the forearm. Venous (100 mmHg) and arterial (220 mmHg) occlusions lasted 75 seconds each prior to release. Oxygenated, deoxygenated, and total hemoglobin concentrations are shown in red, blue, and green lines, respectively.

distance between the orientation-sensor-based location and the hand-held-based location. The average orientation-based error was 1.4 mm. Fig. 5.8(d) shows the same digitization error with optodes grouped by module. For all five modules, the average digitization error was less than 2 mm.

5.3.5 Cuff occlusion results

Fig. 5.9 shows the resulting changes in hemoglobin concentrations during the dual-pressure blood cuff occlusion experiment. During venous occlusion, both **HbO** and **HbR** increase for both systems [Figs. 5.9(a) and 5.9(b)]. The arterial occlusion resulted in a negative correlation between **HbO** and **HbR**, as demonstrated by the horizontal total hemoglobin (**HbT**) line. Additionally, the **MOBI** module captured the hyperemic peak typically observed when occlusion is suddenly released.

5.3.6 Finger-tapping results

Fig. 5.10 shows the resulting hemodynamic response function (HRF) after block-averaging during a finger-tapping experiment. The stimulus lasted 10 seconds with a 20-second break in between, repeated 10 times. A clear hemodynamic response is shown with an increase in **HbO** of 60 μM approximately 10 seconds after stimulus onset. All channels demonstrated the expected increase in **HbO** and decrease in **HbR**, albeit channels over the motor cortex show a larger amplitude response.

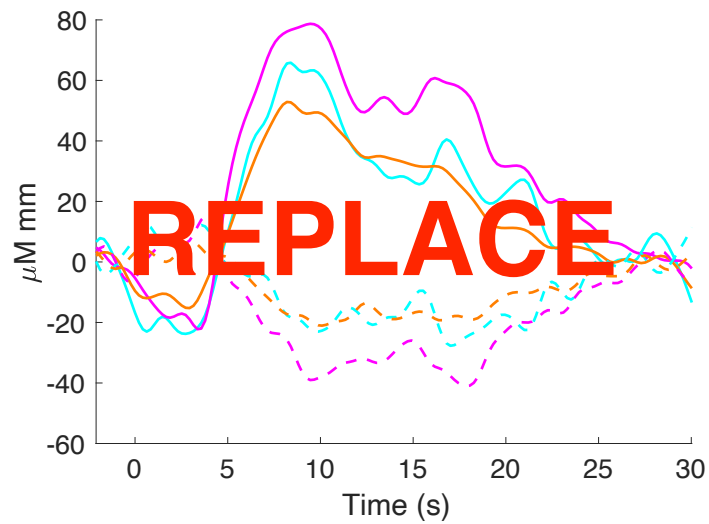


Figure 5.10: Block average results from a finger-tapping experiment with a Modular Optical Brain Imager module placed over the left motor cortex centered on C3 in the standard 10-20 system. Solid lines are oxygenated and dashed lines are deoxygenated hemoglobin. Magenta, cyan, and orange lines represent different channels within the probe.

5.4 Discussion

While many modular fNIRS systems have brought about advantages such as portability, scalability, and modularity, to our knowledge this is the first 3-D aware and fully flexible-circuit-based system. MOBI's features are especially important for transitioning fNIRS from laboratory/clinical settings to natural environments. With the expected higher physical movements in these new settings, we must find new and simpler methods to ensure optode-to-scalp coupling during use. Additionally, for true wearable commercial adoption, the fNIRS community needs to rely less on expensive and cumbersome technology, such as 3-D tracking systems, for system setup. MOBI's automatic connection topology detection and IMU-based optode positioning do just that—they provide the necessary technical quantification for highly accurate 3-D modeling without the need for lots of user input and knowledge, enabling not only a wearable system but a usable one too.

Additionally, the system's usability is improved without affecting its performance. Fig. 5.5 shows MOBI's large dynamic range, an important consideration for modular, full-head systems with multiple channels of various SD separations. A high SNR is achieved for large SD separation while keeping safety considerations in mind. For example, the holes designed into the modules used for clearing hair also provide cooling. The double-sided board design places only optodes on the scalp-facing side, limiting all driving electronics to the non-contact side, allowing for further heat dissipation for long-term wear. With a measured $9.8\text{ m}\Omega$ resistance for each module, 75 modules can be theoretically connected prior to the 5 V supply power dropping below the necessary 3.3 V to drive the microcontrollers, far above the approximate 20 modules needed for a full head probe. Excluding the master board and any fabric to further block light, a full-head 20-module probe would weigh 280 grams (about the weight of an average bicycle helmet)—lightweight enough for long-term wear.

Full-head modular probes not only require lightweight modules and large dynamic ranges but also an encoding strategy to ensure fast full frame rates. Fig. 5.6 shows how a spatial multiplexing encoding strategy can improve a full probe's sampling rate by leveraging a probe's layout rather than the total number of sources. As long as sources are spatially dispersed based on their performance, contributions to a detector's readings avoid cross-talk. As the probes become denser and the number of channels increases (Table 5.1, Row 3), the distance between sources decreases, and the number of SMGs must increase to prevent cross-talk. Similarly, as 2-D probes are placed on 3-D surfaces, the Euclidean distance between sources decreases, which may require further SMG refinement. Although spatial multiplexing can be easily implemented and doesn't require exten-

sive hardware, it does require knowledge of the location of all sources and detectors to identify the **SMGs** for a particular probe—a functionality that many systems currently do not possess without the use of external digitization tools.

In addition to increasing the full frame rate of a probe, modular **fNIRS** systems must ensure proper source-to-scalp coupling during high-movement use in natural settings. Fig. 5.7 compares a rigid board and a flexible-circuit-based board’s ability to conform to a surface. Rigid modules have minimal direct contact with the scalp and rely on mechanical/protruding couplers on the optodes or curved board designs tailored toward specific head shapes. Fig. 5.7 highlights the source-to-scalp gaps inherent in rigid-board designs. Therefore, designers of rigid boards must balance between designing smaller boards to increase source-scalp coupling or designing larger boards that allow for larger **SD** separations. Our flexible-circuit-based boards allow for both.

Finally, not only is source-to-scalp coupling important, but an **fNIRS** system must also constantly measure the position of each optode during use. Fig. 5.8 validates the accuracy of our internal **IMU**-based optode positioning system. It demonstrates that the average error between **MOBI**’s **IMU**-based optode digitization and the traditional Polhemus-based digitization is only 1.4 mm. The positioning error is less than the variability of repeated handheld-based digitization systems. This method requires knowledge of the probes connection topology, assumes fixed **FPC** cable lengths, and requires knowledge of the module geometry and optode layout. Although automatic optode digitization can drastically reduce the time it takes to set up **fNIRS** systems, it does require appropriate hardware support such as a **P2P** network and orientation sensors on each module. Although we have seen the use of orientation sensors in modular systems for motion artifact correction, to our knowledge, this is the first use of **IMUs** for internal-based optode positioning and decreasing system setup times.

Fig. 5.9 shows the results of validating our **MOBI** system against a commercial **fNIRS** system. As expected, both systems show an increase in both **HbO** and **HbR** during venous occlusion. When the pressure increases above systolic pressure, we see a negative correlation between **HbO** and **HbR** due to the muscles depleting blood oxygen during the occlusion of arterial blood. Finally, the hyperemia peak seen at 180 seconds corresponds to the increase in blood flow that occurs following arterial occlusion. Not only do both systems capture the same physiological traces, but the traces are consistent with previous research results [149]. Similarly, Fig. 5.10 shows the results of a finger-tapping experiment. As expected, the **HRF** shows an increase in **HbO** and a decrease in **HbR** during a task that utilizes the motor cortex. Although we cannot say anything about our system’s performance across a population due to it being a study of N=1, these experiments demonstrate

that **MOBI**'s ability to extract tissue hemodynamics and brain activity is comparable to existing commercial systems.

Our **MOBI** system has limitations despite directly addressing many usability concerns of wearable systems. First, spline models onto which optode layouts are superimposed rely on the assumption that the distance between modules is fixed. In **MOBI**, we use 14 mm length non-stretchable **FPC** cables that provide a 2 mm gap between modules once connected to the **FPC** connector. As **MOBI** samples neighboring **IMUs**, it fixes the spline distance between modules. Depending on the cap design, this assumption may not hold true for other **fNIRS** systems (for example, if modules are placed on stretchable fabric). Second, while connecting modules using **FPC** cables assists with determining the connection topology, it makes it difficult to remove a single module from a dense probe to adjust hair under a particular region. Rather, our **MOBI** system uses two caps—a sparse mesh cap that holds the probe in place while a user uses the holes to access and adjust hair under optodes, and a second cap placed after hair adjustment to further block stray light. Third, the finger-tapping results were conducted on a subject with short hair. Further investigations into the effect of hair artifacts on signal quality must be performed. Finally, although **MOBI** data can be saved in the standardized **SNIRF** format, our data acquisition Processing-based **GUI** requires users to learn and work in a new interface. Future work includes integrating our work with the open-source middleware Lab Streaming Layer [159] for easier synchronization and recording of **fNIRS** and auxiliary data.

CHAPTER 6

OPTICAL MAMMOGRAPHY CO-IMAGER (OMCI)

OMCI is a high-density breast multi-subsystem devide designed to be used in conjunction with existing x-ray mammography systems or as a standalone system for **DOT**. It integrates four subsystems: a mechanical breast compression stage to resemble clinical mammography, a frequency-domain subsystem for recovering absolute tissue optical properties, a wide-field transmission-based diffuse optical subsystem, and high-resolution breast surface acquisition system. Although **OMCI** is composed of four separate subsystems working in tandem, in this chapter, we will briefly provide an overall instrument description but will focus on design and characterization of the dual-camera **SLI** breast shape acquisition system used for improving diffuse optical tomography image reconstructions.

6.1 Introduction

Breast cancer is the most commonly diagnosed cancer in women worldwide with an estimated 1,918,030 new cases in 2022 in the United States alone [160]. Screening and diagnostics of breast cancer is done through structural or functional breast imaging using multiple breast imaging modalities. X-ray mammography and digital breast tomosynthesis (**DBT**) are the primary breast cancer screening techniques [161] used for early detection to reduce mortality rates [162]. Modalities such as magnetic resonance imaging (**MRI**) and positron emission tomography (**PET**) are used less frequently than x-ray due to their high cost and use of radioactive isotopes [161]. Despite its recommendation for screening, not only does x-ray mammography expose patients to ionizing ra-

diation but it also suffers from a high false-positive diagnostic rate [162, 163]. The modality lacks both strong structural contrast between healthy and tumor tissue, and the ability to quantify tissue functions to assess benign versus malignancy [164]. These limitations have led researchers to investigate using **DOT**) techniques to characterize the breast tumor’s physiology to lower false-positive diagnoses.

Unlike x-ray mammography, **DOT** is an imaging modality that uses non-ionizing **NIR** radiation to yield three-dimensional (3-D) maps of the optical properties of illuminated tissue [44, 165, 166, 167]. Biological tissues’ primary absorbers in the spectral window from around 600 to 1000 nm have relatively low absorption, allowing **NIR** light to penetrate through centimeters of tissues [168]. This allows the quantification of physiological properties such as hemoglobin concentration, blood volume, and blood oxygen saturation [164, 44]. Malignant tumors generally demand a greater blood supply than their surrounding tissues, leading to increased light absorption that can be delineated using spectroscopy and imaging methods, making **DOT** particularly useful for breast cancer imaging diagnosis [169, 170, 171, 172, 173]. Unfortunately, **DOT** images are known for low spatial resolution largely caused by the high scattering properties of biological tissues [44].

The low spatial resolution of **DOT** [174] can be improved by a multi-modal approach with x-ray mammography [175, 53, 176, 124]. The high scattering present in the breast tissue redirects photons to traverse large overlapping probing volumes before their detection, greatly reducing the locality of the measurements and resulting in blurry images. Mathematically, this is reflected as the severe ill-posedness of the inverse problem. Parallel-plate compression of breast tissues has been used in an x-ray mammography scan to minimize overlapping tissues and has also been explored for a number of standalone [172, 177] and multi-modal **DOT** breast imaging systems [178, 124, 179]. Multi-modal imaging approaches have been developed by leveraging tissue structural priors obtained from high-resolution imaging methods such as magnetic resonance imaging [180, 181] and ultrasound [51]. These approach leverage the advantages of multiple modalities—they leverage high quality structural images to constrain the **DOT** inverse problem for more accurate tissue physiology reconstructions.

Additionally, the **DOT** reconstruction can also be improved by constraining the inverse problem through more accurate surface representations of the breast. Obtaining breast surface information to aid quantitative analysis of imaging data has garnered interest from a number of applications, including **DBT** [182] and **MRI** scans [183, 184]. For multi-modal **DOT** systems, the 3-D shape of the breast can be estimated using the structural imaging modality such as **DBT** [52] or **MRI** [185]. When a 3-D imaging modality is not available, two-dimensional (2-D) mammogra-

phy [176] has also been used to provide the shape information. In such case, a simple way to recover a 3-D breast surface is to extrude the 2-D breast contour along the compression axis [186, 187], or sweep the 2-D breast contour along the contour line extracted from an orthogonal view [188]. These methods either rely on assumptions about the 3-D location of certain features (e.g. mamilla position) or assume a constant curvature of the breast along the sweeping direction. For more accurate reconstructions of tissue optical properties, especially near the surface, measuring 3-D breast surface accurately can be greatly beneficial.

Accurately acquiring breast 3-D surface shapes has gained clinical acceptance due in large part to the plastic and reconstructive surgery communities [189, 190]. The two prominent techniques for 3-D breast surface imaging are stereophotogrammetry and laser scanning [55]. Stereophotogrammetry works by overlaying multiple images of an object taken from different view angles and triangulating the location of the object based on matching features in the multiple images [191, 192, 193]. In addition to requiring multiple cameras to increase accuracy [194], this technique is also heavily influenced by lighting conditions since features need to be extracted from multiple viewpoints [195]. Another limitation is the “ptosis error” seen during scanning of ptotic or larger breasts [196]. This arises due to the small field of view of stereophotogrammetry systems, leading to inaccuracies in breast surface and volume estimations due to the portions of the breast that are not illuminated. Laser scanning is a surface imaging technique in which rays from a laser beam are reflected off an object and detected by a detector [197]. Although laser-based acquisition systems can produce more accurate surfaces [198], these systems tend to be expensive [199, 200] and require the need for very precise setups [201]. Recently, the use of patterned-lasers and orientation-sensitive detectors has led to an increase in portable 3-D laser scanning devices [202]. While low-cost laser-based depth sensors have been widely deployed in game consoles such as Xbox or PlayStation, they are only designed to achieve relatively low spatial accuracy compared to dedicated 3-D scanners. Still, patterned-laser-based surface acquisition systems generally require a minimum scanner-to-target distance of 35 cm [203, 204]. Additionally, their typical housing is too large to fit between mammography compression plates [204, 183]. Bulky instrumentation and long minimum working distance requirements make stereophotogrammetry and laser scanning techniques infeasible in the confined, low-light mammography setting.

Another widely used 3-D surface acquisition technique is **SLI** [205, 206]. SLI works by illuminating an object with two-dimensional spatially varying patterns with a projector and capturing images from the illuminated object using cameras [56]. The distortion of the specially designed patterns provides information regarding the shape of the object. Calibration of the camera-projector

system is easily done by capturing images of a known planar pattern (e.g. a checkerboard). With the ability to use off-the-shelf components, a simple setup with a single projector and camera, and a robust and simple calibration method, **SLI** is positioned to provide accurate, fast, and cost-effective breast surface scanning [205]. However, similar to most patterned-laser surface scanners, commercially available **SLI** systems have long minimal working distance requirements and large assemblies that cannot readily fit within the confined mammography compression plates [206, 182].

Our approach to lowering false-positive diagnoses is two-fold. We first aim to improve **DOT** reconstruction through more accurate surface representations of the compressed breast. Second, we aim to develop a standalone **DOT** breast imaging system that leverages structural information through the registration of the **DOT** reconstruction with prior x-ray mammographies. Our group has primarily focused on the latter through the development of both multi-modal **DOT** reconstruction algorithms [53] and multi-modal (**DOT** and **DBT**) instrumentation that can work independently [207, 208, 209] or in conjunction with existing mammography systems [126, 175]. The approach to build **DOT** systems that can work independently and integrate with existing mammography systems is commercially intriguing, since it can lower acquisition costs and maximize previous investments made into clinical instrumentation. We will take this same approach in our first aim—that is, the **SLI** surface acquisition system we build will also have the capability to function independently or be easily integrated into existing mammography systems.

In this chapter, we first describe the overall **OMCI** instrument and its subsystems. We then describe the design of the **SLI** breast scanner and detail the methods for adaptive illumination for subject-specific skin tones as well as approaches to reduce specular reflection from the compression plates. Next, we compare several traditional surface acquisition methods that leverage mammography images against our **SLI**-based breast surface acquisition system and quantify the impact of improved breast surface acquisition on the recovery of breast lesions using a series of simulations. Finally, we demonstrate **OMCI**'s use on healthy volunteers.

6.2 Methods

6.2.1 OMCI Instrument

OMCI is composed of a linear stage mounted on a vertical rotary stage. The breast is compressed by a pair of acrylic plates, with one plate mounted at the stationary end of a linear stage (MN10-0160-M02-31 BiSlide, Velmex, NY, USA). Under the bottom compression plate is a box

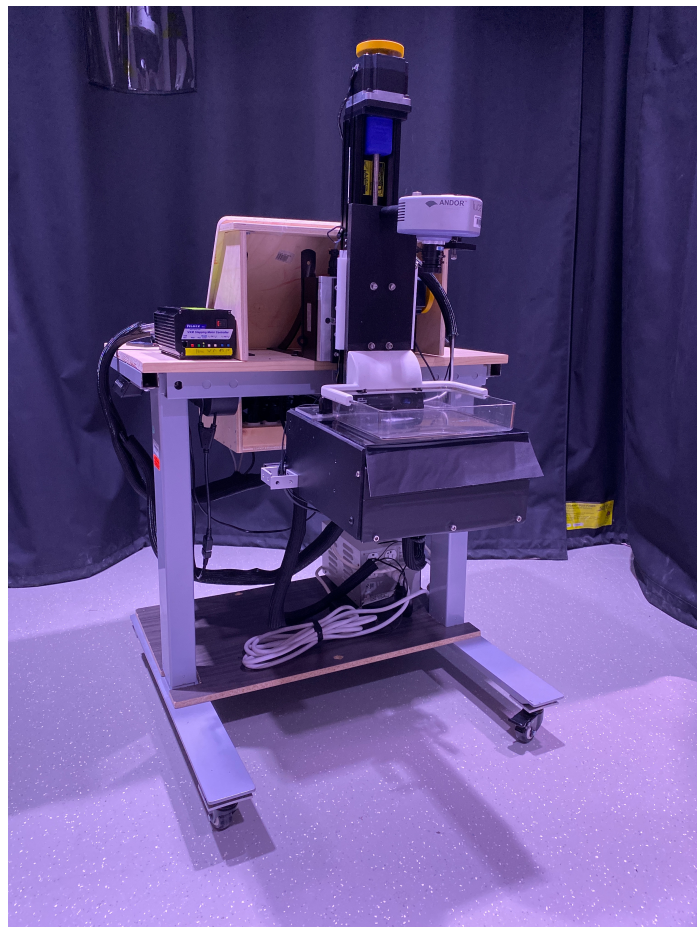


Figure 6.1: The patient side of our OMCI system in its fully compressed state.

that encloses many of the optical components of OMCI. An acrylic mammography compression plate is mounted on the moving gantry of the linear stage, allowing for a plate separation ranging from 300 mm (fully released) to 0 mm (fully closed). A linear encoder (ETI Systems, Carlsbad, CA, USA) is connected between the pair of compression plates to measure their separation. The entire breast compression assembly is mounted on a rotatory table (306045-1-s-M04-C376, Lintech, Monrovia, CA, USA), controlled by a foot pedal to permit mammography-like lateral-oblique compression. A motor driver interface (VXM-2, Velmex Inc., USA) allows both stages to be actuated independently by their stepper motor (NEMA 34 PK296 Stepper Motor, Oriental Motor Corporation, MA, USA). Two limit switches (BiSlide Push Button, Velmex Inc., NY, USA) confine the translation stage range. A reed switch (L06 Non-Contact Reed Switch, LinTech Motors, CA, USA) is used for homing the rotary stage. Four load sensors (SEN-10245, SparkFun, CO, USA) hold up the bottom compression plate and measure the pressure applied on the breast. This design specifically enables registration of structural information from separately acquired mammography scans with the DOT images using the methods detailed in our previous studies [53].

While the breast is in compression, it is illuminated with an frequency-domain (FD) and a wide-field (WF) subsystem. Bulk tissue properties are determined using a FD subsystem [210] that utilizes two laser modules (HL6750MG and HL8338MG, Thorlabs GmbH, Germany) coupled to bifurcated fiber bundle (BFY400LS02, Thorlabs GmbH, Germany). The frequency multiplexed light is driven into the OMCI box where a dual-axis galvo motor (GVS002, Thorlabs GmbH, Germany) redirects it onto different positions on the bottom of the compressed breast. A fixed detector on the top compression plate directs the light to a frequency-domain detector (C5331-04, Hamamatsu, Japan) for collection. The WF subsystem illuminates the breast from below using a continuous-wave (CW) projector (P300 Neo, Aaxa Technologies, USA) while a EMCCD camera (Andor Luca R, Oxford Instruments, U.K) located above the compression plate samples the dual-wavelength light transmitted through the breast. Both the FD and WF subsystems are controlled through the OMCI GUI written in MATLAB.

6.2.2 Dual-camera SLI breast surface scanning system

The SLI system is embedded between the compression plate to provide accurate measurement of the breast surface [Fig. 6.2(c)]. This low-profile SLI scanner has a dimension of $30 \times 10 \times 4.8$ cm³ and is attached to the stationary compression plate, on the side facing the patient's breast [Fig. 6.3(a)]. It consists of a central projector (P2-B DLP Pico Projector, AAXA

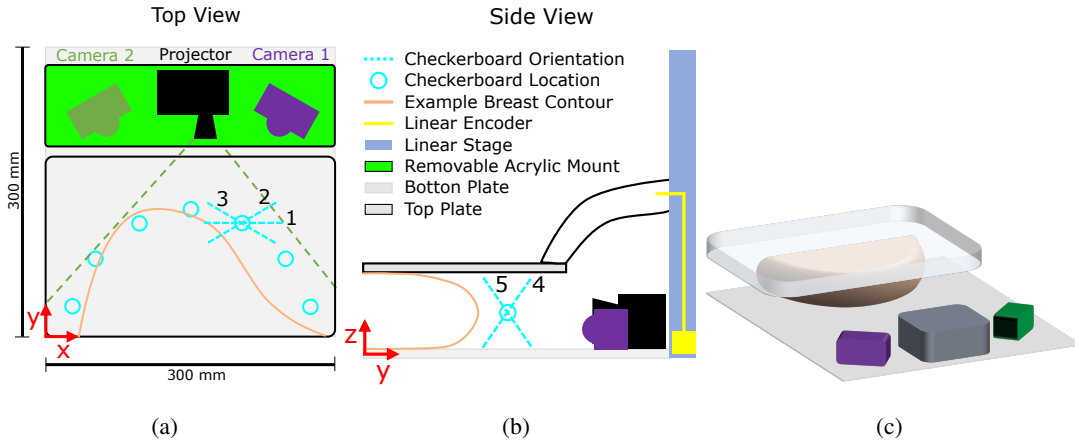


Figure 6.2: (a) Top-view of the breast compression compartment – upper: structured-light imaging system; bottom: horizontal cross-section (orange line) of the compressed breast with blue circles indicating the placement of the checkerboard used for system calibration. Numbers 1-5 indicate the 5 board orientations repeated at each location for calibration. (b) Side-view of the breast compression plates, showing the linear translation stage (blue bar on the right) and a linear encoder (in yellow), and (c) 3-D rendering of the structured-light imaging system, an acrylic bottom plate, and an acrylic compression plate (top).

Technologies, Irvine, CA, USA) and two USB cameras (C525, Logitech, Lausanne, Switzerland) to reconstruct a 3-D surface of the compressed breast. The SLI scanner is designed to have a relatively short scanner-to-target distance, typically less than 15 cm, and a vertical profile of less than 3 cm to permit scanning breasts with a wide range of sizes. A laptop is used to control the data acquisition, including illumination pattern generation, projection, camera image acquisition, and translation stage control via an interface written in MATLAB (R2017b, Mathworks, Natick, MA, USA).

Gray-code-based binary patterns [211] are sequentially illuminated onto the breast surface and captured using both USB cameras. These patterns are characterized by their pattern order, P . A pattern set of $P = 3$ results in 3 sequences which are a reflected binary of the previous (“01”, “0110”, and “01100110”). Four bar patterns are created for each sequence (a horizontal black and white bar pattern, a vertical black and white bar pattern, and the complimentary pattern of each) [212]. The digits correspond to the white (“1”) and black (“0”) bars. In addition, a full-bright (white) and full-dark (black) pattern are added to each pattern set. Thus, a pattern set of $P = 3$ results in $4 \times P + 2$ illumination bar patterns. Complimentary Gray-code-based illumination pattern sets are used due to their robustness to decoding errors [213]. The two USB cameras have

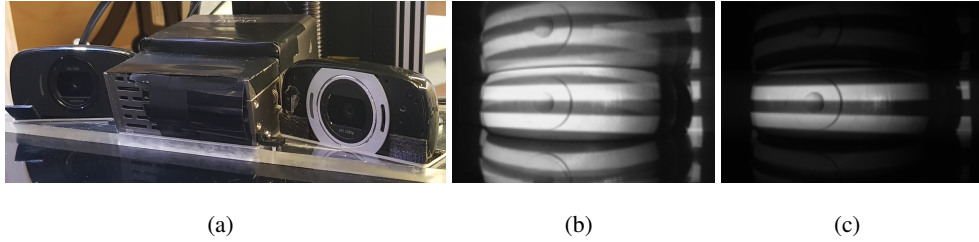


Figure 6.3: (a) Front-view photo of the structured-light imaging system. Cameras and projectors are embedded in an acrylic mount to prevent the need for re-calibration. (b) Horizontal bar patterns reflecting off the top compression plate and onto the breast show curved illumination bar artifacts when the scaling factor α is set to 1. In (c), we show the same illumination pattern with thickness-informed masking eliminating the curved bar artifacts by cropping the patterns exceeding the breast surface before projection. Additionally, the scaling factor is automatically calculated to prevent camera saturation.

overlapping field-of-views and sequentially capture images of the breast during each illumination pattern at an exposure time of 250 ms. Dual-camera simultaneous acquisition allows the **SLI** system to capture the curved surface of breasts of varied sizes without moving components.

6.2.2.1 Special data acquisition considerations

Skin tone differences are known to affect light-based surface reconstruction accuracy, especially in low-light settings. To account for skin tone variations, the normalized illumination patterns are multiplied by a scaling factor α ranging from 0 to 1 to prevent camera saturation. The scaling factor for a camera is calculated prior to data acquisition by first illuminating a full-bright pattern with $\alpha = 1$ onto the breast and capturing a single image using the camera. If the maximum pixel value of the captured image is above a preset threshold, α is decreased and the breast is re-illuminated with a full-bright pattern multiplied by the new α value. This procedure is repeated until the maximum pixel value of the captured image is less than 95% of the camera's maximum allowable pixel value. This entire procedure takes an estimated 8 seconds to complete and is repeated for each camera.

Additionally, specular reflections from the acrylic compression plates, shown in Fig. 6.3(b), can produce vertically mirrored breast surfaces. To minimize such specular reflection, we use dynamic pattern masking based on real-time separation readings provided by a linear encoder. By limiting the vertical span of the illumination patterns, the patterns are projected onto the compressed breast surface without generating strong direct specular reflections from the top and bottom com-

pression plates, as shown in Fig. 6.3(c).

6.2.2.2 SLI system calibration and re-projection errors

A standard **SLI** camera-projector calibration is performed prior to image acquisition and is described in detail in [213]. For each camera-projector pair, a checkerboard pattern is fully illuminated in multiple positions and the corner locations are estimated in the projector's default coordinate system using a robust pixel classification algorithm [214]. The camera and projector's intrinsic parameters (optical center and focal lengths) are estimated using a calibration method described in [215] by fixing a world coordinate system to the calibration checkerboard plane.

The projector's extrinsic parameters (rotation and translation from camera to projector) are calculated using a simple stereo camera calibration [216] that treats the projector as a secondary camera. This results in a rotation matrix and a translation vector relating the camera's coordinates to the projector's coordinates. Once the 3-D coordinates of all the corners of the checkerboard are computed using the camera's (and projector's) intrinsic and extrinsic parameters, the corners are "reprojected" onto all the images for which they appear. The re-projection error is defined as the average distance between the re-projected corner locations and the actual corner location.

6.2.2.3 SLI system acquisition

The same acquisition procedures are used for both calibrating the system and acquiring breast shape measurements (Fig. 6.4). A single acquisition refers to the image capture of all illumination patterns by both cameras. Camera-projector calibration requires an acquisition at each checkerboard position. During breast measurements, the acquisition is preceded by the determination of the saturation scaling factor α and masking of the patterns. Patterns during calibration are not masked since the calibration is done with the system fully uncompressed.

6.2.3 Alternative breast surface reconstruction methods for assessing SLI surface accuracy

To evaluate the accuracy of the **SLI** system, we compare its output against alternative surface acquisition methods. Each method estimates the surface of a 3-D breast derived from a **DBT** scan.

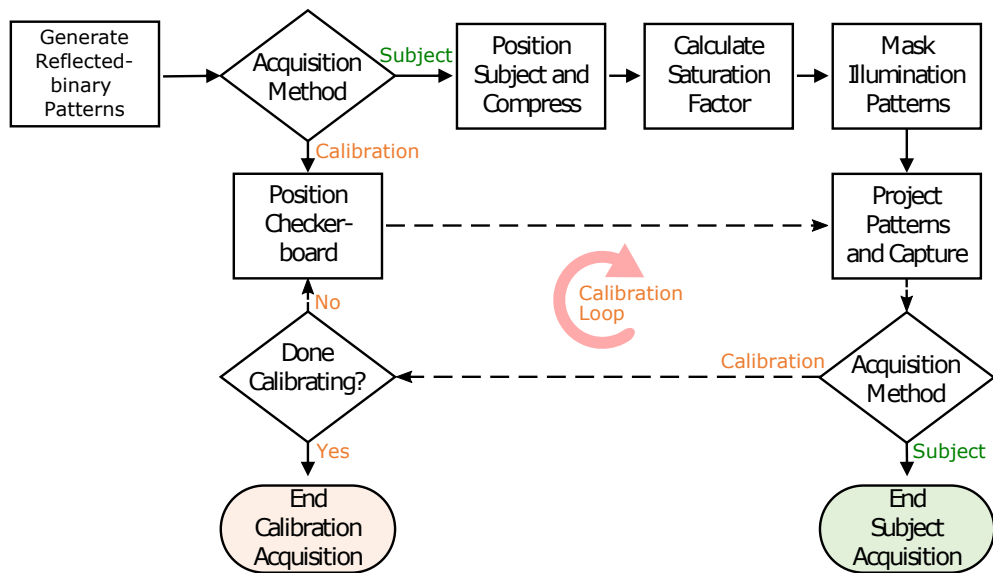


Figure 6.4: Flow chart of image acquisition for both subject measurements and system calibration. Subject measurements calculate a saturation scaling factor and mask the illumination patterns prior to projecting patterns. System calibration measurements do not mask the illumination patterns and project at full intensity. The calibration loop (dashed lines) is repeated for each location and orientation of the calibration checkerboard.

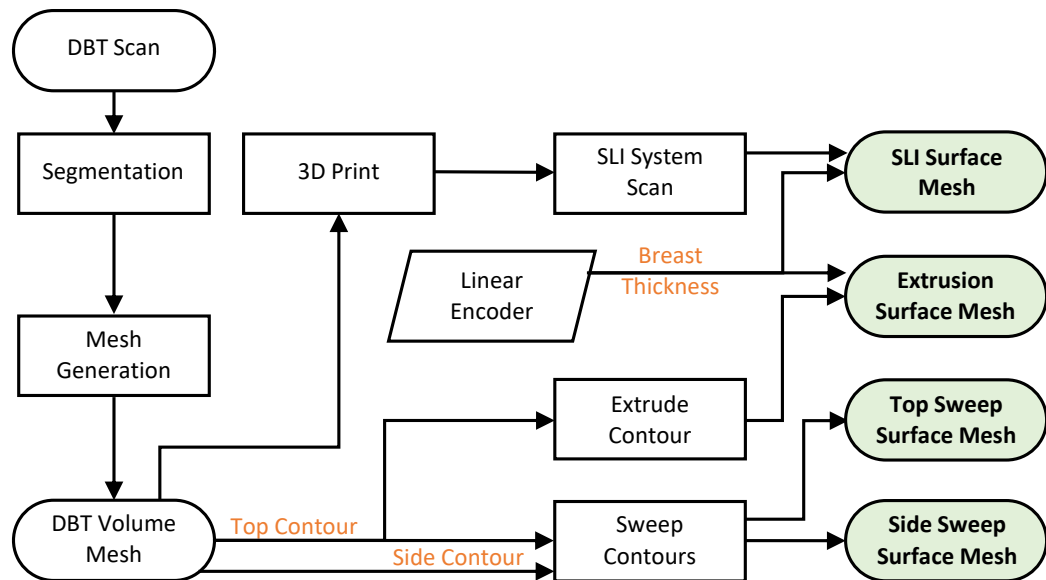


Figure 6.5: Generation of breast surface meshes using multiple acquisition methods. The digital breast tomosynthesis (DBT) volumetric mesh is created from segmented scans. The extrusion surface mesh is created by extruding the top contour to the breast thickness. The top and side contours of the DBT mesh are swept to create top and side surface meshes. The structured-light imaging mesh is created by scanning a 3-D printed breast phantom and trimming the resulting point-cloud using the linear encoder measurements. The surface estimation error is calculated for each of the surface meshes by comparing the surface estimations to the DBT mesh. All surface meshes are converted to volumetric meshes for validating the effect of surface estimation methods on inclusion reconstruction.

6.2.3.1 Reference breast phantom fabrication

Fig. 6.5 shows the process of creating surface meshes from **DBT** scans. Scans were obtained from radiology data from The Cancer Genome Atlas (**TCGA**) breast Invasive Carcinoma collection [217], available freely through The Cancer Imaging Archive [3]. The scan (ID: TCGA-AO-A03M) was chosen due to its large size and complex surface structure, allowing us to highlight the limitations of low field-of-view acquisition methods as well as traditional shape estimation methods that simply sweep a single breast contour. Digital Imaging and Communications in Medicine (**DICOM**) slices were segmented into breast and non-breast regions using ITK-SNAP [218]. Segmented slices were converted to a volumetric image and then into a 3-D mesh using a MATLAB toolbox Iso2Mesh [126] [Fig. 6.6(a)].

6.2.3.2 Single and double contour sweep-based surfaces

Three alternative surface estimation methods are employed in addition to the **SLI** surface acquisition method. These three methods use spline models of the **DBT** breast contours from two different planes (Fig. 6.2). The extrusion method creates a surface mesh by extruding the x/y breast contour in the z direction to the thickness of the **DBT** breast measured by the linear encoder [Fig. 6.6(b)]. The second and third methods utilize a curve-based sweep, in which a profile (shape) follows a path (contour) to create a 3-D model. In the “top-sweep” method, the x/y breast contour profile is swept along the y/z breast contour path [Fig. 6.6(c)]. Similarly, the “side-sweep” method uses the y/z breast contour as the profile and the x/y breast contour as the path [Fig. 6.6(d)]. In both sweep methods, the profile normal is kept constant.

6.2.3.3 Structured-light imaging surface mesh generation

The **SLI** system estimates the surface of the compressed breast from the captured images while the breast is illuminated with Gray-code sequence patterns. Each camera-projector pair’s extrinsic parameters are used to generate a point-cloud in each camera’s reference frame using Scan3d-Capture [57] [Fig. 6.6(e)]. The alignment of each camera-projector pair point-cloud is done by a rigid transformation of each point-cloud to the projector’s coordinates. The point-clouds are then down-sampled using a box grid filter and merged to a single point with normal properties averaged [219]. Denoising is then performed to remove outliers [220]. The point-cloud is trimmed in the z direction to the height of the **DBT** breast measured by the linear encoder [Fig. 6.6(f)]. The

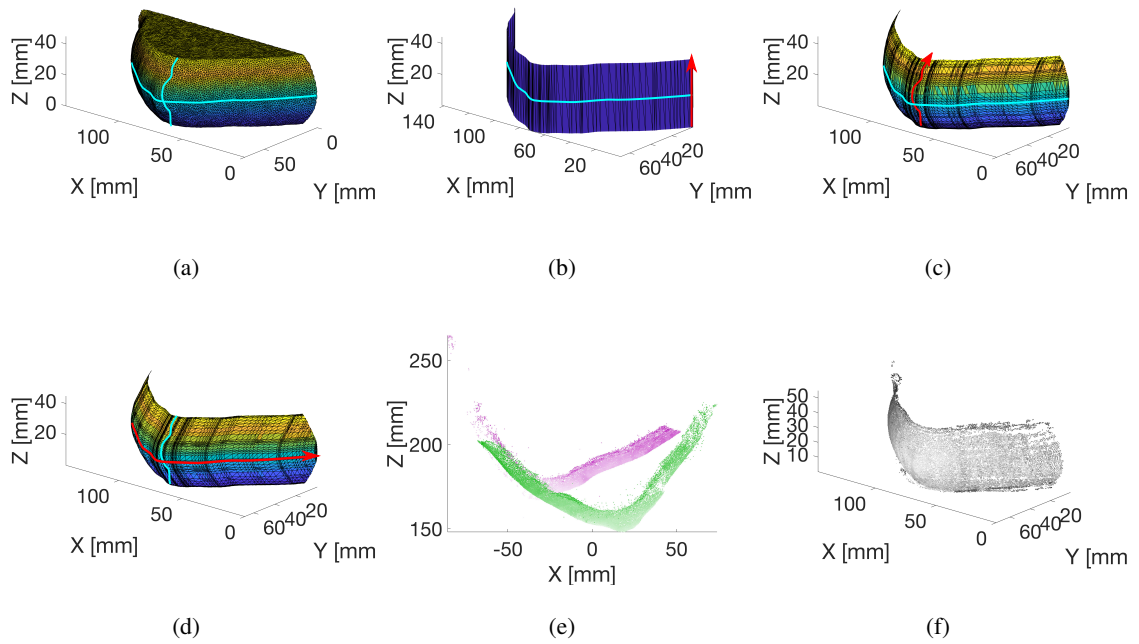


Figure 6.6: (a) Surface mesh of a digital breast tomosynthesis (DBT) model obtained from The Cancer Imaging Archive [3]. Blue cyan lines show the x/y and y/z breast contours from the top and side views. (b) Estimate of the DBT surface using the extrusion method in which the contour (cyan) is extruded to the thickness of the breast along the z axis. (c) The top-sweep method uses the x/y contour as the profile (cyan) and the y/z contour as the path to sweep (red). (d) The side-sweep method uses the y/z contour as the profile (cyan) and the x/y contour as the path to sweep (red). (e) point-clouds from both camera-projector pairs were generated by scanning a 3-D printed model of the DBT breast using the structured-light imaging system. The green (Camera 1) and magenta (Camera 2) point-clouds are in the respective camera coordinates. (f) Merged and denoised point-cloud in the projector's coordinates.

trimmed point-cloud is first converted to a mesh using a crust algorithm [221] prior to being cropped by a bounding-box mesh with height matching the breast thickness to form a closed surface mesh.

6.2.3.4 Surface estimation error

The surface estimation error, E_s , of each surface estimation method is computed by comparing the nodes in each surface mesh to the nodes in the **DBT** mesh. The residual for each node in the surface mesh is the shortest distance from that node to the **DBT** mesh. The **SLI** output mesh is linearly translated (rotation and translation only) into the projector's frame using the projector's extrinsic parameters prior to determining residuals. E_s is defined as the average residual of all nodes for a particular surface estimation method.

6.2.4 Evaluation of the impact of surface errors on DOT image reconstructions

Simulations were conducted to evaluate the impact of surface estimation accuracy on **DOT** reconstruction accuracy for inclusions of various depths. Breast surface meshes were converted to volumetric meshes with optical inclusions and the mean squared error of wide-field **DOT** reconstructions was calculated for each estimation method.

6.2.4.1 Assessment of reconstruction accuracy

The effect of different surface estimations on lesion reconstruction was quantified using simulations of **CW** pattern-illumination sources. A 5 mm radius spherical inclusion was added at the mid-plane of each volumetric mesh at distances of 5 to 45 mm away from the nipple. The x and z coordinates of the inclusion were fixed at 68 and 22 mm, respectively. The forward simulation was conducted on a ground truth volumetric mesh consisting of the **DBT** volumetric mesh and a spherical inclusion. The non-linear image reconstruction of tissue properties was calculated using an iterative Gauss-Newton method in which a series of corrective terms were added to an initial guess. The reconstruction resulted in distributions, μ_{ai} , representing the resulting 3-D absorption coefficient (μ_a) maps at the i^{th} node for each simulated tumor location and surface model.

6.2.4.2 Reconstruction error assessment

We use mean squared error (**MSE**) to determine the accuracy of the image reconstruction resulting from each breast mesh. To compute the **MSE**, we first interpolate the reconstructed absorption map, μ_a , to the **DBT** mesh, and then subtract the interpolated μ_a at each node i , with the

corresponding ground truth absorption value defined on the same node, expressed as

$$\text{MSE} = \frac{1}{N} \sum_{i=1}^N (\mu_{ai} - \mu_{a0i})^2, \quad (6.1)$$

where N is the total node number; μ_{ai} and μ_{a0i} define the recovered and ground truth μ_a values, respectively, at the i^{th} node in the **DBT** mesh.

6.3 Results

Results from the characterization of the **SLI** subsystem are broken down into three parts. We will first report the projector and camera re-projection errors of our **SLI** calibration using the calibration checkerboard. We then quantify the error of surface estimation methods in estimating the surface shape of the **DBT** breast. Finally, we show the effect of different surface estimation methods on optical property reconstruction using simulations of continuous wave pattern-illumination sources.

6.3.1 Camera-projector calibration and surface acquisition

Our dual-camera **SLI** system was calibrated in a dark room using a checkerboard with 5×7 internal corners with $1 \times 1 \text{ cm}^2$ black and white squares. The calibration checkerboard was printed and adhered to a black Delrin surface to ensure it remained planar. To account for varying breast shapes and curvatures, the checkerboard was placed at 7 locations. At each location, camera images were captured for 5 board orientations: 1) normal to the y -axis [see Fig. 6.2(a)], 2) rotated left and 3) rotated right by 30 degrees relative to the x -axis, and 4) tilted forward and 5) tilted backward by 30 degrees in the y/z plane [Fig. 6.2(b)]. This results in a total of $7 \times 5 = 35$ checkerboard positions within the camera and projector field-of-views (Fig. 6.2). Each rotation and tilt was measured manually using a printed protractor. The projector's resolution is 1280×720 pixels and the resolution of the cameras is 1600×896 pixels. Using a Gray-code of bit-length $P = 9$, we acquire $P \times 4 + 2 = 38$ images (see Section 6.2.2) at each board orientation/position placement. An exposure time of 0.25 seconds per image per camera results in a total one-time calibration time of $38 \times 7 \times 5 \times 2 \times 0.25 = 665$ seconds. The first camera-projector pair (Camera 1 with projector) resulted in a camera and projector re-projection error of 0.4089 and 0.2282 pixels, respectively. The second camera-projector pair resulted in a camera re-projection error of 0.4368 pixels and a projector re-projection error of 0.2889 pixels.

Table 6.1: Mean and standard deviation of the residuals of each point in a surface estimation mesh compared to the original digital breast tomosynthesis breast mesh.

	Extrusion	Top-Sweep	Side-Sweep	SLI
Surface estimation error, E_s [mm]	6.8353	0.3772	0.4726	0.2543
Standard deviation [mm]	2.8671	0.3029	0.3370	0.2723

A re-calibration is only necessary when the relative position of the cameras and projector is changed. Once calibrated, the **SLI** system can acquire a surface scan in about 35 seconds, including 16 seconds for adaptively adjusting the intensity scaling factor α for both cameras (see Section 6.2.2.1 for details) and 19 seconds for image acquisition ($38 \times 2 \times 0.25 = 19$ s).

6.3.2 Surface estimation errors

The **DBT** breast model was 3-D printed (Ender 5, Creality, China) with a 0.1 mm layer height using white **PLA** filament. The 3-D printed **DBT** breast was placed in between the compression plates, compressed to the thickness of the printed **DBT** phantom, and scanned using the dual-camera **SLI** system. The saturation scaling factors α were automatically determined using twenty iterations, resulting in a $\alpha = 0.8$ for both cameras. The two point-clouds from each camera-projector pair were transformed to the projector's coordinates, down-sampled, and merged prior to being denoised with the number of nearest neighbor points set to four and the outlier threshold set to one standard deviation from the mean of the average distance to those four neighboring points. The resulting point-cloud from the **SLI** system scan has 35,256 points.

Table 6.1 shows the mean and standard deviation of the residual of all the nodes in the estimated breast surface mesh. The z -extrusion method (EXT) results in the largest error (E_s) of all compared methods. While the top-sweep, side-sweep, and **SLI** methods all had similar standard deviations, the **SLI** method resulted in the smallest E_s .

6.3.3 Mean square error of optical property reconstruction

DOT reconstructions were performed using our in-house data analysis toolbox, Redbird-m [222]. An L -curve analysis is used to determine the regularization parameter as 3.16×10^{-10} , which is fixed over 10 Gauss-Newton iterations. The absorption coefficient of the spherical inclusion was set to be twice ($\mu_a = 0.016/\text{mm}$) that of the background tissue ($\mu_a = 0.008/\text{mm}$). The reduced scattering coefficient μ'_s was set to 1 mm^{-1} for both breast and inclusion tissues. A set of 32 (16 vertical, 16 horizontal) moving-bar source patterns [223] covering an area of $40 \times 40 \text{ mm}^2$ was

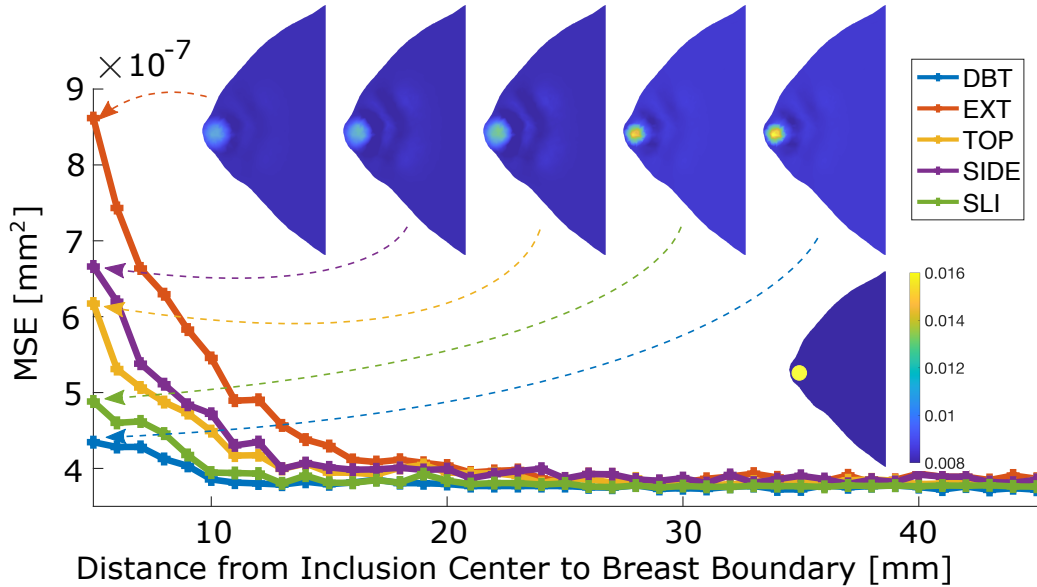


Figure 6.7: A comparison between the mean squared error (MSE) of the reconstructed absorption map using 4 estimated surfaces (EXT - z -axis extrusion, TOP - sweeping x/y contour along y/z contour, SIDE – sweeping y/z contour along x/y contour, and SLI – surface acquired from our structured-light imaging system) as well as the ground truth digital breast tomosynthesis surface. A 1 cm diameter spherical inclusion is moved away from the breast surface at various depths between 5 and 45 mm in 1 mm increments. Image slices (in x/y plane) of the reconstructed absorption coefficient (μ_a in mm^{-1}) (top-row) and the ground truth μ_a (bottom-right) are shown as insets.

centered at the spherical inclusion. Iso2Mesh was used to interpolate nodal values from the reconstructed mesh to the ground truth mesh based on linear interpolation in order for all reconstructed meshes to have the same number of nodes.

The **MSE** errors from these reconstructed images are summarized in Fig. 6.7, showing the effect of different surface estimation methods on the accuracy of optical property recovery. Overall, surface mesh accuracy appears to have a notable impact on relatively shallow tumors, with a depth of less than 25 mm. **MSE** values obtained using the **SLI** method closely follow those using the ground truth **DBT** mesh for most inclusion depths. The top- and side-sweep-based meshes followed similar trends, however, reporting higher errors compared to **SLI** especially when the tumor is relatively shallow. The maximum **MSE** value for the **SLI** mesh at a distance of 5 mm from the surface ($4.89 \times 10^{-7} \text{ mm}^2$) was 23% higher than the maximum **MSE** value for the **DBT** mesh ($4.35 \times 10^{-7} \text{ mm}^2$). In contrast, the single-axis-extrusion method (EXT) **MSE** was nearly twice higher ($8.62 \times 10^{-7} \text{ mm}^2$) than that from the **DBT** mesh. Although the **DBT** and **SLI** mesh **MSEs** plateau to their minimum around 15 mm from the surface, top-, side-, and extrusion-based mesh **MSEs** continue to decrease until a depth of 25 mm. Beyond the depth of 25 mm, the errors between different methods become minimal.

6.3.4 Full system *in-vivo* patient results

6.4 Discussion

The camera and projector re-projection errors in Section 6.3.1 represent an average error of fewer than 0.5 pixels in estimating the corner locations of a calibration checkerboard placed between 50 and 250 mm away [Fig. 6.2(b)] from the projector for all 35 checkerboard positions. Although the same illumination patterns and calibration checkerboard positions were used to calibrate each camera-projector pair, we find a slightly better calibration accuracy when the projector is paired with Camera 1 since Camera 1 is closer to the projector's lens (Fig. 6.2). The discrepancy in the re-projection errors of the two pairs is due in part to the asymmetry of the dual-camera setup. The asymmetry arises from the projector offset relative to its housing, making one camera closer to the projector than the other [Fig. 6.2(a)].

From Table 6.1, the single-axis extrusion method resulted in the highest surface error because it does not account for the curvature of the breast in the y/z plane [Fig. 6.6(b)]. Table 6.1 indicates that, on average, points in the extrusion-method-derived surface estimation mesh are ap-

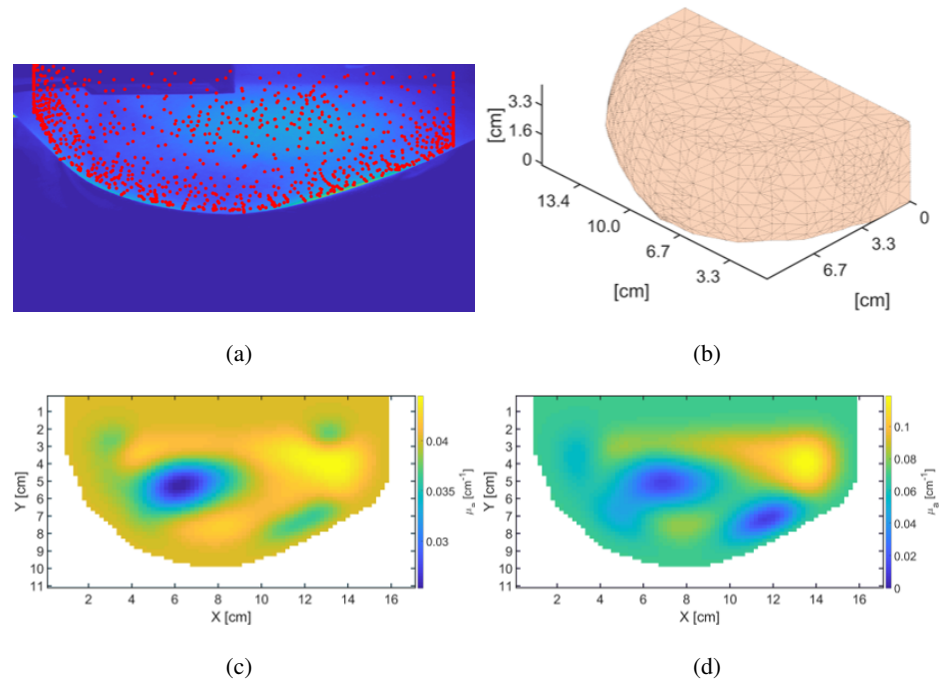


Figure 6.8: These images will be replaced with patient data showing structured-light imaging (SLI) in a healthy volunteer. I will also show reconstructed results and will cite Edward + Miguel. Edward to provide me with patient IDs that have good SLI acquisitions. (b) The generated 3D breast-shaped mesh from a SLI measurement on a healthy patient.

proximately 6.84 mm away from the **DBT** mesh. The top- and side-sweep methods decrease the surface estimation error by incorporating a second breast contour from the y/z plane [Figs. 6.6(c) and 6.6(d)]. Both methods improve the accuracy of surface estimations by approximating the 3-D curvature of the breast. We want to point out that both top-sweep and side-sweep methods require an additional camera to obtain two orthogonal views of the breast [224], which does not necessarily lead to simplified hardware compared to the **SLI** setup considering the mounting space constraints and lighting conditions [182]. While also requiring two cameras, our mammography-tailored **SLI** system can produce sub-millimeter resolution of the surface compared to the reference **DBT** breast model based on Table 6.1.

Our results also demonstrated that the improvement in surface estimation accuracy can lead to improved **DOT** reconstruction accuracy. Fig. 6.7 shows using breast surfaces derived from **SLI** can accurately recover the absorption profile compared to those recovered using the ground-truth (**DBT**) mesh at most tested tumor depths. For superficial/shallow (< 10 mm) tumors, the top- and side-sweep surface estimation methods followed similar trends to each other, reporting **MSEs** about 50% higher compared to those from using ground-truth (**DBT**) surface models, and about 30% higher than those from using **SLI** surfaces. As expected, the effect of the surface accuracy decreases as the inclusion is moving further away (> 25 mm) from the skin.

Despite the ability to produce sub-millimeter resolution of breast surfaces in poorly lit and confined mammography-like settings, both our **SLI** system and our analysis have limitations. Firstly, the span of the output point-cloud from our **SLI** system is limited to the area of the breast that is well-illuminated by the projector. As a result, tissue boundaries near the chest wall or those in direct contact with the compression plate may not be well covered due to the limited angles of the projector/camera line-of-sight. Still, for **DOT** of a compressed breast, capturing a significant portion of the front-facing breast tissue as our system does, provides quantitative differences in reconstructions, as shown above. Future improvement of this system should consider using more compact, wide-angle projectors, higher resolution cameras, and patterns with higher order binary codes to both expand the field-of-view and increase the point-cloud resolution. Secondly, a 3-D printed breast model was used to experimentally compare different shape acquisition methods. Different choices of extruder sizes, filament colors, and printing techniques could impact the surface texture of the printed phantom and slightly alter the surface estimation errors. Finally, the quantification of reconstruction errors was based on simulations using a single set of pre-determined breast models, tumor size and shape, tumor contrast, and wide-field pattern size. An experimental validation using heterogeneous phantoms may produce more realistic comparisons.

CHAPTER 7

3-D PRINTED PHANTOMS

7.1 Introduction

In order to evaluate the performance of the **NIR** systems we have built, we need to use phantoms. Phantoms are physical samples carefully made to mimic the optical properties of human tissues[20]. By imaging these objects of known optical properties, we can evaluate the accuracy of a new system by comparing its result against existing systems. Creating these phantoms is complex: not only do you need to create recipes that lead to desired optical properties, but phantoms must also be manufactured in specific geometries tailored to what the **NIR** system will measure. To address the optical properties, phantom makers tend to focus on mimicking the absorption coefficient (μ_a) and the reduced scattering coefficient (μ'_s) of biological tissue [22] by using mixtures of scattering agents and absorbing pigments with a clear base [23, 24]. The shape of the phantom is typically created using traditional fabrication techniques, either mold casting [25] or spin coating [27].

Traditionally, as **NIR** imaging was in its infancy, these methods sufficed for simple phantoms. However, these methods fall short of supporting complex geometries. As new **NIR** systems are developed to image the brain [28, 29] and the breast, we will need to evaluate their performance with phantoms that have complex structural and physiological properties. While some phantom makers use intricate methods and procedures to develop geometrically complex phantoms [26], these phantoms take days to manufacture, require lots of equipment and expertise, and the manual process leads to geometry and optical property variations due to human variability. Thus, to support the system development, calibration, and testing of new imaging methods [30, 31] (like the **NIR** systems developed in this thesis), we need a new method to manufacture phantoms with spatially varying optical properties and anatomically accurate geometries.

Rather than add structure-generating methods to traditional phantom making, we propose a method to add customizable optical properties to a digital fabrication method that is already engineered to produce arbitrary geometry—fused-deposition modeling (**FDM**). **FDM** is a form of 3-D printing that creates a 3-D object by adding solid material layer-by-layer [24]. While traditional 3-D printing uses a single filament material to generate a 3-D object, we proposed the mixing of grey (absorbing), white (scattering), and transparent (base) filament colors to produce the desired optical properties.

3-D printing for phantom development allows for customizable properties using raw printing materials and the creation of spatially varying optical properties within a 3-D printed phantom. This allows the creation of a wide range of phantoms with precisely known optical properties, geometries, and inclusions of various resolutions (size, shape, depth). Most significantly, the design of a 3-D printed standardized calibration phantom for DOT minimizes geometry and optical property variations due to human variability. In this way, researchers can manufacture identical phantoms using *in-situ* materials with resolutions limited only by their 3-D printer, effectively allowing independent DOT systems to be characterized by the same exact phantom.

In this chapter, we will detail our method to develop 3-D printed phantoms. We will first describe a workflow to characterize new filaments to account for variations in lots of the same color filament. We then show details of a slicer with the ability to slice an assembly of multiple STL files. The slicer is able to assign filament ratios (tissue types) to each individual STL, allowing the printer to adjust the mixing ratio of the extruder as it prints embedded inclusions into the large geometric print. To demonstrate the capabilities of the slicer, we will slice anatomical geometries with multi-tissue types for each of the three **NIR** systems in this study, including a finger with arteries for **MOXI**, a head phantom with spherical inclusions for use with **MOBI**, and a breast-shaped phantom with inclusions for **OMCI**. Finally, in order to encourage the use of our method, we will disclose a list of lessons learned to help others attempt to replicate our phantoms.

7.2 3-D Printing Hardware

This project utilizes an experimental **FDM** multi-material 3-D printer (QuadFusion, M3D). This marlin-based printer has an extrusion bar-based frame and uses stepper motors to control motion. The extrusion head is composed of small stepper motors to guide four filaments through a metal nozzle with a polytetrafluoroethylene (**PTFE**) insert. The **PTFE** insert is a cylindrical piece with 4 milled holes that extend from end to end. Mixing occurs in the nozzle tip. Due to the need

to mix filaments into one nozzle exit, we used polyethylene terephthalate glycol (**PETG**) instead of the standard **PLA** filament. **PLA** is the most popular thermoplastic for 3-D printing because of its cost, ease of print (it is semi-flexible and very forgiving), and it does not off-gas any fumes. However, **PLA** is difficult to mix with other materials due to its limited temperature range. At high temperatures (above 200° Celsius), **PLA** releases water which causes a high-pressure build-up in nozzles. To resist the higher temperate and water, **PETG** is used. **PETG** is more viscous at higher temperatures, allowing it to easily fuse with other **PETG** filaments.

7.3 New Filament Characterization

The filament profiles are the derived settings used for a particular filament. Although the majority of printing settings are consistent across **PETG** filaments, certain features must be accounted for, particularly, the extrusion multipliers and retraction amount. extrusion multiplier (**EM**) is a setting used to account for variability in extrusion amounts. An extrusion multiplier of 1 means that 1 mm of filament is extruded for every 1 mm requested. Due to the filament path (the Bowden tube, motor teeth, varying temperatures), certain filaments in certain printers may require over- or under-extrusion to extrude the correct amount of filament. The retraction amount is the amount of filament to pull back up into the nozzle as the print head moves in between printing layers. When this value is too low, you will see “stringing” in prints from the oozing of material while the head is in motion. Too much retraction and the printer will not print the first few millimeters upon restarting since the nozzle is empty of filament.

To account for variations in filaments of the same color by the same manufacturer, we have developed a method to characterize filaments and create filament profiles for each spool of filament. In fairness, the variability in the extrusion multiplier is not entirely due to the manufacturer. The QuadFusion head is a complex head that requires filaments to be driven through curved paths and high pressure that result in friction. We calculate filament-specific **EMs** for each spool used in our printer by printing a square wall with the thickness of a single path width (**PW**). We then calculate the new **EM** based on the desired path width and the actual path width of the print using the formula $EM_{new} = EM_{printed} \times (PW_{desired}/PW_{measured})$. The steps are outlined in Figure 7.1(a).

A 3-D printed tissue type is simply a mixing ratio of multiple characterized filament profiles. While one filament profile informs of the settings for printing a single filament, we have to create combined printing settings when mixing multiple filaments (tissue types). This is done as a weighted average of the settings scaled by the mixing ratios. For example, if white,

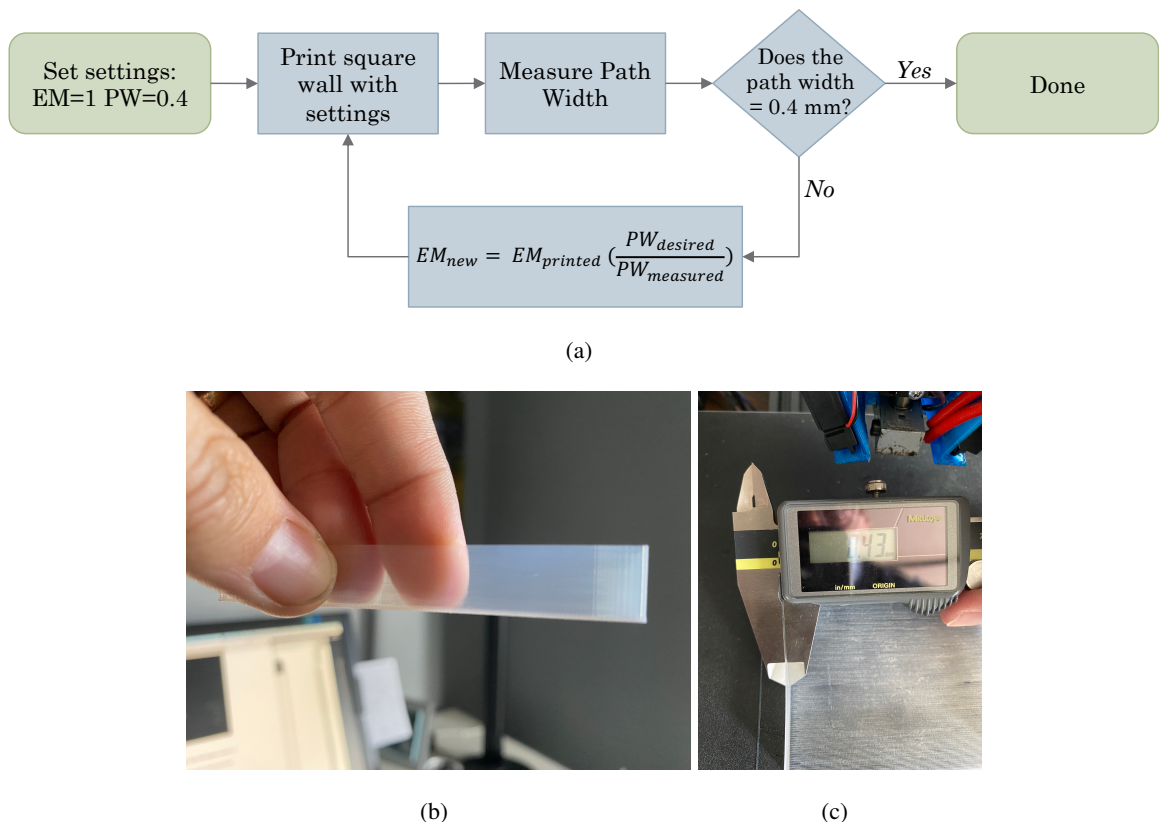


Figure 7.1: (a) Flowchart showing how to use measured path widths to adjust extrusion multiplier values when characterizing filaments. (b) Printed square wall using clear filament. (c) Caliper measurements show over-extrusion.

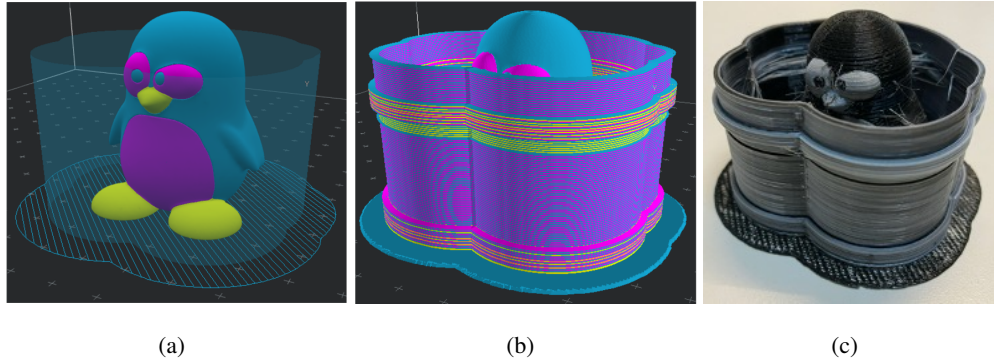


Figure 7.2: The “caging” purge method (a) An example penguin composed of three different tissue types. (b) The same penguin model with the cage shown. The colors of the cage indicate the colors on that segment of the print. (c) Resulting 3-D printed penguin.

grey, black, and clear filaments each have extrusion multipliers of 1, 0.98, 1, and 0.9, respectively, and we want to mix them in a 30/20/0/50 ratio, then the final extrusion multiplier would be $(1 \times 30 + 0.98 \times 20 + 1 \times 0 + 0.9 \times 50) / (30 + 20 + 0 + 50) = 0.946$. Similarly, the extrusion motors are driven at scaled rates based on the filament mixing ratio.

7.4 Multi-filament slicing

7.4.1 Artifacts for purging during transition

One difficulty in fused multi-material 3-D printing not found in single filament printing is the need to purge the nozzle in between changing mixing ratios for different tissue types on the same layer. For example, if we want two separate mixing ratios for concentric rods, the nozzle needs to be purged in between printing the outside color and printing the inside color. Purging refers to the extrusion of sacrificial filament when the outputted mixed filament is transitioning between different two ratios (tissue types).

We have implemented a “caging” method in which a cage is built around the print to purge the nozzle. The method is an extension of the “brim” artifact commonly used to help prints adhere to the print bed. Essentially, at every layer, concentric shapes around the model are printed for each ratio. This allows the nozzle to fully transition to a new mixing ratio prior to continuing the print. This results in a cage around the print.

7.4.2 MOXI, MOBI, and OMCI system slicing

7.5 Lessons learned for use of PETG in filament mixing

The use of PETG filament, a “caging” purging method, mixed filament ratio-based extrusion multipliers, and an experimental FDM 3-D printer has taught us many lessons. To facilitate future researchers in this space, here is a list of lessons learned and pitfalls to avoid.

- **BED MATERIAL:** PETG sticks very well to the printing bed. The use of sacrificial generic blue painter’s tape on the print bed will facilitate removal by removing the print from the bed by pulling on the tape itself.
- **BED LEVELING:** Add a decent gap between the nozzle and the bed. Typical 3-D printers level the bed by using a single sheet of regular printing paper as the unit of measure between the nozzle and the print bed. To account for the “gooey”-ness of PETG, use 3 sheets of paper.
- **BED TEMPERATURE:** Start the bed temperature around 80° C. Do not heat above 100° C. Higher bed temperatures are better for bed adhesion, but PETG already adheres pretty well. Consider decreasing the space between the nozzle and the bed before increasing the bed temperature.
- **NOZZLE TEMPERATURE:** PETG prints between 230 and 250° C. However, PTFE (which is what the tube that aligns the filaments prior to being mixed in the nozzle is made of) has a melting point between 250 and 260° C. Start at 230° C and do some test prints. If you hear a knocking noise during printing, your extruder is skipping, and you should increase the nozzle temperature by 5° C.
- **RETRACTION SPEEDS:** Do not retract PETG at high speeds. Set the retraction speed to around 25 mm/s. The retraction distance should be set at about 3 or 4 millimeters for direct drive extruders. With PETG, the retraction speed is more important than distance. If you still have oozing and stringing, try lowering the retraction speed.
- **TRAVEL SPEED:** One more parameter that will help in reducing oozing is the travel speed. PETG tends to drip from the tip of the nozzle, especially if the nozzle temperature is high. To combat this, try increasing the travel speed to reduce the time the printer is not actively extruding.

- PRINT SPEED: PETG is very sensitive to print speed. Printing too fast results in poor layer adhesion, extruder skipping, and low print quality. Printing too slow results in deformed parts, stringing, and oozing. A good place to start is between 50 and 55 mm/s. We suggest 25 mm/s for the first layer and the outer wall, while travel moves should be as fast as possible, at least 120 mm/s, to avoid oozing.
- FANS: We recommend printing without fans for the first two layers. All other layers should have the fan running at 100%.

CHAPTER 8

CONCLUSION

8.1 Summary

In this work, we have elevated state-of-the-art **NIR** imaging through the design and development of three **NIR** imaging systems to address three grand challenges and demonstrate the potential broad application of **NIR** imaging across populations and settings. In Chapter 3, we addressed the **USAID** challenge through developing an ultra-low-cost colored-paper-filter-based mobile phone oximeter. **MOXI** leverages a mobile phone’s flash **LED** as the broadband source and the phone’s camera as an area detector. By covering half of the field of view of the camera with a colored paper, we can obtain two spectra that have traversed the finger to determine **SpO₂**. Measurements on healthy subjects in a pilot study reveal that our **MOXI** device can follow expected changes in **SpO₂** during breath holding compared to a reference pulse oximeter.

The **BRAIN** initiative challenge was addressed in Chapter 5. We designed and validated a lightweight, fiberless, diamond-shaped modular **fNIRS** system with features tailored toward use in natural environments. Its shape and flexible-circuit-based design allow for the system to conform to the scalp and increase optode-to-scalp coupling during use. A dense communication network allows for the automatic determination of the connection topology for the creation of spatial multiplexing groupings to increase the full frame rate of any probe configuration relative to sequential encoding methods. The use of 3-D orientation sensors allows for the determination of optode positions without the need for external hardware. Our **MOBI** modules were validated against a commercial system in cuff occlusion and serial subtraction tests. The **MOBI fNIRS** system directly addresses the ergonomic, automatic, and usability concerns necessary for the adoption of wearable systems by the masses.

The third challenge, funded by the NIH’s NCI, is addressed in Chapter 6 where we developed and validated a low-profile, low-cost, and robust SLI-based breast surface acquisition system that can be used in confined low-light mammography-like settings to obtain 3-D breast surfaces. Once calibrated, our SLI system can achieve sub-millimeter accuracy with a data acquisition time of less than 40 seconds. We quantified the impact of breast surface estimation methods on DOT optical property reconstruction accuracy of inclusions embedded at various depths and found that obtaining accurate breast surfaces is important for DOT reconstructions of shallow lesions with a depth less than 25 mm. A compact breast shape acquisition system that can fit between mammography compression plates can not only help improve parallel-plate breast DOT image reconstructions but can also be incorporated into standard x-ray based DBT scanners to help improve 3-D DBT image reconstructions. Currently, clinical DBT image reconstructions are performed without considering the actual breast shape [225] and often result in an inaccurate cylindrical quasi-3D breast shape [222]. Explicitly capturing and considering breast 3-D shapes is expected to lead to improved image quality in DBT and other model-based breast imaging modalities.

Additionally, we contributed to the adoption of NIR imaging through defining a systematic method for the creation of optical phantoms as well as through building a software platform to aid in designing new fNIRS systems. In Chapter 4, we developed a MATLAB-based modular probe design toolbox, MOCA, with the goal of providing fNIRS developers with a systematic yet easy-to-use software platform to navigate the large design space of modular fNIRS probes and provide metrics-based guidance. MOCA simplifies the design problem with module-level parameters such as size, shape, and optode layout as well as probe-level parameters such as the maximum source-to-detector separation and ROI geometry to characterize a modular probe. It offers the ability to perform operator-guided sweeping of probe parameters such as orientation, spacing, and module staggering offset, helping designers explore alternative designs that potentially improve upon existing probes or outline spectra of trade-offs. MOCA is quantitative, guided by application-specific fNIRS performance metrics, including channel distribution, average brain sensitivity, and spatial multiplexing groups, making it possible for quantitative characterization and comparison between various design decisions. Applying MOCA in several case studies, we identified several valuable design considerations that have not been widely recognized, including the importance of fine-tuning module orientation, spacing, and staggering distance. In the meantime, these case studies also demonstrate the complexity of modular probe optimization, where multiple variables compete and eventually lead to alternative designs with various trade-offs. While MOCA was not designed to provide full automation for complex probe design and optimization, it offers fNIRS probe designers

Table 8.1: Pugh Chart ranking of NIR systems

Ility Name	Pulse Oximeter	MOXI	MOBI	OMCI
Adaptability*	0	0	3	1
Affordability	0	2	-1	-3
Comfortability	0	-1	3	-3
Conformability	0	-1	3	-1
Extensibility*	0	2	1	3
Interoperability*	0	0	3	2
Maintainability	0	3	-1	-3
Manufacturability	0	3	-1	-3
Modifiability*	0	1	2	3
Operability	0	-1	-2	-3
Portability	0	3	-1	-3
Reconfigurability*	0	1	2	0

a suite of powerful tools, including module tiling, routing, re-orientation, and fine-tuning of module spacing and staggering offset, with each outcome quantified by meaningful performance metrics. **MOCA** is expected to attract more research interests towards developing next generation modular **fNIRS** systems. Similarly, in Chapter 7, we detailed a method for characterizing new filaments for use in multi-material fusion-based 3-D printing. We also show a modified brim method for efficiently purging filament when a print changes between mixing ratios on a single layer. Through this process, we show how we can design and setup the fabrication of anatomically complex optical phantoms for validating arbitrary **NIR** imaging systems, including the three systems developed in this thesis.

8.2 Comparing system lifecycle properties

Finally, we revisit the system lifecycle properties defined in Table 2.1. We use the Pugh method [16] to qualitatively rank each of the three **NIR** systems against a reference design using the ilities as the set of criteria. The reference **NIR** system is a standard finger-clip-based, two-wavelength pulse oximeter. Each ility can vary between ± 3 indicating that the system is ranked better (+), worse (-), or the same as (0) the reference design. A value of 3 allows for each of the three systems to all be ranked better (or worse) than the reference design while still providing relative ranking between the three systems. The results of this ranking are shown in Table 8.1.

Adaptability **MOXI** is designed for a specific function and is not easily adaptable for other vital

signs. **OMCI** can be adapted for other applications. For example, the **SLI** system can be used on its own for surface estimation of other body parts (e.g. facial landmark identification). It is **MOBI**, however, that is ranked highest due to its modular design that allows for spectroscopy or **DOT** applications at various sites.

Affordability **OMCI** is clearly the most expensive **NIR** system we built due to its numerous subsystems and expensive hardware. Although **MOBI** has similar optical components as a traditional pulse, it does use more complex electronics and interfaces that drive up the cost. In contrast, the **MOXI** is more affordable than traditional pulse oximeters since it only requires a small piece of paper. The reason for giving it a rank of three is because **MOXI** still requires a smartphone, which a user may or may not have in their possession.

Comfortability The silicone covers and wireless capability of the **MOBI** modules allow them to be used for hours at a time. On the other hand, **OMCI** requires heavy compression of the breast to minimize the thickness between paddles. This is so uncomfortable that we have to limit the time in compression to less than 3 minutes. The **MOXI** system, although highly portable, requires the user to actively press onto the camera phone, which can cause discomfort over long-term use compared to the passive design of a traditional finger-clip pulse oximeter.

Conformability The reflectance-based design of **MOXI** relies on the flat surface of a phone camera that is susceptible to motion. **OMCI**, like **MOXI**, uses flat surfaces that compress the breast preventing motion. However, the mechanical principle of compressing tissue using two fixed-shaped surfaces is identical to a traditional pulse oximeter in the sense that neither adjusts to different user shapes. In contrast, the flexible-circuit-based **MOBI** modules conform easily to the scalp.

Extensibility Given the context, our **OMCI** system can be easily extended to include features from state-of-the-art **DOT** research including the use of optimal wide-field illumination patterns and sizes, new **SLI** illumination patterns, and compression-sensor-based tomography. In contrast, **MOBI** would leverage features from portable **fNIRS** systems, which rely on the use of new driving electronics and optodes, which require new circuit designs. It, however, unlike a pulse oximeter, varies the intensity of light to accommodate hair artifacts. **MOXI** can do software updates easily, but features to support other vital signs necessitate specific electronics that the mobile-phone in use may not have.

Interoperability **MOXI** is not better or worse in its ability to operate with other imaging systems.

By design, **OMCI** is capable of being integrated in existing x-ray mammography systems.

However, **MOBI** receives the highest score due to the auxiliary input of the master module, allow its measurements to synchronize with any other system that can output a **TTL** signal.

Maintainability Our **MOXI** system is ranked highest because it can be easily maintained with regular software updates and replacing its inexpensive pieces of paper. Our **MOBI** modules are robust and designed to be used in natural settions. However, they were ranked lower than the reference design due to the high number of components (flat-flex cables, caps, master modules) that can potentially break and require replacement. Due to the complexity of our **OMCI** system, it is ranked the lowest in maintainability.

Manufacturability **MOBI** modules have very similar optical components to a finger-clip pulse oximeter, thus same expertise used in designing the circuit and fabricating the physical enclosure of a pulse oximeter clip is needed for fabricating a **MOBI** module. We ranked them –1 because a **MOBI** system also requires the fabrication of the master and trigger boards, as well as the creating of the headgear that holds the modules in place. Our **OMCI** system requires not only fabricating circuits but also mechanical assemblies and sensitive optical fibers. In contrast, **MOXI** simply requires a piece of colored paper.

Modifiability Modifiability refers to the ability to change a default set of specified parameters. Besides the color of the paper filter, **MOXI** does not allow any user changes. On our **MOBI** system, a use can change the source currents, detector gains, and sampling strategy (sequen-tially and spatial multiplexing). **OMCI** receives the highest ranking in this category due to the ability to change the wide-field and **SLI** patterns, position of the radio frequency (**RF**) source location, and scaling factor sensitvity.

Operability Although a lot of consideration was taken into the usability of the software **GUI** of our **OMCI** system, it is clear from the extensive training that was required to obtain human subject data that the complexity of all the subsystems and calibration steps prior to acquisition make this system difficult to use, even for a knowledgeable user. Although conceptually similar to a pulse oximeter, our **MOBI** modules require relatively longer setup times to connect modules and affix a cap onto a user. Our **MOXI** system only requires user input into a very basic application. Also easy to operate, it is ranked less than zero because a finger-clip-based pulse oximeter requires no user input.

Portability Our **MOXI** system receives the highest ranking because it only requires a piece of paper and its Moximeter application can be easily downloaded. Although wearable and portable, compared to a traditional pulse oximeter, our **MOBI** system requires the transportation of multiple modules and supporting electronics. Our **OMCI** breast imaging system is much less portable than a pulse oximeter due to its size and weight.

Reconfigurability **OMCI** requires a well-aligned and calibrated system to function. In theory, **MOXI** can use different colored paper filters and the Moximeter application attempts to account for the misplacement of the filter on the camera. **MOBI** is by far the most reconfigurable of the three **NIR** systems by simply reconnected the modules in different arrangements. However, the optode layout within a **MOBI** module is fixed, which is why the rank is set to two.

8.3 Future Outlook

This dissertation is an opportunity to course correct. For much of the twentieth century, harmful, ionizing x-ray imaging was the dominant medical imaging tool. It took 82 years after the introduction of x-ray imaging for the medical community to demonstrate the first whole-body **MRI** scan. In the 45 years since, we are still using potentially harmful radiological and mediconuclear approaches and limiting our understanding of ourselves through modalities that are not conducive to the unrestricted measurements required globally today. As a community, we owe it to ourselves to reflect on the use of our innovations to ensure a viable and healthy future. With this in mind, the call to action of this thesis is to turn our attention towards the translation of the emerging, portable, non-invasive, non-ionizing, and low-cost **NIR** imaging modality. This will require us to find creative methods to navigate regulatory pathways, improve computation efficiency, and leverage advanced electronics to address the pressing needs of an ever-increasing population. We invite researchers to accelerate innovation through the use of our tools to continue to advance the state-of-the-art of **NIR** systems and bring to light (pun intended) new harmless, advantageous methods and features tailored towards a global applications.

REFERENCES

- [1] Christopher M. Aasted, Meryem A. Yücel, Robert J. Cooper, Jay Dubb, Daisuke Tsuzuki, Lino Becerra, Mike P. Petkov, David Borsook, Ippeita Dan, and David A. Boas. Anatomical guidance for functional near-infrared spectroscopy: AtlasViewer tutorial. *Neurophotonics*, 2(2):020801, 2015.
- [2] Gary E. Strangman, Zhi Li, and Quan Zhang. Depth Sensitivity and Source-Detector Separations for Near Infrared Spectroscopy Based on the Colin27 Brain Template. *PLoS ONE*, 8(8), 2013.
- [3] Kenneth Clark, Bruce Vendt, Kirk Smith, John Freymann, Justin Kirby, Paul Koppel, Stephen Moore, Stanley Phillips, David Maffitt, Michael Pringle, Lawrence Tarbox, and Fred Prior. The cancer imaging archive (TCIA): Maintaining and operating a public information repository. *Journal of Digital Imaging*, 26(6):1045–1057, 2013.
- [4] Olivier L de Weck, Adam M Ross, and Donna H Rhodes. Investigating Relationships and Semantic Sets amongst System Lifecycle Properties (Ilities). In *Third International Engineering Systems Symposium CESUN 2012, Delft University of Technology*, number June in 3, pages 18–20, 2012.
- [5] Qianqian Fang. Mesh-based Monte Carlo method using fast ray-tracing in Plücker coordinates. *Biomed. Opt. Express*, 1(1):165–175, aug 2010.
- [6] Carmen E. Sanchez, John E. Richards, and C. Robert Almlie. Age-specific MRI templates for pediatric neuroimaging. *Developmental Neuropsychology*, 37(5):379–399, 2012.
- [7] Richard B Gunderman. *X-ray vision: the evolution of medical imaging and its human significance*. Oxford University Press, 2012.

- [8] John K Iglehart. The New Era of Medical Imaging — Progress and Pitfalls. *New England Journal of Medicine*, 354(26):2822–2828, 2006.
- [9] Paul Suetens. *Fundamentals of medical imaging*. Cambridge University Press, 3 edition, 2017.
- [10] Eugenio Picanco. Sustainability of medical imaging. *BMJ*, 328(7439):578–580, 2004.
- [11] Frederic H. Fahey. Data acquisition in PET imaging. *Journal of Nuclear Medicine Technology*, 30(2):39–49, 2002.
- [12] Vincent Chan and Anahi Perlas. *Basics of Ultrasound Imaging*, pages 13–19. Springer New York, New York, NY, 2011.
- [13] Donald B. Plewes and Walter Kucharczyk. Physics of MRI: A primer. *Journal of Magnetic Resonance Imaging*, 35(5):1038–1054, 2012.
- [14] Miguel Adrián Mireles Núñez. *Hybrid Diffuse Optics For Translational Oncology and Nano-Biophotonics: Towards a Theranostic Approach For Emerging Cancer Therapies*. PhD thesis, Barcelona Institute of Science and Technology, 2018.
- [15] Saving Lives at Birth. A Grand Challenge for Development, 2021.
- [16] Stuart Pugh. Concept selection: a method that works. In *Proceedings of the International conference on Engineering Design*, pages 497–506, 1981.
- [17] Lihong V. Wang and Hsin-I Wu. *Biomedical Optics: Principles and Imaging*. John Wiley and Sons, Ltd, 2009.
- [18] Ashley J Welch, Martin J C van Gemert, and Willem M Star. Definitions and overview of tissue optics. In *Optical-thermal response of laser-irradiated tissue*, pages 27–64. Springer, 2010.
- [19] Wei Du, Ying Wang, Qingming Luo, and Bi-Feng Liu. Optical molecular imaging for systems biology: from molecule to organism. *Analytical and bioanalytical chemistry*, 386(3):444–457, oct 2006.
- [20] Brian W Pogue and Michael S Patterson. Review of tissue simulating phantoms for optical spectroscopy, imaging and dosimetry. *Journal of Biomedical Optics*, 11(4):1–16, jul 2006.

- [21] John G. Webster, John W. Clark, Michael R. Neuman, Walter H. Olson, Robert A. Peura, Frank P. Primiano, Melvin P. Siedband, and Lawrence A. Wheeler. *Medical instrumentation: Application and design*. John Wiley and Sons, Ltd, 4th edition, 2010.
- [22] Laura A Dempsey, Melissa Persad, Samuel Powell, Danial Chitnis, and Jeremy C Hebden. Geometrically complex 3D-printed phantoms for diffuse optical imaging. *Biomedical optics express*, 8(3):1754–1762, feb 2017.
- [23] Jeremy C Hebden, David J Hall, Michael Firbank, and David T Delpy. Time-resolved optical imaging of a solid tissue-equivalent phantom. *Applied Optics*, 34(34):8038–8047, 1995.
- [24] Erbao Dong, Zuhua Zhao, Minjie Wang, Yanjun Xie, Shidi Li, Pengfei Shao, Liuquan Cheng, and Ronald X Xu. Three-dimensional fuse deposition modeling of tissue-simulating phantom for biomedical optical imaging. *Journal of Biomedical Optics*, 20(12):1–10, nov 2015.
- [25] Camerin Hahn and Sima Noghanian. Heterogeneous Breast Phantom Development for Microwave Imaging Using Regression Models. *International Journal of Biomedical Imaging*, 2012:803607, 2012.
- [26] A T Mobashsher and A M Abbosh. Three-Dimensional Human Head Phantom With Realistic Electrical Properties and Anatomy. *IEEE Antennas and Wireless Propagation Letters*, 13:1401–1404, 2014.
- [27] Jihoon Park, Yunjin Bae, Youngwoo Bae, Heesung Kang, Kyoung-Joung Lee, and Byungjo Jung. Fabrication of double layer optical tissue phantom by spin coating method: mimicking epidermal and dermal layer. In *Proc.SPIE*, volume 8583, feb 2013.
- [28] Jeremy C Hebden, Adam Gibson, Rozarina Md Yusof, Nick Everdell, Elizabeth M C Hillman, David T Delpy, Simon R Arridge, Topun Austin, Judith H Meek, and John S Wyatt. Three-dimensional optical tomography of the premature infant brain. *Physics in Medicine and Biology*, 47(23):4155–4166, 2002.
- [29] Arno Villringer and Britton Chance. Non-invasive optical spectroscopy and imaging of human brain function. *Trends in Neurosciences*, 20(10):435–442, 1997.
- [30] Albert E Cerussi, Robert Warren, Brian Hill, Darren Roblyer, Anais Leproux, Amanda F Durkin, Thomas D O’Sullivan, Sam Keene, Hosain Haghany, Timothy Quang, William M

- Mantulin, and Bruce J Tromberg. Tissue phantoms in multicenter clinical trials for diffuse optical technologies. *Biomedical optics express*, 3(5):966–971, may 2012.
- [31] Phuong Diep, Sanjana Pannem, Jordan Sweer, Justine Lo, Michael Snyder, Gabriella Stueber, Yanyu Zhao, Syeda Tabassum, Raeef Istfan, Junjie Wu, Shyamsunder Erramilli, and Darren Roblyer. Three-dimensional printed optical phantoms with customized absorption and scattering properties. *Biomedical optics express*, 6(11):4212–4220, oct 2015.
- [32] Thomas A Neff. Routine Oximetry: A Fifth Vital Sign? *Chest*, 94(2):227, 1988.
- [33] Paul Aaron Bohn. *Mobile phone pulse oximeter*. PhD thesis, Northeastern University, 2015.
- [34] James E Sinex. Pulse oximetry: Principles and limitations. *The American Journal of Emergency Medicine*, 17(1):59–66, 1999.
- [35] Santiago Lopez. Pulse Oximeter Fundamentals and Design. Technical report, Freescale Semiconductor, Inc., 2012.
- [36] Edward D. Chan, Michael M. Chan, and Mallory M. Chan. Pulse oximetry: Understanding its basic principles facilitates appreciation of its limitations. *Respiratory Medicine*, 107(6):789–799, 2013.
- [37] David A. Boas, Clare E. Elwell, Marco Ferrari, and Gentaro Taga. Twenty years of functional near-infrared spectroscopy: Introduction for the special issue. *NeuroImage*, 85(1):1–5, 2014.
- [38] Marco Ferrari and Valentina Quaresima. A brief review on the history of human functional near-infrared spectroscopy (fNIRS) development and fields of application. *NeuroImage*, 63(2):921–935, 2012.
- [39] Felix Scholkmann, Stefan Kleiser, Andreas Jaakko Metz, Raphael Zimmermann, Juan Mata Pavia, Ursula Wolf, and Martin Wolf. A review on continuous wave functional near-infrared spectroscopy and imaging instrumentation and methodology. *NeuroImage*, 85:6–27, 2014.
- [40] Paola Pinti, Ilias Tachtsidis, Antonia Hamilton, Joy Hirsch, Clarisse Aichelburg, Sam Gilbert, and Paul W Burgess. The present and future use of functional near-infrared spectroscopy (fNIRS) for cognitive neuroscience. *Annals of the New York Academy of Sciences*, 1464(1):5–29, mar 2020.

- [41] S C Bunce, M Izzetoglu, K Izzetoglu, B Onaral, and K Pourrezaei. Functional near-infrared spectroscopy. *IEEE Engineering in Medicine and Biology Magazine*, 25(4):54–62, 2006.
- [42] M Izzetoglu, S C Bunce, K Izzetoglu, B Onaral, and a. K Pourrezaei. Functional brain imaging using near-infrared technology. *IEEE Engineering in Medicine and Biology Magazine*, 26(4):38–46, 2007.
- [43] Stéphane Perrey. Non-invasive NIR spectroscopy of human brain function during exercise. *Methods*, 45(4):289–299, 2008.
- [44] D A Boas, D H Brooks, E L Miller, C A DiMarzio, M Kilmer, R J Gaudette, and Quan Zhang. Imaging the body with diffuse optical tomography. *IEEE Signal Processing Magazine*, 18(6):57–75, 2001.
- [45] J P Culver, V Ntziachristos, M J Holboke, and a G Yodh. Optimization of optode arrangements for diffuse optical tomography: A singular-value analysis. *Optics letters*, 26(10):701–703, 2001.
- [46] S R Arridge. Optical tomography in medical imaging. *Inverse Problems*, 15(2):R41–R93, 1999.
- [47] Simon R Arridge and John C Schotland. Optical tomography: forward and inverse problems. *Inverse Problems*, 25(12):123010, 2009.
- [48] T Durduran, R Choe, W B Baker, and A G Yodh. Diffuse Optics for Tissue Monitoring and Tomography. *Reports on progress in physics. Physical Society (Great Britain)*, 73(7):76701, jul 2010.
- [49] Martin Schweiger, Ilkka Nissilä, David A Boas, and Simon R Arridge. Image reconstruction in optical tomography in the presence of coupling errors. *Applied Optics*, 46(14):2743–2756, 2007.
- [50] Paul C Pearlman, Max A Viergever, Josien P Pluim, Arthur Adams, Sjoerd G Elias, and Willem P Th. M Mali. Mono- and multimodal registration of optical breast images. *Journal of Biomedical Optics*, 17(8):1–11, aug 2012.
- [51] Quing Zhu, Poornima U Hegde, Andrew Ricci, Mark Kane, Edward B Cronin, Yasaman Ardeshirpour, Chen Xu, Andres Aguirre, Scott H Kurtzman, Peter J Deckers, and Susan H

- Tannenbaum. Early-Stage Invasive Breast Cancers: Potential Role of Optical Tomography with US Localization in Assisting Diagnosis. *Radiology*, 256(2):367–378, aug 2010.
- [52] Qianqian Fang, Juliette Selb, Stefan A Carp, Gregory Boverman, Eric L Miller, Dana H Brooks, Richard H Moore, Daniel B Kopans, and David A Boas. Combined Optical and X-ray Tomosynthesis Breast Imaging. *Radiology*, 258(1):89–97, jan 2011.
- [53] Bin Deng, Maxim Fradkin, Jean-Michel Rouet, Richard H. Moore, Daniel B. Kopans, David A. Boas, Mats Lundqvist, and Qianqian Fang. Characterizing breast lesions through robust multimodal data fusion using independent diffuse optical and x-ray breast imaging. *Journal of Biomedical Optics*, 20(8):080502, 2015.
- [54] Samuel Bélanger, Maxime Abran, Xavier Intes, Christian Casanova, and Frederic Lesage. Real-time diffuse optical tomography based on structured illumination. *Journal of Biomedical Optics*, 15(1):1–7, jan 2010.
- [55] Jiqiao Yang, Run Zhang, Jiani Shen, Yuanyuan Hu, and Qing Lv. The Three-Dimensional Techniques in the Objective Measurement of Breast Aesthetics. *Aesthetic Plastic Surgery*, 39(6):910–915, 2015.
- [56] Jason Geng. Structured-light 3D surface imaging: a tutorial. *Advances in Optics and Photonics*, 3(2):128, 2011.
- [57] Daniel Moreno and Gabriel Taubin. Simple, accurate, and robust projector-camera calibration. In *Proceedings - 2nd Joint 3DIM/3DPVT Conference: 3D Imaging, Modeling, Processing, Visualization and Transmission*, pages 464–471. IEEE, 2012.
- [58] Jerrold T. Bushberg, J. Anthony Seibert, Edwin M. Leidholdt Jr., and John M. Boone. *The Essential Physics of Medical Imaging*. LWW; Third, North American edition, 3rd edition, 2011.
- [59] Olivier L de Weck, Daniel Roos, and Christopher L. Magee. *Engineering Systems: Meeting Human Needs in a Complex Technological World*. The MIT Press, 2011.
- [60] World health organization. Neonatal and perinatal mortality. *World Health Organisation*, 99:1–75, 2006.

- [61] Monica Alexander and Leontine Alkema. Global estimation of neonatal mortality using a Bayesian hierarchical splines regression model. *Demographic Research*, 38(1):335–372, 2018.
- [62] Martin W. Weber, John B. Carlin, Salvacion Gatchalian, Deborah Lehmann, Lulu Muhe, and E. Kim Mulholland. Predictors of neonatal sepsis in developing countries. *Pediatric Infectious Disease Journal*, 22(8):711–716, 2003.
- [63] A F Ouro-Bang’na Maman, K Tomta, S Ahouangbévi, and M Chobli. Deaths associated with anaesthesia in Togo, West Africa. *Tropical Doctor*, 35(4):220–222, oct 2005.
- [64] A J Heywood, I H Wilson, and J R Sinclair. Perioperative mortality in Zambia. *Annals of the Royal College of Surgeons of England*, 71:354–358, 1989.
- [65] Young-Jin Jung, Manuela Roman, Jennifer Carrasquilla, Sarah J Erickson, and Anuradha Godavarty. Portable Wide-Field Hand-Held NIR Scanner. *Proceedings of SPIE*, 8572(i):1–9, 2013.
- [66] W Karlen, G Dumont, C Petersen, J Gow, J Lim, J Sleiman, and J M Ansermino. Human-Centered Phone Oximeter Interface Design For The Operating Room: Pulse Oximeter Interfaced to a Mobile Device for Anesthesia Monitoring in the Developing World. In *Healthinf 2011: Proceedings of the International Conference on Health Informatics*, number July in 1, pages 433–438, 2011.
- [67] J. Hudson, S. M. Nguku, J. Sleiman, W. Karlen, G. A. Dumont, C. L. Petersen, C. B. Wariner, and J. M. Ansermino. Usability testing of a prototype phone Oximeter with healthcare providers in high- and low-medical resource environments. *Anaesthesia*, 67(9):957–967, 2012.
- [68] Robert A. Malkin. Barriers for medical devices for the developing world. *Expert Review of Medical Devices*, 4(6):759–763, 2007.
- [69] Jacob Poushter. Smartphone Ownership and Internet Usage Continues to Climb in Emerging Economies. *Pew Research Center*, pages 1–45, 2016.
- [70] Joseph Bailey, Michael Fecteau, and Noah L. Pendleton. Wireless Pulse Oximeter. *The Degree of Bachelor of Science*, page 80, 2008.

- [71] Elmar Laistler, Barbara Dymerska, Jürgen Sieg, Sigrun Goluch, Roberta Frass-Kriegl, Andre Kuehne, and Ewald Moser. In vivo MRI of the human finger at 7 T. *Magnetic resonance in medicine*, 79(1):588–592, jan 2018.
- [72] Q Fang and D A Boas. Monte Carlo simulation of photon migration in 3D turbid media accelerated by graphics processing units. *Opt Express*, 17(22):20178–20190, 2009.
- [73] Steven Jacques, Ting Li, and Scott Prahl. MCXYZ.c, 2013.
- [74] Sanathana Konugolu Venkata Sekar, Marco Pagliazzi, Eugènia Negredo, Fabrizio Martelli, Andrea Farina, Alberto Dalla Mora, Claus Lindner, Parisa Farzam, Núria Pérez-Álvarez, Jordi Puig, Paola Taroni, Antonio Pifferi, and Turgut Durduran. In Vivo, Non-Invasive Characterization of Human Bone by Hybrid Broadband (600-1200 nm) Diffuse Optical and Correlation Spectroscopies. *PLoS one*, 11(12):e0168426–e0168426, dec 2016.
- [75] S A Prahl. A compendium of tissue optical properties, 2012.
- [76] Steven L Jacques. Optical properties of biological tissues: a review. *Physics in Medicine and Biology*, 58(11):R37–R61, 2013.
- [77] George M Hale and Marvin R Querry. Optical Constants of Water in the 200-nm to 200- μm Wavelength Region. *Applied Optics*, 12(3):555–563, 1973.
- [78] R L P van Veen, H.J.C.M. Sterenborg, A Pifferi, A Torricelli, and R Cubeddu. Determination of VIS- NIR absorption coefficients of mammalian fat, with time- and spatially resolved diffuse reflectance and transmission spectroscopy. In *Biomedical Topical Meeting*, OSA Technical Digest, page SF4, Miami Beach, Florida, 2004. Optical Society of America.
- [79] Steven L Jacques and Daniel J McAuliffe. The Melanosome: Threshold Temperature For Explosive Vaporization and Internal Absorption Coefficient During Pulsed Laser Irradiation. *Photochemistry and Photobiology*, 53(6):769–775, jun 1991.
- [80] Alrick B Hertzman. The blood supply of various skin areas as estimated by the photoelectric plethysmograph. *American Journal of Physiology-Legacy Content*, 124(2):328–340, 1938.
- [81] Mohamed Elgendi. On the analysis of fingertip photoplethysmogram signals. *Current cardiology reviews*, 8(1):14–25, feb 2012.

- [82] Sebastian Heinzel, Florian B. Haeussinger, Tim Hahn, Ann Christine Ehlis, Michael M. Plichta, and Andreas J. Fallgatter. Variability of (functional) hemodynamics as measured with simultaneous fNIRS and fMRI during intertemporal choice. *NeuroImage*, 71:125–134, 2013.
- [83] Meryem A. Yücel, Juliette J. Selb, Theodore J. Huppert, Maria Angela Franceschini, and David A. Boas. Functional Near Infrared Spectroscopy: Enabling routine functional brain imaging. *Current Opinion in Biomedical Engineering*, 4:78–86, 2017.
- [84] Nicole M. McDonald and Katherine L. Perdue. The infant brain in the social world: Moving toward interactive social neuroscience with functional near-infrared spectroscopy. *Neuroscience and Biobehavioral Reviews*, 87(December 2017):38–49, 2018.
- [85] Richard N. Aslin, Mohinish Shukla, and Lauren L. Emberson. Hemodynamic Correlates of Cognition in Human Infants. *Annual Review of Psychology*, 66(1):349–379, 2015.
- [86] Ross E. Vanderwert and Charles A. Nelson. The use of near-infrared spectroscopy in the study of typical and atypical development. *NeuroImage*, 85:264–271, 2014.
- [87] Teresa Wilcox and Marisa Biondi. fNIRS in the developmental sciences. *Wiley Interdisciplinary Reviews: Cognitive Science*, 6(3):263–283, 2015.
- [88] Mojtaba Soltanlou, Maria A. Sitnikova, Hans Christoph Nuerk, and Thomas Dresler. Applications of functional near-infrared spectroscopy (fNIRS) in studying cognitive development: The case of mathematics and language. *Frontiers in Psychology*, 9(APR), 2018.
- [89] Valentina Quaresima, Silvia Bisconti, and Marco Ferrari. A brief review on the use of functional near-infrared spectroscopy (fNIRS) for language imaging studies in human newborns and adults. *Brain and Language*, 121(2):79–89, 2012.
- [90] Sonja Rossi, Silke Telkemeyer, Isabell Wartenburger, and Hellmuth Obrig. Shedding light on words and sentences: Near-infrared spectroscopy in language research. *Brain and Language*, 121(2):152–163, 2012.
- [91] Ann-Christine Ehlis, Sabrina Schneider, Thomas Dresler, and Andreas J Fallgatter. Application of functional near-infrared spectroscopy in psychiatry. *NeuroImage*, 85:478–88, 2014.

- [92] Vijay Kumar, Venkataram Shivakumar, Harleen Chhabra, Anushree Bose, Ganesan Venkatasubramanian, and Bangalore N. Gangadhar. Functional near infra-red spectroscopy (fNIRS) in schizophrenia: A review. *Asian Journal of Psychiatry*, 27(2017):18–31, 2017.
- [93] Muyue Yang, Zhen Yang, Tifei Yuan, Wuwei Feng, and Pu Wang. A systemic review of functional near-infrared spectroscopy for stroke: Current application and future directions. *Frontiers in Neurology*, 10(FEB):1–14, 2019.
- [94] Noman Naseer and Keum Shik Hong. fNIRS-based brain-computer interfaces: A review. *Frontiers in Human Neuroscience*, 9(JAN):1–15, 2015.
- [95] Sangtae Ahn and Sung C. Jun. Multi-modal integration of EEG-fNIRS for brain-computer interfaces – Current limitations and future directions. *Frontiers in Human Neuroscience*, 11(October):1–6, 2017.
- [96] Keum Shik Hong, M. Jawad Khan, and Melissa J. Hong. Feature Extraction and Classification Methods for Hybrid fNIRS-EEG Brain-Computer Interfaces. *Frontiers in Human Neuroscience*, 12(June):1–25, 2018.
- [97] Valentina Quaresima and Marco Ferrari. A mini-review on functional near-infrared spectroscopy (fNIRS): Where do we stand, and where should we go? *Photonics*, 6(3):87, 2019.
- [98] Adam T. Eggebrecht, Silvina L. Ferradal, Amy Robichaux-Viehoever, Mahlega S. Hassanpour, Hamid Dehghani, Abraham Z. Snyder1, Tamara Hershey, and Joseph P. Culver. Mapping distributed brain function and networks with diffuse optical tomography. *Nature Photonics*, 8(6):448–454, 2014.
- [99] Muriah D. Wheelock, Joseph P. Culver, and Adam T. Eggebrecht. High-density diffuse optical tomography for imaging human brain function. *Review of Scientific Instruments*, 90(5):1–24, 2019.
- [100] Artinis. OxyMon Cart fNIRS System, 2017.
- [101] TechEn. NIRSOptix CW6 System, 2018.
- [102] Hubin Zhao and Robert J. Cooper. Review of recent progress toward a fiberless, whole-scalp diffuse optical tomography system. *Neurophotonics*, 5(01):1, 2017.

- [103] Adrian Curtin and Hasan Ayaz. The Age of Neuroergonomics: Towards Ubiquitous and Continuous Measurement of Brain Function with fNIRS. *Japanese Psychological Research*, 60(4):374–386, 2018.
- [104] Joanne L. Park, Paul A. Dudchenko, and David I. Donaldson. Navigation in real-world environments: New opportunities afforded by advances in mobile brain imaging. *Frontiers in Human Neuroscience*, 12(September):1–12, 2018.
- [105] Nicholas M. Gregg, Brian R. White, Benjamin W. Zeff, Andrew J. Berger, and Joseph P. Culver. Brain specificity of diffuse optical imaging: improvements from superficial signal regression and tomography. *Frontiers in Neuroenergetics*, 2(July):1–8, 2010.
- [106] A Maki, Y Yamashita, Y Ito, E Watanabe, Y Mayanagi, and H Koizumi. Spatial and temporal analysis of human motor activity using noninvasive NIR topography. *Medical physics*, 22(12):1997–2005, dec 1995.
- [107] Daniel Chitnis, Robert J. Cooper, Laura Dempsey, Samuel Powerl, Simone Quaggia, David Highton, Clare Elwell, Jeremy C. Hebden, and Nicholas L. Everdell. Functional imaging of the human brain using a modular , fibre-less , high-density diffuse optical tomography system. *Biomedical optics express*, 7(10):4275–4288, 2016.
- [108] Alexander von Luhmann, Heidrun Wabnitz, Tilmann Sander, and Klaus-Robert Müller. M3BA : A Mobile , Modular , Multimodal Biosignal Acquisition Architecture for Miniaturized EEG-NIRS-Based Hybrid BCI and Monitoring. *IEEE Transactions on Biomedical Engineering*, 64(6):1199–1210, 2017.
- [109] R Zimmermann, F Braun, T Achtnich, Olivier Lambery, Roger Gassert, and M Wolf. Silicon photomultipliers for improved detection of low light levels in miniature near-infrared spectroscopy instruments. *Biomedical optics express*, 4(5):659–666, 2013.
- [110] Tsukasa Funane, Takashi Numata, Hiroki Sato, Shinsuke Hiraizumi, Yuichi Hasegawa, Hidenobu Kuwabara, Kiyoshi Hasegawa, and Masashi Kiguchi. Rearrangeable and exchangeable optical module with system-on-chip for wearable functional near-infrared spectroscopy system. *Neurophotonics*, 5(01):1, 2017.
- [111] Hubin Zhao, Sabrina Brigadoi, Reuben Hill, Greg Smith, Luke Dunne, Elisabetta Maria Frijia, Samuel Powell, Nick L. Everdell, and Robert Cooper. Advances in wearable high-density

- diffuse optical tomography: first applications of a new commercial technology and development of an infant-specific research device. In *Clinical and Preclinical Optical Diagnostics II*, page 110742. Optica Publishing Group, 2019.
- [112] Hubin Zhao, Elisabetta M Frijia, Vidal Rosas, Liam Collins-jones, Greg Smith, Reuben Nixon-hill, Samuel Powell, Nicholas L Everdell, and Robert J Cooper. Design and validation of a mechanically flexible and ultra-lightweight high-density diffuse optical tomography system for functional neuroimaging of newborns. *Neurophotonics*, 8(1):1–18, 2021.
- [113] Theodore J Huppert, Solomon G Diamond, Maria Angela Franceschini, and David A Boas. HomER: a review of time-series analysis methods for near-infrared spectroscopy of the brain. *Applied optics*, 48(10):280–298, 2009.
- [114] Hendrik Santosa, Xuetong Zhai, Frank Fishburn, and Theodore Huppert. The NIRS Brain AnalyzIR toolbox. *Algorithms*, 11(5), 2018.
- [115] Samuel Montero Hernandez and Luca Pollonini. NIRSplot: A tool for quality assessment of fNIRS scans. In *Biophotonics Congress: Biomedical Optics*, 2020.
- [116] Sabrina Brigadoi, Domenico Salvagnin, Matteo Fischetti, and Robert J. Cooper. Array Designer: automated optimized array design for functional near-infrared spectroscopy. *Neurophotonics*, 5(03):1, 2018.
- [117] A. Machado, Z. Cai, G. Pellegrino, O. Marcotte, T. Vincent, J. M. Lina, E. Kobayashi, and C. Grova. Optimal positioning of optodes on the scalp for personalized functional near-infrared spectroscopy investigations. *Journal of Neuroscience Methods*, 309(November 2017):91–108, 2018.
- [118] Guilherme Augusto Zimeo Morais, Joana Bisol Balardin, and João Ricardo Sato. FNIRS Optodes’ Location Decider (fOLD): A toolbox for probe arrangement guided by brain regions-of-interest. *Scientific Reports*, 8(1):1–11, 2018.
- [119] Morris D. Vanegas and Qianqian Fang. Modular Optode Configuration Analyzer. In <https://github.com/COTILab/MOCA>, 2020.
- [120] Dominik Wyser, Olivier Lambery, Felix Scholkmann, Martin Wolf, and Roger Gassert. Wearable and modular functional near-infrared spectroscopy instrument with multidistance measurements at four wavelengths. *Neurophotonics*, 4(4), 2017.

- [121] Thomas Muehlemann, Daniel Haensse, and Martin Wolf. Wireless miniaturized in-vivo near infrared imaging. *Optics Express*, 16(14):10323, 2008.
- [122] Bertan Hallacoglu, Jason W. Trobaugh, Kate L. Bechtel, and Chandran V. Seshagiri. Blood phantom verification of a new compact DOT system. In *Biomedical Optics Congress 2016*, 2016.
- [123] Tomoyuki Hiroyasu, Tomoya Yoshida, and Utako Yamamoto. Investigation of regions of interest (ROI) through the selection of optimized channels in fNIRS data. In *2015 IEEE Congress on Evolutionary Computation (CEC)*, pages 764–768. IEEE, 2015.
- [124] Qianqian Fang, Stefan A Carp, Juliette Selb, Greg Boverman, Quan Zhang, B Daniel, Richard H Moore, Eric L Miller, Dana H Brooks, and David A Boas. Combined Optical Imaging and Mammography of the Healthy Breast: Optical Contrast Derived From Breast Structure and Compression. *IEEE Transactions on Medical Imaging*, 28(1):30–42, 2009.
- [125] Michael Jermyn, Hamid Ghadyani, Michael A. Mastanduno, Wes Turner, Scott C. Davis, Hamid Dehghani, and Brian W. Pogue. Fast segmentation and high-quality three-dimensional volume mesh creation from medical images for diffuse optical tomography. *Journal of Biomedical Optics*, 18(8):1–11, 2013.
- [126] Qianqian Fang and David A. Boas. Tetrahedral mesh generation from volumetric binary and grayscale images. In *Proceedings - 2009 IEEE International Symposium on Biomedical Imaging: From Nano to Macro, ISBI 2009*, pages 1142–1145, 2009.
- [127] Mateo Calderon-Arnulphi, Ali Alaraj, and Konstantin V Slavin. Near infrared technology in neuroscience: past, present and future. *Neurological research*, 31(6):605–614, 2009.
- [128] Gentaro Taga, Fumitaka Homae, and Hama Watanabe. Effects of source-detector distance of near infrared spectroscopy on the measurement of the cortical hemodynamic response in infants. *Neuroimage*, 38(3):452–460, 2007.
- [129] Sarah Lloyd-Fox, Anna Blasi, and C E Elwell. Illuminating the developing brain: the past, present and future of functional near infrared spectroscopy. *Neuroscience and Biobehavioral Reviews*, 34(3):269–284, 2010.

- [130] Andrew Winslow. An Optimal Algorithm for Tiling the Plane with a Translated Polyomino. In Khaled Elbassioni and Kazuhisa Makino, editors, *Algorithms and Computation*, pages 3–13, Berlin, Heidelberg, 2015. Springer Berlin Heidelberg.
- [131] Hanan Samet. *The Design and Analysis of Spatial Data Structures*, volume 85. Addison-Wesley, Reading, MA, 1990.
- [132] Takahiko Kamae. A systematic method of finding all directed circuits and enumerating all directed paths. *IEEE Transactions on Circuit Theory*, 14(2):166–171, 1967.
- [133] Sabrina Brigadoi and Robert J. Cooper. How short is short? Optimum source–detector distance for short-separation channels in functional near-infrared spectroscopy. *Neurophotonics*, 2(2):025005, 2015.
- [134] Anh Phong Tran, Shijie Yan, and Qianqian Fang. Improving model-based functional near-infrared spectroscopy analysis using mesh-based anatomical and light-transport models. *Neurophotonics*, 7(1):1–18, 2020.
- [135] Eiji Okada and David T. Delpy. Near-infrared light propagation in an adult head model II Effect of superficial tissue thickness on the sensitivity of the near-infrared spectroscopy signal. *Applied Optics*, 42(16):2915, 2003.
- [136] Ruoyang Yao, Xavier Intes, and Qianqian Fang. Direct approach to compute Jacobians for diffuse optical tomography using perturbation Monte Carlo-based photon “replay”. *Biomedical Optics Express*, 9(10):4588, 2018.
- [137] John T. McConville, Charles E. Clauser, Thomas D. Churchill, Jaime Cuzzi, and Ints Kaleps. Aerospace Medical Report: Anthropometric Relationships of Body and Body Segment Moments of Inertia. Technical report, Johnson Space Center, 1980.
- [138] Gowerlabs. Gowerlabs, 2019.
- [139] James E. Crum. Future Applications of Real-World Neuroimaging to Clinical Psychology. *Psychological Reports*, 124(6):2403–2426, 2021.
- [140] Fabian Herold, Patrick Wiegel, Felix Scholkmann, Angelina Thiers, Dennis Hamacher, and Lutz Schega. Functional near-infrared spectroscopy in movement science: a systematic review on cortical activity in postural and walking tasks. *Neurophotonics*, 4(4):041403, 2017.

- [141] Parikshat Sirpal, Ali Kassab, Philippe Pouliot, and Dang Khoa Nguyen. fNIRS improves seizure detection in multimodal EEG-fNIRS recordings. *Journal of Biomedical Optics*, 24(05):1, 2019.
- [142] Eric S. Jackson, Sobana Wijekumar, Deryk S. Beal, Bryan Brown, Patricia Zebrowski, and John P. Spencer. A fNIRS Investigation of Speech Planning and Execution in Adults Who Stutter. *Neuroscience*, 406:73–85, 2019.
- [143] Guilherme Brockington, Joana Bisol Balardin, Guilherme Augusto Zimeo Morais, Amanda Malheiros, Roberto Lent, Luciana Monteiro Moura, and Joao R. Sato. From the laboratory to the classroom: The potential of functional near-infrared spectroscopy in educational neuroscience. *Frontiers in Psychology*, 9(OCT):1–7, 2018.
- [144] Daniel Lopez-Martinez, Ke Peng, Arielle Lee, David Borsook, and Rosalind Picard. Pain Detection with fNIRS-Measured Brain Signals: A Personalized Machine Learning Approach Using the Wavelet Transform and Bayesian Hierarchical Modeling with Dirichlet Process Priors. In *2019 8th International Conference on Affective Computing and Intelligent Interaction Workshops and Demos, ACIIW 2019*, pages 304–309, 2019.
- [145] N. L. Everdell, A. P. Gibson, I. D.C. Tullis, T. Vaithianathan, J. C. Hebden, and D. T. Delpy. A frequency multiplexed near-infrared topography system for imaging functional activation in the brain. *Review of Scientific Instruments*, 76(9):1–6, 2005.
- [146] Manob Jyoti Saikia, Walter G. Besio, and Kunal Mankodiya. WearLight: Toward a Wearable, Configurable Functional NIR Spectroscopy System for Noninvasive Neuroimaging. *IEEE Transactions on Biomedical Circuits and Systems*, 13(1):91–102, 2019.
- [147] Hubin Zhao, Sabrina Brigadoi, Danial Chitnis, Enrico De Vita, Marco Castellaro, Samuel Powell, Nicholas L. Everdell, and Robert J. Cooper. A wide field-of-view, modular, high-density diffuse optical tomography system for minimally constrained three-dimensional functional neuroimaging. *Biomedical Optics Express*, 11(8):4110, 2020.
- [148] Ernesto E. Vidal-Rosas, Hubin Zhao, Reuben Nixon-Hill, Greg Smith, Luke Dunne, Samuel Powell, Robert J. Cooper, and Nicholas L. Everdell. Evaluating a new generation of wearable high-density diffuse optical tomography (HD-DOT) technology via retinotopic mapping in the adult brain. *Optics InfoBase Conference Papers*, 8(2):1–24, 2021.

- [149] Guangda Liu, Wenjie Cui, Xinlei Hu, Ruolan Xiao, Shang Zhang, Jing Cai, Jiqing Qiu, and Yuan Qi. Development of a miniaturized and modular probe for fNIRS instrument. *Lasers in Medical Science*, 37(4):2269–2277, 2022.
- [150] Morris Vanegas, Miguel Mireles, and Qianqian Fang. MOCA: a systematic toolbox for designing and assessing modular functional near-infrared brain imaging probes. *Neurophotonics*, 9(01):1–23, 2022.
- [151] Paola Pinti, Clarisse Aichelburg, Sam Gilbert, Antonia Hamilton, Joy Hirsch, Paul Burgess, and Ilias Tachtsidis. A Review on the Use of Wearable Functional Near-Infrared Spectroscopy in Naturalistic Environments. *Japanese Psychological Research*, 60(4):347–373, 2018.
- [152] Nathan W Moon, Paul MA Baker, and Kenneth Goughnour. Designing wearable technologies for users with disabilities: Accessibility, usability, and connectivity factors. *Journal of Rehabilitation and Assistive Technologies Engineering*, 6:205566831986213, 2019.
- [153] Hasan Ayaz, Wesley B. Baker, Giles Blaney, David A. Boas, Heather Bortfeld, Kenneth Brady, Joshua Brake, Sabrina Brigadoi, Erin M. Buckley, Stefan A. Carp, Robert J. Cooper, Kyle R. Cowdrick, Joseph P. Culver, Ippeita Dan, Hamid Dehghani, Anna Devor, Turgut Durduran, Adam T. Eggebrecht, Lauren L. Emberson, Qianqian Fang, Sergio Fantini, Maria Angela Franceschini, Jonas B. Fischer, Judit Gervain, Joy Hirsch, Keum-Shik Hong, Roarke Horstmeyer, Jana M. Kainerstorfer, Tiffany S. Ko, Daniel J. Licht, Adam Liebert, Robert Luke, Jennifer M. Lynch, Jaume Mesquida, Rickson C. Mesquita, Noman Naseer, Sergio L. Novi, Felipe Orihuela-Espina, Thomas D. O’Sullivan, Darcy S. Peterka, Antonio Pifferi, Luca Pollonini, Angelo Sassaroli, João Ricardo Sato, Felix Scholkmann, Lorenzo Spinelli, Vivek J. Srinivasan, Keith St. Lawrence, Ilias Tachtsidis, Yunjie Tong, Alessandro Torricelli, Tara Urner, Heidrun Wabnitz, Martin Wolf, Ursula Wolf, Shiqi Xu, Changhuei Yang, Arjun G. Yodh, Meryem A. Yücel, and Wenjun Zhou. Optical imaging and spectroscopy for the study of the human brain: status report. *Neurophotonics*, 9(S2):1–65, 2022.
- [154] Stéphane Perrey. Possibilities for examining the neural control of gait in humans with fNIRS. *Frontiers in Physiology*, 5(May):10–13, 2014.
- [155] Christian H Bartkowski, Jessica Gemignani, Randall L Barbour, Klaus-dieter Lang, Von Krishiwołozki, René Vieroth, Christian Dils, Erik Jung, and Christoph H Schmitz. Variable

- Source Emitter Smart Textile Headgear Design for Functional Near Infrared Spectroscopy. In *IEEE Engineering in Medicine and Biology*, number July in 1, 2019.
- [156] K Alper, Yun Miao, and Valencia Koomson. Design of a miniaturized frequency domain near infrared spectroscopy instrument with validation in solid phantoms and human tissue. *Journal of Near Infrared Spectroscopy*, 0(0):1–11, 2022.
- [157] Ilaria Mazzonetto, Marco Castellaro, Robert J. Cooper, and Sabrina Brigadoi. Smartphone-based photogrammetry provides improved localization and registration of scalp-mounted neuroimaging sensors. *Scientific Reports*, 12(1):1–14, 2022.
- [158] SNIRF. Shared Near Infrared Format, 2021.
- [159] Christian Kothe. Lab Streaming Layer (LSL).
- [160] Rebecca L. Siegel, Kimberly D. Miller, Hannah E. Fuchs, and Ahmedin Jemal. Cancer statistics, 2022. *CA: A Cancer Journal for Clinicians*, 72(1):7–33, 2022.
- [161] Béatrice Lauby Secretan, D Ph, Chiara Scoccianti, D Ph, Dana Loomis, and D Ph. Breast-Cancer Screening — Viewpoint of the IARC Working Group. *New England Journal of Medicine*, 372(24):2353–2358, 2015.
- [162] Laszlo Tabar, Ming Fang Yen, Bedrich Vitak, Hsiu Hsi Tony Chen, Robert A. Smith, and Stephen W. Duffy. Mammography service screening and mortality in breast cancer patients: 20-year follow-up before and after introduction of screening. *Lancet*, 361(9367):1405–1410, 2003.
- [163] Joann G. Elmore, Mary B. Barton, Victoria M. Moceri, Sarah Polk, Philip J. Arena, and Suzanne W. Fletcher. Ten-year risk of false positive screening mammograms and clinical breast examinations. *New England Journal of Medicine*, 338(16):1089–1096, 1998.
- [164] Daniel Richard Leff, Oliver J. Warren, Louise C. Enfield, Adam Gibson, Thanos Athanasiou, Darren K. Patten, Jem Hebden, Guang Zhong Yang, and Ara Darzi. Diffuse optical imaging of the healthy and diseased breast: A systematic review. *Breast Cancer Research and Treatment*, 108(1):9–22, 2008.
- [165] Hamid Dehghani, Subhadra Sri Nivasan, Brian W. Pogue, and Adam Gibson. Numerical modelling and image reconstruction in diffuse optical tomography. *Philosophical*

- Transactions of the Royal Society A: Mathematical, Physical and Engineering Sciences*, 367(1900):3073–3093, 2009.
- [166] Yukio Yamada and Shinpei Okawa. Diffuse optical tomography: Present status and its future. *Optical Review*, 21(3):185–205, 2014.
- [167] Yoko Hoshi and Yukio Yamada. Overview of diffuse optical tomography and its clinical applications. *Journal of Biomedical Optics*, 21(9):091312, 2016.
- [168] A P Gibson, J C Hebden, and S R Arridge. Recent advances in diffuse optical imaging. *Physics in Medicine and Biology*, 50(4):R1–R43, 2005.
- [169] Yihan Wang, Songpeng Li, Yirong Wang, Qiang Yan, Xin Wang, Yudong Shen, Zhiqiang Li, Fei Kang, Xu Cao, and Shouping Zhu. Compact fiber-free parallel-plane multi-wavelength diffuse optical tomography system for breast imaging. *Optics Express*, 30(5):6469, 2022.
- [170] Hamed Vavadi, Chen Xu, Atahar Mostafa, and Quing Zhu. Automated data selection method for diffuse optical tomography to improve the robustness of breast cancer detection. *Optics InfoBase Conference Papers*, 7(10):387–397, 2014.
- [171] Molly L. Flexman, Hyun K. Kim, Jacqueline E. Gunther, Emerson A. Lim, Maria C. Alvarez, Elise Desperito, Kevin Kalinsky, Dawn L. Hershman, and Andreas H. Hielscher. Optical biomarkers for breast cancer derived from dynamic diffuse optical tomography. *Journal of Biomedical Optics*, 18(9):096012, 2013.
- [172] Regine Choe, Soren D Konecky, Alper Corlu, Kijoon Lee, Turgut Durduran, David R Busch, Saurav Pathak, Brian J Czerniecki, Julia Tchou, Douglas L Fraker, Angela Demichele, Britton Chance, Simon R Arridge, Martin Schweiger, Joseph P Culver, Mitchell D Schnall, Mary E Putt, Mark A Rosen, and Arjun G Yodh. Differentiation of benign and malignant breast tumors by in-vivo three-dimensional parallel-plate diffuse optical tomography. *Journal of biomedical optics*, 14(2):24020, 2009.
- [173] Paola Taroni, Alessandro Torricelli, Lorenzo Spinelli, Antonio Pifferi, Francesco Arpaia, Gianmaria Danesini, and Rinaldo Cubeddu. Time-resolved optical mammography between 637 and 985 nm: Clinical study on the detection and identification of breast lesions. *Physics in Medicine and Biology*, 50(11):2469–2488, 2005.

- [174] Ang Li, Jing Liu, Wendy Tanamai, Richard Kwong, Albert E Cerussi, and J Bruce. Assessing the spatial extent of breast tumor intrinsic optical contrast using ultrasound and diffuse optical spectroscopy. *Journal of Biomedical Optics*, 13(3):1–8, 2010.
- [175] Bernhard B. Zimmermann, Bin Deng, Bhawana Singh, Mark Martino, Juliette Selb, Qianqian Fang, Amir Y. Sajjadi, Jayne Cormier, Richard H. Moore, Daniel B. Kopans, David A. Boas, Mansi A. Saksena, and Stefan A. Carp. Multimodal breast cancer imaging using coregistered dynamic diffuse optical tomography and digital breast tomosynthesis. *Journal of Biomedical Optics*, 22(4):046008, 2017.
- [176] Bin Deng, Dana H. Brooks, David A. Boas, Mats Lundqvist, and Qianqian Fang. Characterization of structural-prior guided optical tomography using realistic breast models derived from dual-energy x-ray mammography. *Biomedical Optics Express*, 6(7):2366–2379, 2015.
- [177] J. P. Culver, R. Choe, M. J. Holboke, L. Zubkov, T. Durduran, A. Slemp, V. Ntziachristos, B. Chance, and A. G. Yodh. Three-dimensional diffuse optical tomography in the parallel plane transmission geometry: Evaluation of a hybrid frequency domain/continuous wave clinical system for breast imaging. *Medical Physics*, 30(2):235–247, 2003.
- [178] Quing Zhu and Steven Poplack. A review of optical breast imaging: Multi-modality systems for breast cancer diagnosis. *European Journal of Radiology*, 129:109067, 2020.
- [179] Venkataraman Krishnaswamy, Kelly E. Michaelsen, Brian W. Pogue, Steven P. Poplack, Ian Shaw, Ken Defrietas, Ken Brooks, and Keith D. Paulsen. A digital x-ray tomosynthesis coupled near infrared spectral tomography system for dual-modality breast imaging. *Optics Express*, 20(17):19125, 2012.
- [180] Fadi El-Ghussein, Michael A Mastanduno, Shudong Jiang, Brian W Pogue, and Keith D Paulsen. Hybrid photomultiplier tube and photodiode parallel detection array for wideband optical spectroscopy of the breast guided by magnetic resonance imaging. *Journal of Biomedical Optics*, 19(1):11010, aug 2013.
- [181] Vasilis Ntziachristos, A G Yodh, Mitchell D Schnall, and Britton Chance. MRI-Guided Diffuse Optical Spectroscopy of Malignant and Benign Breast Lesions. *Neoplasia*, 4(4):347–354, 2002.

- [182] Alejandro Rodríguez-Ruiz, Greeshma A. Agasthya, and Ioannis Sechopoulos. The compressed breast during mammography and breast tomosynthesis: In vivo shape characterization and modeling. *Physics in Medicine and Biology*, 62(17):6920–6937, 2017.
- [183] Matthew J. Pallone, Steven P. Poplack, Hima Bindu R. Avutu, Keith D. Paulsen, and Richard J. Barth. Supine breast MRI and 3D optical scanning: A novel approach to improve tumor localization for breast conserving surgery. *Annals of Surgical Oncology*, 21(7):2203–2208, 2014.
- [184] C. Gallego Ortiz and A. L. Martel. Automatic atlas-based segmentation of the breast in MRI for 3D breast volume computation. *Medical Physics*, 39(10):5835–5848, 2012.
- [185] Ben Brooksby, Brian W. Pogue, Shudong Jiang, Hamid Dehghani, Subhadra Srinivasan, Christine Kogel, Tor D. Tosteson, John Weaver, Steven P. Poplack, and Keith D. Paulsen. Imaging breast adipose and fibroglandular tissue molecular signatures by using hybrid MRI-guided near-infrared spectral tomography. *Proceedings of the National Academy of Sciences of the United States of America*, 103(23):8828–8833, 2006.
- [186] Julia Krüger, Jan Ehrhardt, Arpad Bischof, and Heinz Handels. Breast compression simulation using ICP-based B-spline deformation for correspondence analysis in mammography and MRI datasets. *Medical Imaging 2013: Image Processing*, 8669(March 2013):86691D, 2013.
- [187] Carl L Kalbhen, John J McGill, Paul M Fendley, Kevin W Corrigan, and Juan Angelats. Mammographic Determination of Breast Volume: Comparing Different Methods. *American Journal of Roentgenology*, 173(6):1643–1649, 1999.
- [188] Yasuyo Kita, Ralph Highnam, and Michael Brady. Correspondence between different view breast x-rays using a simulation of breast deformation. *Proceedings of the IEEE Computer Society Conference on Computer Vision and Pattern Recognition*, pages 700–707, 1998.
- [189] Jessica B. Chang, Kevin H. Small, Mihye Choi, and Nolan S. Karp. Three-Dimensional Surface Imaging in Plastic Surgery: Foundation, Practical Applications, and beyond. *Plastic and Reconstructive Surgery*, 135(5):1295–1304, 2015.

- [190] Albert Losken, Hisham Seify, Donald D. Denson, Alfredo A. Jr Paredes, and Grant W. Carlson. Validating Three-Dimensional Imaging of the Breast. *Annals of Plastic Surg*, 54(5):471–476, 2005.
- [191] Xiangyang Ju, Helga Henseler, Matthew Jian qiao Peng, Balvinder S. Khambay, Arup K. Ray, and Ashraf F. Ayoub. Multi-view stereophotogrammetry for post-mastectomy breast reconstruction. *Medical and Biological Engineering and Computing*, 54(2-3):475–484, 2016.
- [192] Greg M. Galdino, Maurice Nahabedian, Michael Chiaramonte, Jason Z. Geng, Stanley Klatsky, and Paul Manson. Clinical applications of three-dimensional photography in breast surgery. *Plastic and Reconstructive Surgery*, 110(1):58–70, 2002.
- [193] Qianqian Fang. Quantitative diffuse optical tomography using a mobile phone camera and automatic 3D photo stitching. In *Biomedical Optics and 3-D Imaging*, page BSu3A.96. Optica Publishing Group, 2012.
- [194] Helga Henseler, J Smith, A Bowman, BS Khambay, Xiangyang Ju, Ashraf F. Ayoub, and Arup K. Ray. Investigation into variation and errors of a three-dimensional breast imaging system using multiple stereo cameras. *Journal of Plastic, Reconstructive and Aesthetic Surgery*, 65(12), 2012.
- [195] Helga Henseler, BS Khambay, A Bowman, J Smith, J Paul Siebert, S Oehler, X Ju, A Ayoub, and AK Ray. Investigation into accuracy and reproducibility of a 3D breast imaging system using multiple stereo cameras. *Journal of Plastic, Reconstructive and Aesthetic Surgery*, 64(5), 2011.
- [196] Maurice Y. Nahabedian and Gregory Galdino. Symmetrical breast reconstruction: Is there a role for three-dimensional digital photography? *Plastic and Reconstructive Surgery*, 112(6):1582–1590, 2003.
- [197] Laszlo Kovacs, Alexander Yassouridis, Alexander Zimmermann, Gernot Brockmann, Antonia Wöhnl, Matthias Blaschke, Maximilian Eder, Katja Schwenzer-Zimmerer, Robert Rosenberg, Nikolaos A. Papadopoulos, and Edgar Biemer. Optimization of 3-Dimensional Imaging of the Breast Region With 3-Dimensional Laser Scanners. *Annals of Plastic Surgery*, 56(3):229–236, 2006.

- [198] Laszlo Kovacs, Maximilian Eder, Regina Hollweck, Alexander Zimmermann, Markus Settles, Armin Schneider, Kristian Udovic, Katja Schwenzer-Zimmerer, Nikolaos A Papadopoulos, and Edgar Biemer. New Aspects of Breast Volume Measurement Using 3-Dimensional Surface Imaging. *Annals of Plastic Surgery*, 57(6):602–610, 2006.
- [199] Laszlo Kovacs, Maximilian Eder, Regina Hollweck, Alexander Zimmermann, Markus Settles, Armin Schneider, Matthias Endlich, Andreas Mueller, Katja Schwenzer-Zimmerer, Nikolaos A. Papadopoulos, and Edgar Biemer. Comparison between breast volume measurement using 3D surface imaging and classical techniques. *Breast*, 16(2):137–145, 2007.
- [200] Martin C. Koch, Boris Adamietz, Sebastian M. Jud, Peter A. Fasching, Lothar Haeberle, Stefan Karbacher, Klaus Veit, Ruediger Schulz-Wendtland, Michael Uder, Matthias W. Beckmann, Mayada R. Bani, Katharina Heusinger, Christian R. Loehberg, and Alexander Cavaliero. Breast volumetry using a three-dimensional surface assessment technique. *Aesthetic Plastic Surgery*, 35(5):847–855, 2011.
- [201] J. Grant Thomson, Yuen Jong Liu, Richard J. Restifo, Brian D. Rinker, and Andrew Reis. Surface area measurement of the female breast: Phase I. validation of a novel optical technique. *Plastic and Reconstructive Surgery*, 123(5):1588–1596, 2009.
- [202] Susan C Kuzminsky and Megan S Gardiner. Three-dimensional laser scanning: potential uses for museum conservation and scientific research. *Journal of Archaeological Science*, 39(8):2744–2751, 2012.
- [203] Ametek. HandySCAN 3D Technical Specifications, 2002.
- [204] Artec3D. Artec Leo Technical Specifications, 2022.
- [205] Di Yang, Dayong Qiao, and Changfeng Xia. Curved light surface model for calibration of a structured light 3D modeling system based on striped patterns. *Optics Express*, 28(22):33240, 2020.
- [206] Song Zhang. High-speed 3D shape measurement with structured light methods: A review. *Optics and Lasers in Engineering*, 106:119–131, 2018.
- [207] Stefan A Carp, Tina Kauffman, Qianqian Fang, Elizabeth Rafferty, Richard Moore, Daniel Kopans, and David Boas. Compression-induced changes in the physiological state of the

- breast as observed through frequency domain photon migration measurements. *Journal of Biomedical Optics*, 11(6):64016, 2006.
- [208] S A Carp, J Selb, Q Fang, R Moore, D B Kopans, E Rafferty, and D A Boas. Dynamic functional and mechanical response of breast tissue to compression. *Optics Express*, 16(20):16064, sep 2008.
- [209] Stefan A Carp, Amir Y Sajjadi, Christy M Wanyo, Qianqian Fang, Michelle C Specht, Lidia Schapira, Beverly Moy, Aditya Bardia, David A Boas, and Steven J Isakoff. Hemodynamic signature of breast cancer under fractional mammographic compression using a dynamic diffuse optical tomography system. *Biomedical Optics Express*, 4(12):2911, dec 2013.
- [210] Bernhard B Zimmermann, Qianqian Fang, David A Boas, and Stefan A Carp. Frequency domain near-infrared multiwavelength imager design using high-speed, direct analog-to-digital conversion. *Journal of Biomedical Optics*, 21(1):1–8, 2016.
- [211] Seiji Inokuchi, K Sato, and F Matsuda. Range-imaging system for 3-D object recognition. In *Proceedings of the International Conference on Pattern Recognition*, pages 806–808, 1984.
- [212] Seppe Sels, Bart Ribbens, Steve Vanlanduit, and Rudi Penne. Camera Calibration Using Gray Code. *Sensors*, 19(2), 2019.
- [213] Daniel Moreno and Gabriel Taubin. Scan3d-Capture, 2012.
- [214] Yi Xu and Daniel G. Aliaga. Robust pixel classification for 3D modeling with structured light. *Proceedings - Graphics Interface*, pages 233–240, 2007.
- [215] Z Zhang. A flexible new technique for camera calibration. *IEEE Transactions on Pattern Analysis and Machine Intelligence*, 22(11):1330–1334, nov 2000.
- [216] Jean-Yves Bouguet. *Camera calibration tool box for matlab*. Natick, Massachusetts, United State, 2004.
- [217] W. Lingle, B. J. Erickson, M. L. Zuley, R. Jarosz, E. Bonaccio, J. Filippini, and N. Gruszauskas. Radiology Data from The Cancer Genome Atlas Breast Invasive Carcinoma [TCGA-BRCA] collection., 2016.
- [218] Paul A. Yushkevich, Joseph Piven, Heather Cody Hazlett, Rachel Gimpel Smith, Sean Ho, James C. Gee, and Guido Gerig. User-guided 3D active contour segmentation of anatomical

- structures: Significantly improved efficiency and reliability. *NeuroImage*, 31(3):1116–1128, 2006.
- [219] François Pomerleau, Francis Colas, Roland Siegwart, Stéphane Magnenat, François Pomerleau, Francis Colas, Roland Siegwart, Stéphane Magnenat, Comparing Icp, and Francis Colas Roland. Comparing ICP variants on real-world data sets Open-source library and experimental protocol To cite this version : HAL Id : hal-01143458 Comparing ICP Variants on Real-World Data Sets. *Autonomous Robots*, 34(3):133–148, 2013.
- [220] Radu Bogdan Rusu, Zoltan Csaba Marton, Nico Blodow, Mihai Dolha, and Michael Beetz. Towards 3D Point cloud based object maps for household environments. *Robotics and Autonomous Systems*, 56(11):927–941, 2008.
- [221] Nina Amenta, Marshall Bern, and Manolis Kamvysselis. A New Voronoi-Based Surface Reconstruction Algorithm. In *Proceedings of the 25th Annual Conference on Computer Graphics and Interactive Techniques*, SIGGRAPH ’98, pages 415–421, New York, NY, USA, 1998. Association for Computing Machinery.
- [222] Qianqian Fang, Stefan A Carp, Juliette J. Selb, Richard H. Moore, Daniel B. Kopans, Eric L. Miller, Dana H. Brooks, and David A. Boas. A multi- modality image reconstruction platform for diffuse optical tomography. In *OSA Biomedical Optics (BIOMED)*, 2008.
- [223] Ruoyang Yao, Qi Pian, and Xavier Intes. Wide-field fluorescence molecular tomography with compressive sensing based preconditioning. *Biomed. Opt. Express*, 6(12):4887–4898, dec 2015.
- [224] Marta Pinto, Ruby Egging, Alejandro Rodríguez-Ruiz, Koen Michielsen, and Ioannis Sechopoulos. Compressed breast shape characterization and modelling during digital breast tomosynthesis using 3D stereoscopic surface cameras. In *15th International Workshop on Breast Imaging*, page 38, 2020.
- [225] Alice Chong, Susan P Weinstein, Elizabeth S McDonald, and Emily F Conant. Digital Breast Tomosynthesis: Concepts and Clinical Practice. *Radiology*, 292(1):1–14, 2019.